

**BRNO UNIVERSITY OF TECHNOLOGY**  
VYSOKÉ UČENÍ TECHNICKÉ V BRNĚ

**FACULTY OF INFORMATION TECHNOLOGY**  
**DEPARTMENT OF INTELLIGENT SYSTEMS**  
FAKULTA INFORMAČNÍCH TECHNOLOGIÍ  
ÚSTAV INTELIGENTNÍCH SYSTÉMŮ

**THEORETICAL AND EXPERIMENTAL  
DETERMINATION OF THE AMOUNT OF INFORMATION  
IN HUMAN OCULAR BIOMETRIC CHARACTERISTICS**  
TEORETICKÉ A EXPERIMENTÁLNÍ STANOVENÍ MNOŽSTVÍ INFORMACÍ V BIOMETRICKÝCH  
VLASTNOSTECH LIDSKÉHO OKA

**DOCTORAL THESIS**  
DISERTAČNÍ PRÁCE

**AUTHOR**  
AUTOR PRÁCE

Ing. LUKÁŠ SEMERÁD

**SUPERVISOR**  
ŠKOLITEL

Prof. Ing., Dipl.-Ing., MARTIN  
DRAHANSKÝ, Ph.D.

BRNO 2022



## Abstract

The aim of this work is to design method and quantify amount of biometric entropy in the human retina. In other words, this work seeks to determine how unique this biometric feature is, and whether universality is ensured in the human population. The first part shows how the human eye works, especially with regard to the retina. It also mentions the physiological basis of angiogenesis in the retina, on which biometric recognition is based in the work's next part. Further are noted ophthalmological devices designed by the STRaDe research group, which are equipped algorithms for detection of the most common diseases in the retina, which are manifested by a visual change. The fourth part presents a tool for generating synthetic retinas, which can be used to create databases for testing other algorithms. Further part deals with the statistical evaluation of the points and properties of the retina, from which it's based the theoretical formula for the calculation retina biometric entropy. In the final chapter are outlined several principles for quantify the mentioned theoretical formula. The work could serve to prove the uniqueness of biometric devices based on retinal scanning, which are currently not very widespread.

## Abstrakt

Cílem této práce je navrhnout způsob a vyčíslit množství biometrické entropie v sítnici lidského oka. Jinými slovy se tato práce snaží určit, jak moc unikátní tento biometrický rys je a zda je zajištěna univerzálnost v lidské populaci. V první části je uvedeno, jak oko funguje s přihlédnutím zejména k sítnici. Jsou zde také zmíněny fyziologické základy tvorby cév v sítnici, na kterých je pak biometrické rozpoznávání v další části práce založeno. Představeny jsou také oftalmologické přístroje, navržené výzkumnou skupinou STRaDe. V další části je čtenář seznámen s nejběžnějšími onemocněními sítnice, které se projevují vizuální změnou této části těla, a tudíž i ovlivňují možnosti správného rozpoznávání. Jsou také uvedeny algoritmy, kterými lze zmíněná onemocnění detekovat. Ve čtvrté části je představen nástroj pro generování syntetických sítnic, který lze využít například pro tvorbu databází pro testování dalších algoritmů. Následující část pojednává o statistickém vyhodnocení bodů a vlastností sítnice, ze kterých posléze vychází teoretický vzorec pro výpočet na začátku zmíněné biometrické entropie sítnice. V závěrečné fázi je nastíněno několik principů, kterými je možné zmíněný teoretický vzorec vyčíslit, aby se dalo stanovit, jak unikátní zmíněný biometrický rys je. Práce by díky zjištěním mohla sloužit pro důkaz unikátnosti biometrických zařízení, založených na snímání sítnice, které v současné době nejsou zatím příliš rozšířeny.

## **Keywords**

Human eye, retina, biometrics, biometric entropy, biometric system, vessel bifurcation, vessel crossing, retina diseases, synthetic retina images, retina statistical properties.

## **Klíčová slova**

Lidské oko, sítnice, biometrie, biometrická entropie, biometrický systém, rozdvojení cév, křížení cév, onemocnění sítnice, syntetické snímky sítnice, statistické vlastnosti sítnice.

## **Citation**

Lukáš Semerád: Theoretical and Experimental Determination of the Amount of Information in Human Ocular Biometric Characteristics, doctoral thesis, Brno, FIT BUT, Czech Republic, 2022.

## Declaration

I hereby declare that this thesis is my original work and has been created under the supervision of Prof. Ing., Dipl.-Ing. Martin Drahanský, Ph.D. Some results were achieved in cooperation with bachelor's or master's degree students led by my supervisor or myself. Where other sources of information have been used, they have been duly acknowledged.

.....

Lukáš Semerád

May 31, 2022

## Acknowledgements

I would like to send my biggest thanks to my supervisor Martin Drahanský for his always-helpful approach, precisely targeted advice and huge help throughout my studies. I would also like to thank Ivana Petříková for her help in correcting mathematical formulas and Tomáš Mňuk and Karolína Skorkovská for their medical advice and lessons. I also thank to Luděk Smolik for the thought control of the idea. I would also like to thank Radim Kolář, Dušan Kolář, Petr Malaník and Milan Češka jr. Last but not least, my thanks go to my loved ones and members of the STRaDe research group.

This thesis was supported by projects Reliability and Security in IT (FIT-S-14-2486), Secure and Reliable Computer Systems (FIT-S-17-4014) and Reliable, Secure and Effective Computer Systems (FIT-S-20-6427).

# Contents

<b>1</b>	<b>Introduction.....</b>	<b>9</b>
<b>2</b>	<b>Retina recognition technology .....</b>	<b>13</b>
2.1	Human eye.....	13
2.1.1	Iris.....	15
2.1.2	Medical use.....	15
2.1.3	Biometric use.....	15
2.2	Retina.....	15
2.2.1	Medical basis of vein structure.....	17
2.3	Biometric recognition .....	18
2.3.1	Retinal image.....	20
2.4	History of retinal recognition .....	21
2.5	Medical and biometric examination and acquisition tools.....	22
2.5.1	Medical devices .....	22
2.5.2	Device EYRINA.....	24
2.6	Recognition schemes .....	33
2.6.1	Biometric entropy.....	34
2.7	Limitations.....	36
<b>3</b>	<b>Retinal diseases and their effects .....</b>	<b>37</b>
3.1	Retinal diseases.....	37
3.1.1	Diabetes mellitus .....	37
3.1.2	Diabetic retinopathy .....	38
3.1.3	Age-related macular degeneration.....	40
3.1.4	Retinal detachment .....	43
3.1.5	Cracked retina.....	44
3.1.6	Retinal inflammation .....	44
3.1.7	Retinal swelling.....	44
3.1.8	Circulatory disorders of the retina.....	45
3.2	Automatic retina processing .....	45
3.2.1	Pre-processing .....	46
3.2.2	Obtaining a background mask .....	47
3.2.3	Obtaining properties of the retina.....	47
3.2.4	Optical disc detection .....	48
3.2.5	Fovea detection.....	49

3.2.6	Blood stream detection .....	50
3.3	Automatic disease detection .....	52
3.3.1	Detection of druses and exudates .....	53
3.3.2	Microaneurysm and hemorrhage .....	58
3.4	Testing .....	64
3.4.1	Hard and soft exudates detection.....	64
3.4.2	Microaneurysm and hemorrhage detection .....	65
3.4.3	Additional test algorithms .....	66
<b>4</b>	<b>Synthetic retinas.....</b>	<b>69</b>
4.1	Synthetic retinal images generator .....	69
4.1.1	Vascular bed layer .....	70
4.1.2	Layers .....	72
4.1.3	Background layers .....	74
4.1.4	Generating a vascular bed .....	75
4.1.5	Image result .....	77
4.2	Algorithm improvements.....	78
4.2.1	Retinal vessel shapes identification in macular and nasal bloodstream .....	78
4.2.2	Identification of vessel shapes and branches.....	84
4.2.3	Summary of achieved results.....	90
4.3	Synthetic images generated via neural network .....	90
<b>5</b>	<b>Statistical evaluation.....</b>	<b>93</b>
5.1	Coordinate system .....	94
5.2	Recognition scheme.....	95
5.3	Used databases.....	96
5.4	Developed applications.....	97
5.4.1	Manual marking program.....	97
5.4.2	Automatic marking application .....	97
5.4.3	Application for comparison.....	97
5.4.4	Visualization application .....	99
5.4.5	Recognition application.....	100
5.5	Basic field resolution .....	101
5.6	Number of bifurcations in one image .....	102
5.7	Cropping of edges.....	103
5.7.1	Rectangular cropping of edges .....	104
5.7.2	Circular cropping of edges .....	105

5.8	Results from synthetic retinas.....	106
5.8.1	Testing.....	106
5.8.2	Statistical treatment.....	107
<b>6</b>	<b>Theoretical enumeration of biometric entropy in retina.....</b>	<b>109</b>
6.1	General principle of theoretical quantification.....	109
6.1.1	Experimental calculation of the formula.....	110
6.1.2	Automatic finding.....	111
6.2	Theoretical formula.....	112
<b>7</b>	<b>Practical enumeration of the formula.....</b>	<b>117</b>
7.1	Computing algorithms.....	117
7.1.1	Program in Matlab.....	117
7.1.2	Program in C language.....	117
7.2	Simplification of the calculation.....	119
7.2.1	Field raster reduction.....	119
7.2.2	Retinal symmetry.....	119
7.2.3	Division into regular clusters.....	119
7.2.4	Division into clusters according to probability.....	120
7.2.5	Division into discontinuous areas with the same overall probability.....	121
7.3	Random choose.....	122
<b>8</b>	<b>Conclusion.....</b>	<b>125</b>
<b>9</b>	<b>References.....</b>	<b>127</b>

# 1 Introduction

Human recognition based on its *biometric features* is an increasingly important role for nowadays. In addition, this is mainly for security reasons - whether unlocking a mobile phone, secure access to rooms or investigating criminal offenses. In all these sectors, the question always arises as to whether and how secure the access system is. Whether from the point of view of breaking the system by an unauthorized person or the impossibility of a given biometric feature to recognize a larger number of people. Moreover, it is the second mentioned circumstances that this work deals with. It tries to determine how unique the biometric feature of the *retina* is, i.e. the image of the ocular background. In summary, this degree of diversity can be described as *biometric entropy*.

The oldest mentions of human recognition are preserved from China in the 14<sup>th</sup> century, but for example, various shapes on the fingertip have attracted our ancestors much earlier, because paintings in caves are also preserved. Greater efforts to identify people among themselves began in the second half of the 19<sup>th</sup> century. Area of research of human characteristics was named as *biometrics*. This word was created by combining the Latin words *bios* (life) and *metron* (scale) - that is, the measurement of a living person. Probably the greatest pioneers of biometrics were Francois Galton and William James Herschel. The first one dealt with anthropometry, the second one with fingerprints. In the historical context, the topic of biometrics is probably most relevant to criminology, as it was necessary to identify the perpetrators of crimes. In biometrics, *identification* is a term for determining the identity of a particular individual from records stored in a database. Another approach is *verification*, where we try to prove based on the stored data about the individual that it is really the mentioned individual. *Identity* is the identification of an existing individual. The first method for identify people for forensic reasons was the so-called *anthropometry*. This system measured specific human body lengths, such as body height, head width, or left middle finger length. The total of these measures was 11. After several years, Alphonse Bertillon took over the method of identification and enforced it into the already mentioned criminology. Therefore, the method began to be called *bertillonation*. It has been used for more than 20 years. Then were discovered the patterns of papillary lines on the hands. This biometric feature is called *dactyloscopy* and used for more than 100 years, which is the time during which most of the physiological laws have been discovered.

In recent decades, other methods have come up, but they serve to simplify life at the beginning, rather than criminology. With advances in the field of computer speed, iris biometrics, recognition based on the visible part of the human eye, has developed greatly. Several thousand people can also be identified based on the shape of the hand, which is a method based on anthropometry, as it measures the individual lengths and widths of the fingers and palms. Recently, computationally high-performance facial recognition is gaining more and more prominence. In addition, despite several different biometric features, it can be recognized on the basis of images taken by a thermal cameras. It is, for example, the

previously mentioned face or hand. We must not forget to mention one very strong biometric feature, DNA (deoxyribonucleic acid). It can be used to identify individuals very reliably; an insurmountable disadvantage for biometric access systems, for example, but it is a very long time of sequencing, i.e. "reading" genetic information.

Another larger category of biometric features are the *behavioral features*, which, in contrast to the mentioned physiological features, can be slightly influenced with greater effort. However, recognition should focus on those elements of biometric features that the user cannot falsify. Behavioral features include, for example, the dynamics of a signature, which, in contrast to a static signature on paper, also focuses on the characteristics of the signature operation itself, such as the tilt of the pen, its pressure on the pad or speed. Another behavioral feature is walking, according to which it is possible to distinguish, for example, masked people in the video or characters at a great distance. For all these biometric features, it is useful to know the already mentioned value of biometric entropy, so that we know how many people can be distinguished by our system and how reliable the system will be. In the case of fingerprints in particular, this value has been calculated for a long time; the aim of this work is to calculate this value on the basis of another method, which has probably not been used anywhere yet – by monitoring the bifurcation and crossing of the vascular bed in retinal images. This is perhaps the second extreme of possible observation of these images. Some works focused only on the area of the optical disk, this work tries to use the area of the whole image, which, however, can change significantly when the surrounding shooting conditions change. Therefore, we try to homogenize the images as much as possible.

Retinal entropy is greatly affected by possible diseases. Some of them may cover a large part of the retina. There is no crossing in this part and the images are very different from the standard ones. If the disease progresses, the individual may not be identified. Therefore, the most common diseases that have their shows on the retina are mentioned in the work. For example, widespread diabetic retinopathy may not affect the recognition results at all, but vessel bleeding may cause completely unusable results. Because the study of the course and development of diseases is very complicated, only healthy images were taken to calculate the biometric entropy. In this case, the algorithms by which we are able to detect retinal disease and determine whether this image can be considered fully informative also play an important role. These detection algorithms can also be very helpful in medicine. A lot of eye problems are revealed very late. If even some biometric access systems could recommend a doctor's visit to the user, the consequences of the disease could be lower than now. Even from this motivation, our research group cooperates with leading ophthalmologists on the development of similar devices.

Another large chapter is a description of algorithms for generating random retinal images, which are based on plausible branching of the vascular bed. Scanning the retina of the human eye correctly is complicated and time-consuming, so there are currently only a small number of public image databases. A large amount of data is necessary for the proper functioning and testing of the generated algorithms. We have therefore developed this generator, which we can use to create a large number of images, both healthy and sick. By accidentally entering the symptoms of the disease, we certainly know in which

images and in which places the detectors should detect the finding. Finding the disease in healthy pictures is much more complicated, we need a lot of time experienced ophthalmologists who correctly mark the symptoms of the disease.

Probably the biggest contribution of this work is given in the last chapters. First of them, it is a statistical analysis of vascular branching on retinal images. Both the directions of branching and the individual points at which this occurs, or where the vessels visually intersect, are detected. At these points, we then find out whether crosses and bifurcations occur more often in some parts of the back of the eye than in others. For remind, these points is on which we base our recognition biometric method. From the given areas and frequencies of occurrences points, we then create a probabilistic model in which we process values from several hundred real retinas. On this basis, we then create a set of formulas, which we use to determine the variability of their individual parameters. In the final chapter, we then try to quantify the developed formulas specifically. We try in several ways to calculate the biometric entropy as accurately as possible on the model we specify.

The ambition of this work is to prove the great diversity of the vascular bed in the retina of the human eye, so that it is clear how safe we can then call it safe.



## 2 Retina recognition technology

First chapter describes general information, which is important to understand the context the rest of the work. It describes basic concepts of human eye anatomy and biometrics. The main goal of this thesis is closely related to the retina recognition technology used in biometrics, thus the basic knowledge of biometrics with an emphasis on retina and methods to acquiring them is covered. An integral part is also the way the recognition of retinas works, i.e. the processes that are necessary to acquire a retina. All terms related to biometrics are consulted with [45].

### 2.1 Human eye

The *human eye* is the most complicated and one of the most important sense organs at all. As shown in Figure 2.2, a human eye consists of many working parts such as sclera, cornea, pupil, lens, iris, ciliary body, retina, optic nerve, choroid, etc. *Sclera*, the white colored outer layer of the eye, works as a protector of the eye.

The eye reacts to light entering inside (photoreceptor) and ensures sense of sight. From the physical point of view, it is a transparent biconvex optical system, which focuses the light rays onto the surface of the retina by help of cornea and eye lens. *Cornea* is a front elastic part of the eye. It's transparent, without vessels and with the fixed optical power of more than 43 diopters represents approximately two-thirds of the eye's total power. The human eye can distinguish about 10 million colors [111].

Another optic element of the eye is a *lens* with ability to change its shape and thus optical power and focal length. It allows focusing on object in different distances from observer (accommodation). The minimal and maximal distance, which the eye can focus on, is given by two points [108]:

- *Near point* – a shortest distance between object and observer, which gives still sharp image on the retina. In this case, the optical system of the eye has the largest optical power of more than 60 diopters. A healthy eye can focus on the object at distance of 25 cm without any exertion.
- *Far point* – the longest distance between object and observer, which gives still sharp picture on the retina. The eye lens has the lowest optical power. By a healthy individual is this distance in infinity.

The light entering eye is controlled by *iris*. The iris surface has a shape of annulus with a central hole – *pupil*. Iris controls the diameter of the pupil and thus the amount of light falling on the retina. It has a similar function as aperture of camera lens.

Figure 2.1 shows the projection into the eye. The resulting image of the outside world is in the eye inverted (upside down), mirrored and reduced. On the retina, there are two significant objects – optic disc and macula [107]. *Optic disc* is an area where optic nerve and main blood vessels come into the eye. Thus, there are no *photoreceptors*. The *macular area* has the highest density of cones allowing a high sensitivity under photonics conditions. The captured image is subsequently transformed to electric

signals, which are directed to the brain via optic nerve. In the brain, the image is processed there, i.e. it is flipped upside down and mirrored according to the reality.

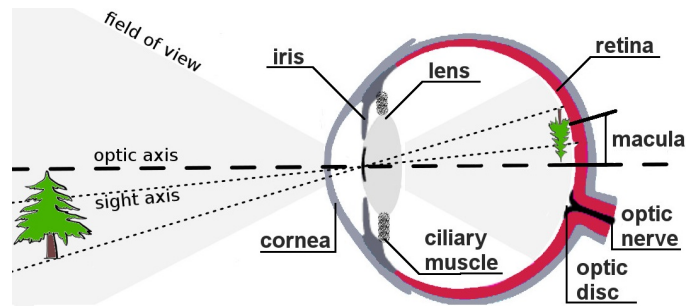


Figure 2.1: Image projection into the eye [30].

A thorough understanding of eye anatomy is closely related to a proposal of optical system for acquirement of digital copy of the eye. That can be used for medical as well as for biometric purposes. The eye is not shaped like a perfect sphere, rather it is a fused two-piece unit. The smaller frontal unit, transparent and more curved, called the cornea is linked to the larger white unit called the sclera. The corneal segment is typically about 8 mm (0.3 inch) in radius. The sclerotic chamber constitutes the remaining five-sixths; its radius is typically about 12 mm. The cornea and sclera are connected by a ring called the *limbus*. The iris is the colored circular structure concentrically surrounding the center of the eye, the pupil, which appears to be black.

The dimensions differ among adults by only one or two millimeters; it is remarkably consistent across different ethnicities. The vertical measure, generally less than the horizontal distance, is about 24 mm among adults, at birth about 16–17 mm. The transverse size of a human adult eye is approximately 24.2 mm and the sagittal size is 23.7 mm with no significant difference between sexes and age groups. Strong correlation was found between the transverse diameter and the width of the orbit ( $r = 0.88$ ) [103]. The eyeball grows rapidly, increasing to 22.5–23 mm by three years of age. By age 13, the eye attains its full size. The typical adult eye has an anterior to posterior diameter of 24 mm, a volume of six cm<sup>3</sup>, [104] and a mass of 7.5 grams.

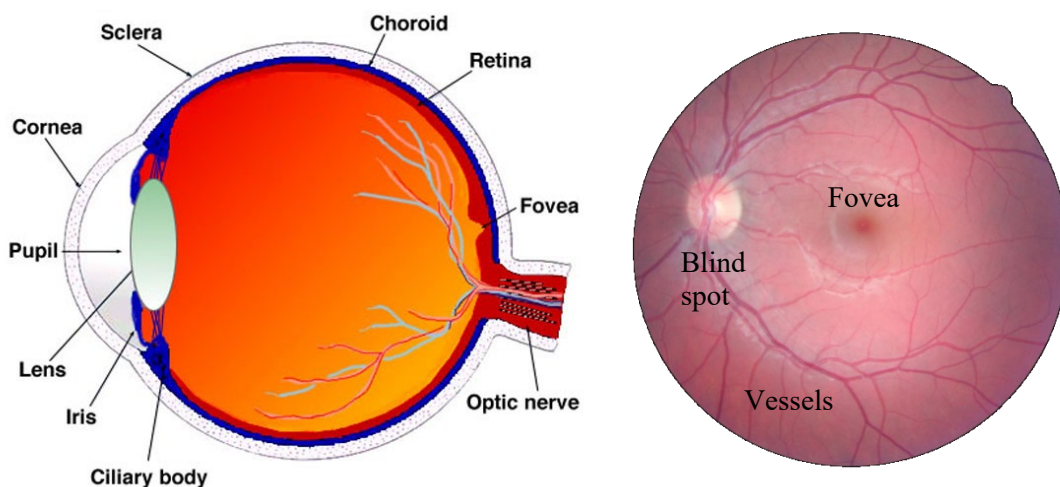


Figure 2.2: Structure of the eye - eyeball (left) and image of retina (right) [44].

### 2.1.1 Iris

Together with the pupil, the iris is responsible for regulating the amount of light that gets into the eye. The muscular iris moves to shrink the pupil if there is too much light and widen it if there is not enough. This is an involuntary function, controlled by the brain. The iris is made almost entirely of connective tissue and smooth muscle fibers.

Despite a common belief, actual change in color of the iris rarely happens. While the color of an eye may appear to change, this is typically due to lighting changes or perception based of nearby colors.

### 2.1.2 Medical use

In medicine, a photographic documentation and subsequent images archiving of retina and iris are necessary for the chronological monitoring process of patient's health condition. It may not be just a disease of these two inner organs of the eye. The iris is a unique tool for tracking of the status of human organism by *iridology* [112] – on this topic, there were posted countless scientific publications, but it is still not clear whether it is a serious science or only a medical fraud [115][102].

The eye retina is the only place on the human body where it is possible to observe vessels by a non-invasive way. The retinal image analysis can be helpful for a diagnostics of eye diseases as well as for making diagnose of diseases related to the cardiovascular system. An automatic and autonomous analysis can be very helpful for making the diagnosis of many diseases, e.g. macular degeneration [114], hypertension [116] and glaucoma [113]. The cardiovascular problems can be detected automatically by the measurement of veins diameters and curvatures [109][110].

### 2.1.3 Biometric use

From the biometric point of view, the eye retina and iris, respectively, are completely unique and have large entropy of biometric information. Moreover, iris and retina are well protected against injuries and external influences. The iris contains a large number of features such as arching ligaments, ridges, crypts, rings etc. Iris is widely used for biometric purposes [105].

On the other hand, the retinal recognition is not so much attractive. Although it is described as one of the safest biometric methods [55], it has several disadvantages. The retina is located on the back of the eye thus it cannot be observed so easily in comparison with eye iris. There must be a complex optical system for image acquisition enabling fully automated user interaction. Currently, there is no biometric device on the market, which is able to perform a retinal biometric identification.

## 2.2 Retina

The retina is considered to be a part of the *central nervous system* (CNS) [1][2]. This is the only part of the CNS that can be observed non-invasively. It is a light-sensitive layer of cells located in the back of the eye with thickness of 0.2-0.4 mm. It is responsible for sensing the light rays that hit it through

the pupil and an eye lens that turns and inverts the image. The only neurons that react directly to light are *photoreceptors* [5]. The optics of the eye creates an image of the visual world on the retina (through the cornea and lens). Light striking the retina initiates a cascade of chemical and electrical events that ultimately trigger nerve impulses. These are sent to various visual centers of the brain through the fibers of the optic nerve. In vertebrate embryonic development, the retina and the optic nerve originate as outgrowths of the developing brain, so the retina is considered part of the CNS and is actually brain tissue. For adults, the retina covers approximately 72 % of the inner eye [1].

The retina is a layered structure with several layers of neurons interconnected by synapses. Photoreceptors have mainly of two types: the rods and cones [3]. *Rods* function mainly in dim light and provide black-and-white vision, while *cones* support daytime vision and the perception of color. A third, much rarer type of photoreceptor, the intrinsically photosensitive ganglion cell, is important for reflexive responses to bright daylight. The entire surface of the retina contains about 7 million cones and 75 to 150 million rods [3]. This would compare the eye to a 157-megapixel camera [1][2].

Neural signals from the rods and cones undergo processing by other neurons of the retina. The output takes the form of action potentials in retinal ganglion cells whose axons form the optic nerve. Several important features of visual perception can be traced to the retinal encoding and processing of light.

The amount of incoming light to the retina is regulated by iris. On the retina is located optic disc and fovea. Fovea is the sharpest-vision place on eye. In this location there are much more cones than in the rest of retina. Optic disc is the point of entry of optical nerves into the eyeball.

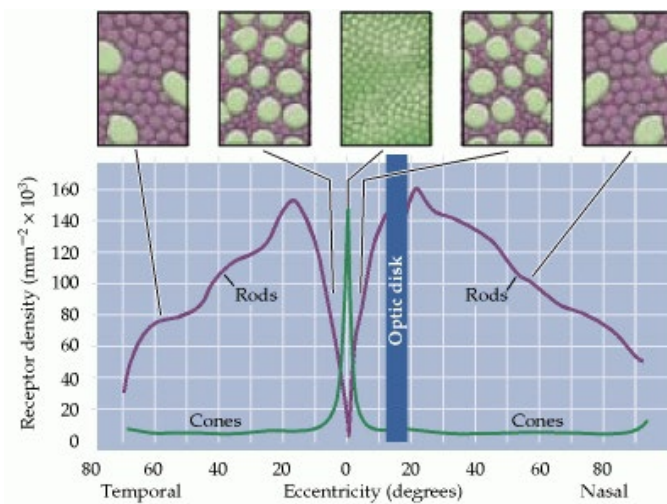


Figure 2.3: Distribution of rods and cones in the human retina. Boxes at top illustrate the appearance of cross sections through the outer segments of the photoreceptors at different eccentricities [36].

As shown in Figure 2.3, cones are present at a low density throughout the retina, with a sharp peak in the center of the fovea. On the other hand, rods are present at high density throughout most of the retina, with a sharp decline in the fovea. The increased density of cones in the fovea is accompanied by a striking reduction in the diameter of their outer segments [36]. Since there are few rods in the fovea, it is less sensitive to light.

We can observe the two most distinctive points on an eye's retina – see Figure 2.4. It is a *optic disc* (or an blind spot) and a *macula* (or yellow spot) [1][2]. An optic disc is the point where the optic nerve enters the eye, has a size of about three mm<sup>2</sup>, and lacks all receptors. Therefore, if the image falls into the optic disc, it will not be visible to a person. The brain often "guesses" how the image should look in order to fill this place. On the other hand, the macula is referred to as the sharpest vision area, has a size of about 5 mm, and the cones predominate it (it is less sensitive to light). This area has the highest concentration of light-sensitive cells whose density is decreasing towards the edges. The center of the macula is *fovea*, which is the term describing receptor concentration and visual acuity. Our direct view is reflected in this area. Interestingly enough, the place called yellow spot is not really yellow, but slightly redder than the surrounding area. This attribute, however, was given by the fact that yellow appears after the death of an individual.

The retina vessels apparatus is similar to the brain, where the structure and venous tangle remain unchanged throughout life. The retina has two main sources of blood supply – the *retinal artery* and *vessels*. Larger blood flow to the retina is through the blood vessel that nourishes its outer layer with photoreceptors. Another blood supply is provided by the retinal artery, which primarily nourishes the inside of the retina. This artery usually has four major branches. The retina located inside the eye is well protected from external influences. During life, the vessel pattern does not change and is therefore suitable for biometric purposes.

The eye iris is out of scope of this chapter, however some interesting works include [65][66][67].

## 2.2.1 Medical basis of vein structure

Formation of retinal vasculature occurs primarily by *angiogenesis* and the factors regulating superficial retinal vascular plexus development in humans are relatively well understood. The vessel regression, sprouting angiogenesis, vascular remodeling and vessel differentiation events involved critically depend on cell-cell signaling between various cellular components such as neurons, glia, endothelial cells, pericytes and immune cells.

Development of the retinal vasculature is preceded by an invasion of migrating astrocytes from the optic nerve into the retina [5]. They stand out from the optic nerve head and extend as a proliferating cell population from center across the inner surface of the retina, forming a cellular mesh-like network that provides a template for the blood vessels in their trace. Before blood vessels cover the astrocytes, they experience hypoxia and strongly express *vascular endothelial growth factor* (VEGF), which is a key stimulus for angiogenesis. The VEGF induces endothelial cells' migration and the expansion of a nascent vascular network over the inner surface of the retina. Once a perfused vascular network has formed, astrocytes gradually downregulate VEGF expression and a typical stellate morphology of the retinal blood vessels emerges. Similarly, the deeper networks of the retinal vasculature are also believed to form by sprouting angiogenesis, in which proliferating endothelial cells form new vessel sprouts and extend the vascular network from pre-existing vessels [24].

There is a strict correlation between the presence of astrocytes and blood vessels in the retina [5]. In primates, retinal astrocytes and blood vessels cover the entire retina, except for the primate fovea from which retinal astrocytes and blood vessels are excluded. Taken together these observations suggest that the retinal astrocyte network and the retinal vasculature are evolutionary and developmentally linked. The process of *retinal angiogenesis* [5] explains why the pattern of retinal vascular network appears quite uniform in the population. Near the disc, the arterioles are more heavily concentrated in the outer choroid, especially nasal and temporal to the disc. The choroidal arteries are wavy or rippled, some like corkscrews, some with one or more 360° loops, and many with rather tightly twisted S-shaped turns [24].

When the outer vessels are gently removed, the smaller vessels are visible. Posteriorly, most prominently in the submacular region, the vessels in the middle layers are highly complicated. Branches are usually not equal in length. The angles formed by two twigs range from 30° to 180°, and T-shaped branchings are common. After the bifurcation, a branch may continue in a straight path, making a sweeping C-shaped curve of 240° to almost 360° and diving inward to enter capillaries only a short distance from the parent trunk [24].

Most of the bifurcations of the larger choroidal arteries are dichotomous, and the very acute angle formed by the offshoots points toward the disc. Second and third branchings may occur almost immediately so that a parent vessel seems to break up, fanlike, into four or six radiating branches after the first branching. Anastomoses between the larger choroidal arteries are not common, but they are frequent in the smaller branches [25].

Additional conditions for branching may be specified by the physics of liquids, high blood pressure or especially the need for blood circulation to and from the areas. According to need of even circulation in all areas, it could be assumed that the sums of the capacities of all vessels will be proportional to the total area. Accordingly, there is probably exists a relationship between different parts of the vascular bed in the retina. Less directly, but with some influence there are also position of bifurcations. Finally, it is necessary to mention that there are also two types of blood vessels - arteries and veins. Logically, how much blood comes through the arteries that much needs to be drained through the veins. It is therefore likely that the vascular beds of both systems will be similarly branched.

## 2.3 Biometric recognition

The retina contains up to 400 features [60], which is many compared to other biometric features. These symptoms include, for example, the size of the optic disc, the relative angles of the major vessels outgoing from the optic disc, or the color patterns of the retina and retinal vascular bed. However, the most reliable and most common are symptoms based on branching and crossing of vessels and their ends in the vascular bed, which are described by the position of the marker or the thickness of the vessel at the marker or in the case of branching [123].

A *biometric recognition system* (BRS) recognizes a person by analyzing the random pattern in his/her physiological or behavioral characteristics known as biometrics which are unique, non-transferable, unforgettable, and always carryable. Among biometric characteristics we can count fingerprint, face, signature, iris, retina, voice, gait, DNA, odor, vein pattern, hand geometry, etc. A BRS has become a usual part of requirements in strictly protected areas such as nuclear plants, military facilities, scientific laboratories, cash vault, border, airport, government office etc., as well as in our day-to-day life such as phone unlocking, building access, online banking, car locking, etc. Comparing to other biometrics, eye biometrics, which include iris and retina [10], offers higher degree of randomness. Even for identical twins the pattern of retinal blood vessels and iris are very distinctive [17][18]. In addition, eye biometrics remain the same for the lifetime of a person. Therefore, the error rate of eye biometrics based BRS is very low. Even though, both eye biometrics offer very high security, the probability of occurrence of counterfeiting is lower in the retina based BRS (RBRS) than the iris based BRS. Because without users' cooperation and special camera like fundus camera or ophthalmoscope, it is not possible to capture retinal image. On the other hand, iris images can be captured by a normal camera at a distance.

In an RBRS, the unique pattern of blood vessels in the retinal image is used to recognize a person. Four kinds of approaches are generally found in the literature for capturing the uniqueness of retinal vessels, among which one approach is matching bifurcations and crossings of the blood vessel structure [40]. *Bifurcation* is the point where one blood vessel divides into two branches and *crossing* is the point where blood vessels visually cross one another. Inspired by the idea of fingerprint minutiae [19][20], Ortega et al., claimed in [21][22] that using of bifurcations and crossings as feature points can overcome the drawback of the RBRS which uses the tree shape pattern of blood vessels of the whole retina proposed by Mariño et al., in [23].

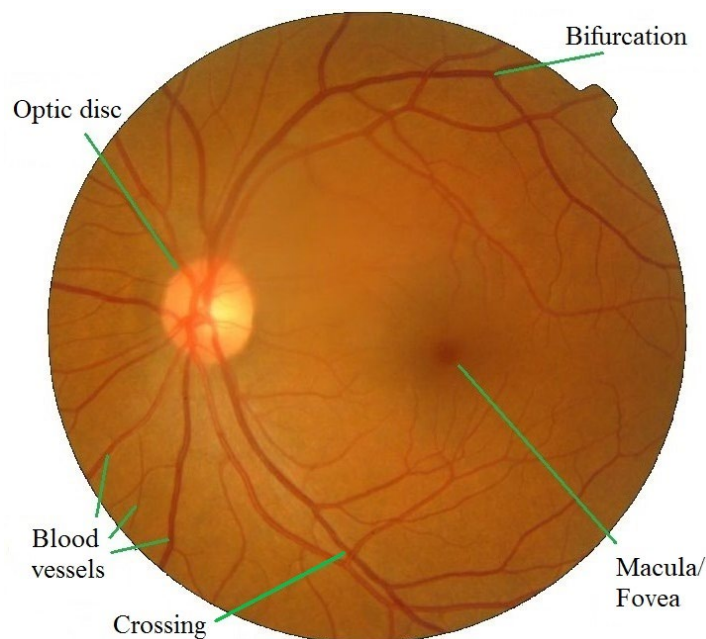


Figure 2.4: Retinal image (own image).

### 2.3.1 Retinal image

One kind of retina scanners is *fundus camera*, which is a specialized microscope with an attached camera. Figure 2.5 shows the fundus camera used in our biometric laboratory of Faculty of Information Technology (FIT) of Brno University of Technology (BUT) in Czech Republic (CZ). No matter which kind of retina scanners is used, without users conscious cooperation the retinal image acquisition is not possible.

Blood vessels coming out from the optic disc with diameter about  $250\ \mu\text{m}$  on average [31][10], make a tree shape on the surface of the retina (shown in Figure 2.4). This tree shape hardly ever changes over the lifetime of an individual and except some severe eye diseases such as hard glaucoma, cataracts, it is not affected by external environment, since the retina is not an external organ comparable to a fingerprint [10]. Moreover, it differs from person to person due to many factors such as the thickness of vessels, the distance from each other, the presence of bifurcations (division points of a single vessel), crossings (intersection points of two or multiple vessels), etc., in different locations and in various amounts.

In order to identify persons by capturing the uniqueness of tree-shaped blood vessels, four kinds of approaches have been proposed to apply [17]:

- using general signal and image processing techniques on the raw retinal images,
- matching of the branching blood vessel structure as a whole,
- matching bifurcations and crossings of the blood vessel structure,
- matching the pattern of vessels traversing a well-defined region.

In all these approaches, storing templates made by features in the training phase, which is accessed in the identification phase, create a database.



Figure 2.5: Fundus camera Canon CR-1 used in the biometric laboratory at FIT BUT.

## 2.4 History of retinal recognition

In 1935, two ophthalmologists, Dr. Carleton Simon and Dr. Isodore Goldstein reported in [42] that every eye has its own totally unique pattern of blood vessels, therefore people can be identified based on the blood vessel patterns in retinal photographs. Subsequently, they published a journal article on the use of vein image in the retina as a unique pattern for identification [42]. Dr. Paul Tower, who in 1955 published an article on studying monozygotic twins [17], supported their research. He discovered that retinal vessel patterns show the least resemblance to all the other patterns examined. At that time, identification based on the vessels in retina was a timeless thought. Their findings boosted research about ophthalmic devices, which can be used, for scanning the retinal blood vessel pattern and result of that research is different types of retina scanners. Fundus cameras photograph the interior surface of the eye, including the retina, retinal vasculature, optic disc, yellow spot, and posterior pole (i.e. the fundus) as shown in Figure 2.4. EyeDentify Co., established in 1976, is considered as the first major vendor of retina scanners [10].

With the concept of a simple fully automated device capable of retrieving a snapshot of the retina and verifying the identity of the user, *Robert Hill*, who established *EyeDentify* in 1975, devoted almost all of his time and effort to this development. However, functional devices did not appear on the market for several years [10][55].

Several other companies attempted to use the available fundus cameras and modify them to retrieve the image of the retina for identification purposes. However, these fundus cameras had several significant disadvantages, such as the relatively complicated alignment of the optical axis, visible light spectra, making the identification quite uncomfortable for the users, and last but not least, the cost of these cameras was very high.

Further experiments led to the use of infrared (IR) illumination, as these beams are almost transparent to the choroid that reflects this radiation to create an image of eye blood vessels [5]. IR illumination is invisible to humans, so there is also no reduction in the pupil diameter when the eye is irradiated. However, it is necessary to pay attention to some wavelengths of infrared lights. The lens absorbs a substantial part of them. Radiation above 1.4  $\mu\text{m}$  wavelength penetrates a maximum of 5 mm deep into the eye and can damage the cornea or lens if is exposed for a long time. The retina can be damaged by infrared light wavelength below 1.4  $\mu\text{m}$  [47].

The first working prototype of the device was built in 1981. The device with an eye-optic camera used to illuminate the IR light was connected to an ordinary personal computer for image capture analysis. After extensive tests, a simple correlation comparison algorithm was chosen as the most appropriate. After another four years of hard work, EyeDentify Inc. launched the *EyeDentificationSystem 7.5*, where verification is performed based on the retina image and the PIN entered by the user with the data stored in the database [10][55].

The last known retinal scanning device to be manufactured by EyeDentify Inc. was the *ICAM 2001*. This device might be able to store up to 3,000 subjects, with a storage capacity of up to 3,300 history transactions [10]. Regrettably, this product was withdrawn from the market because of user non-acceptance and its high price. Some other companies like *Retica Systems Inc.* were working on a prototype of retinal acquisition device for biometric purposes that might be much easier to implement into commercial applications and might be much more user friendly, however even this was a failure and the device did not succeed in the market.

## 2.5 Medical and biometric examination and acquisition tools

First of all, we will start with the description of existing medical devices for retinal examination and acquisition, followed by biometric devices. The medical devices provide a very high quality scans of the retina, however the two major disadvantages are predetermining these devices to fail on the biometric market – firstly, their very high price, which ranges from higher thousands (used devices) up to tens of thousands of euros, secondly to their manual or semi-automatic mode, where medical staff is required. So far, there is no device on the market that can scan the eye retina without user intervention, i.e. fully automatic. We are working on this automatic device, but its price is not yet acceptable for the biometric market.

### 2.5.1 Medical devices

The most commonly used device for examining the retina is a *direct ophthalmoscope* [41]. When using an ophthalmoscope, the patient's eye is examined from a distance of several centimeters through the pupil. Several types of ophthalmoscopes are currently known but the principle is essentially the same: the eye of the investigated data subject and the investigator is in one axis, and the retina is illuminated by a light source from a semipermeable mirror or a mirror with a hole located in the observation axis at an angle of  $50^\circ$  [41]. The disadvantage of a direct ophthalmoscope is a relatively small area of investigation, the need for skill when handling, and patient co-operation.



Figure 2.6: left: Slit lamp example (Optimis Fusion) [56]; right: Non-mydratic fundus camera (Kowa VX-20) [57].

For a more thorough examination of the eye background, the so-called *fundus camera* is used, as shown in Figure 2.6 right, which is currently most likely to have the greatest importance in examining the retina. It allows color photography to capture virtually the entire surface of the retina, as can be seen in Figure 2.4. The optical principle of this device is based on so-called indirect ophthalmoscopy [41]. Fundus cameras are equipped with a white light source to illuminate the retina and then scan it with a CCD (charge-coupled device) sensor. Some types can also find the center of the retina and automatically focus it using a frequency analysis of the scanned image.

The main ophthalmoscopic examination methods of the anterior and posterior parts of the eye include direct and indirect ophthalmoscopy as well as the most widely used examination, a *slit lamp* (see Figure 2.6 on the left), which makes it possible to examine the anterior segment of the eye using so-called *biomicroscopy*. Fundus camera, sometimes referred to as a *retinal camera*, is a special device for displaying the posterior segment of the optic nerve eye, the yellow spots, and the peripheral part of the retina (see Figure 2.6 on the right). It works on the principle of indirect ophthalmoscopy where a source of primary white light is built inside the instrument. Different types of filters can modify the light, and the optical system is focused on the data subject's eye, where it reflects from the retina and points back to the fundus camera lens. There are mydriatic and non-mydriatic types that differ in whether or not the subject's eye must be taken into mydriasis. The purpose of mydriasis is to extend the human eye's pupil so that the "inlet opening" is larger allowing one to be able to read a larger part of the retina. Of course, *non-mydriatic fundus cameras* [48] are preferred because the data subject can immediately leave after the examination and can drive a motor vehicle, which is not possible in the case of mydriasis. However, in some subjects mydriasis is necessary. The price of these medical devices is in the order of from thousands to tens of thousands of euros, which is determined only by medical specialized workplaces. The mechanical construction of the optical device is a rather complex matter [127]. It is clear that the scanning device operates on the principle of medical eye-optic devices. These so-called *retinoscopes*, or fundus cameras, are relatively complicated devices, and the price for them is high as well.

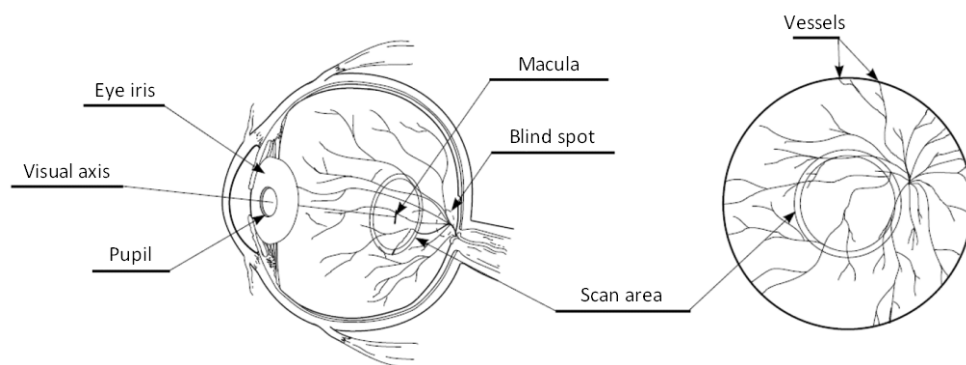


Figure 2.7: Functional principle for obtaining a retinal image of the eye background [49].

The principle is still the same as for a retinoscope, where a beam of light is focused on the retina, and the CCD camera scans the reflected light. The beam of light from the retinoscope is adjusted so that the eye lens focuses on the surface of the retina. This reflects a portion of the transmitted light beam back

to the ophthalmic lens that then readjusts it, the beam leaving the eye at the same angle below which the eye enters (return reflection). In this way, an image of the surface of the eye can be obtained at about  $10^\circ$  around the visual axis, as shown in Figure 2.7. The device performed a circular snapshot of the retina, mainly due to the reflection of light from the cornea, which would be unusable during raster scanning.

## 2.5.2 Device EYRINA

At the end of this subsection, we will devote our attention to our own construction of an interesting and unparalleled device that can be used in both the field of biometric systems and in the field of ophthalmology – we call it EYRINA. This device is a fully automatic non-mydratic fundus camera. Many years ago, we started with a simple device (see Figure 2.8 on the left), but over time we came to the 3<sup>rd</sup> generation of the device (see Figure 2.8 on the right). We are now working on the 4<sup>th</sup> generation of this device that will be completely automatic. The original concept was focused only on the retina (a direct view in the optical axis of the eye), then we arrived (2<sup>nd</sup> generation) to retrieve the retina and the iris of the eye in one device, while the 3<sup>rd</sup> and 4<sup>th</sup> generation are again focused solely on the retina of the eye. The fourth generation can already find the eye in the camera, move the optical system to the center of the image (alignment of the optical axis of the eye and the camera), and take pictures of the eye retina (in the visible spectrum) to shoot a short video (in the infrared spectrum). The 4<sup>th</sup> generation will be able to capture almost the entire ocular background (not just a direct view in the optical axis of the eye) and stitch the image into one file. This will, of course, be associated with software that can already find the macula and optic disc, arteries, and vessels, detect and extract bifurcations and crossings, and find areas with potential pathological findings while we can detect exudates/druses and hemorrhages, including the calculation of their overall area. In the future, we will focus on the reliability and accuracy of detectors and extractors, including other types of illnesses that will be in the interest of ophthalmologists.

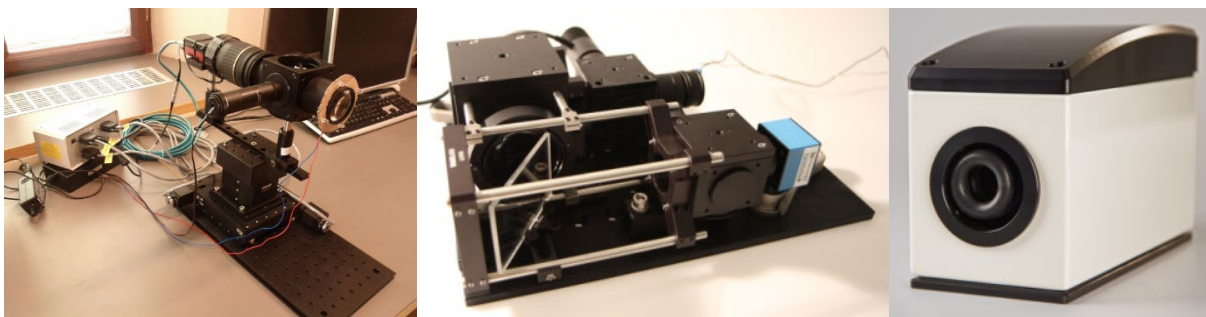


Figure 2.8: A real design 1<sup>st</sup> (left), 2<sup>nd</sup> (middle) and 3<sup>rd</sup> (right) version of the proposed device.

### 2.5.2.1 Design of biometric system based on iris and retina

The device was developed at the Brno University of Technology (CZ). Currently a mechanical design and advanced optical system are under development. We provide brief description of our system in this chapter, together with a short description of current iris and retina biometric approaches and their possibilities of fusion.

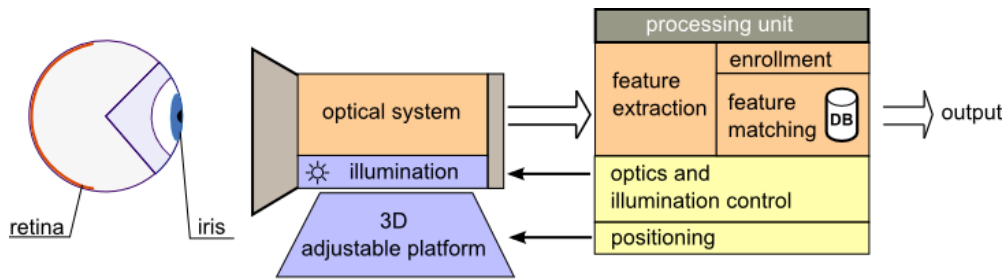


Figure 2.9: The block diagram of proposed system [49].

The optical system is responsible for image acquisition and allows the focusing on iris and retina. Integrated illumination source operates at both visible and near-infrared light. The whole optical system is mounted on an adjustable 3D platform which is controlled by a feedback from the camera image. The positioning algorithm adjusts the optical axis of the device according to the optical axis of the eye. Thanks to the 3D movable platform, we assume that the proposed biometric system will be more user friendly and in addition, the time of scanning will be much less than in case of system described in [37]. Central component of the system is signal-processing unit. It receives and processes output images from the optical system. After evaluation, the unit sends the result to the output (e.g. computer, access system). Fundamental modules of the unit consist of *feature extraction module*, which extracts features from retinal and iris images provided by the optical system. Subsequently a biometric template is generated. An enrolment module allows enrolling a new user to the system. A template is stored in a database located locally on the device or remotely (e.g. via Ethernet connection). *Feature matching module* – matches just extracted template with the templates stored in the database. Optics and illumination control module controls optical system (retina and iris focus, aperture) depending on the feedback from the camera. This module also controls source and intensity of illumination. Positioning module allows to move the optical system in three axes in order to align optical axis of the eye and optical axis of the device. Positioning is controlled by the feedback from the camera image.

Original proposed optical system for this device was described in [93], results are also shown on Figure 2.13. There can be seen iris artefacts, however in some parts the image is blurred due to small depth of field of the optical system. On the same figure the retinal image is rather dark, however there can be clearly seen the optic disc and the blood vessels around. The field of view is comparable with standard fundus cameras. Due to low quality of result images, we divided to propose a new more sophisticated optical setup.

### 2.5.2.2 Optical system

Optical setup itself is designed to fulfill requirements resulting from both physiological properties of a human eye and needs for medical eye examination or biometric pattern recognition. These requirements place emphasis particularly to imaging of relatively large areas of human eye iris and retina combined with computer processing and thus to optical design integrating digital imaging cameras and pertaining optics allowing creation of the image in the plane where the camera active element is placed.

Similar setups were already reported many times [89][90] but the design of one multimodal device represents quite new approach of integration, miniaturization and cost reduction.

Requirements for the optical design were derived from human physiology and – especially in the case of human eye – from the most conventional deviation – refractive disorder (myopia & hyperopia) [50]. Following the interval of these deviations allows us to design the device, which is usable for the vast majority of human population. All these requirements together with the principles of optical imaging were included to the computational model in the ZEMAX<sup>®</sup> environment. The Gullstrand-Le Grand [92] eye model was used to simulate human eye optics during the designing process.

The optical setup, understandably, consist from two essential optical axis which are created by R50T50 plate beam splitter (BS<sub>1</sub>) (Figure 2.10). The BS<sub>1</sub> is the most fundamental part of this novel approach. It allows us to work with two independent optical systems behind the BS<sub>1</sub>. Position of conjugated planes in optical schemas of both iris and retina are designed to do not interfere with the imaging area of other part of the system.

Position of BS<sub>1</sub> relatively close to the eye is the result of contradictory conditions in simulations of both optical branches. One could argue that placement of the BS<sub>1</sub> further from eye could lead to increase of the displayed face area in the iris plane and thus to possibility to use smaller BS<sub>1</sub>, what could lead to lower costs. The second condition – to display sufficiently large area of the retina – however, requires to place main imaging lens (MIL) as close as possible to avoid enormous dimensions (and thus unavailability) of MIL. Therefore, taking into account the costs and available dimensions of elements suitable for BS<sub>1</sub> and MIL, we used rather large BS<sub>1</sub> relatively close to the eye which allows us to use MIL commercially available with acceptable price.

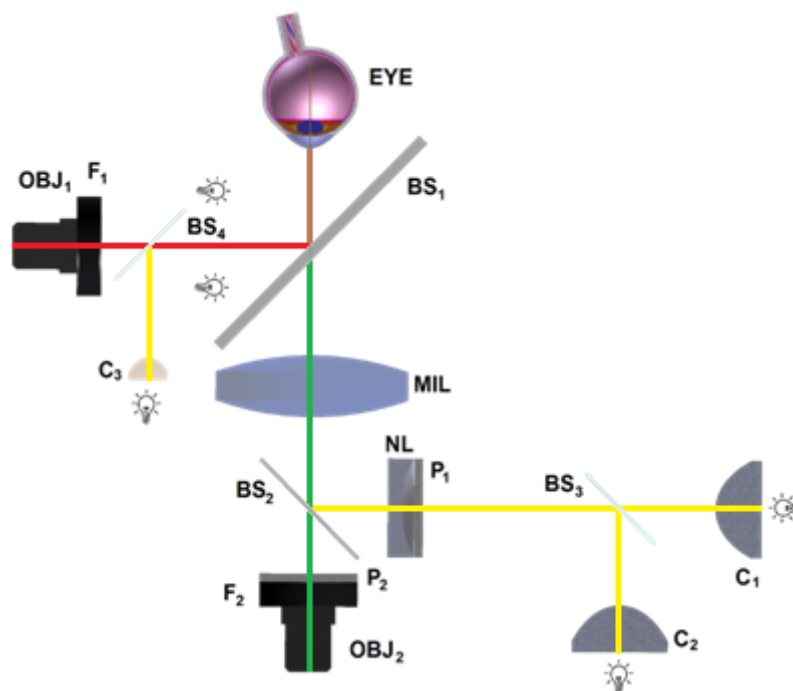


Figure 2.10: Illustrative optical setup of bimodal iris & retina camera. Optical axes of iris (red) and retina (green), imaging and illuminating branches (yellow). BS<sub>1</sub>: main beam splitter; BS<sub>4</sub>: eye navigation beam splitter, C<sub>3</sub>: eye navigation condenses

### **Iris imaging**

The iris imaging in this setup follows classic macrophotography principles and the iris is shown in infrared part of the electromagnetic spectrum [18]. Part of the light scattered from iris (and adjacent part of the face) is reflected on BS<sub>1</sub> and propagates almost unchanged thorough R20T80 beam splitter BS<sub>4</sub>. When light reaches long-pass filter F<sub>1</sub> (edge filter, 800 nm), the part of the spectrum up to 800 nm is cut-off and only infrared part of the spectra pass to the objective. Objective OBJ<sub>1</sub> has focal length 12 mm and F1.6. Objective is mounted to monochromatic autofocus camera (not plotted in the figure) with 1/2.5'' CMOS imaging area and 1.25 mm autofocus range. CMOS technology has sufficient quantum efficiency even in near infrared region, so this camera is an applicable variant.

### **Retina imaging**

The retina could be shown in both infrared and visible part of the light spectrum. The 20D ( $f' = 50$  mm) MIL is used as a cornerstone of the retina-imaging branch. The light scattered from retina propagates via optical system of the eye. Part of it passes through BS<sub>1</sub> and propagates along the optical axis via MIL, R30T70 beam splitter BS<sub>2</sub>, linear polarizer P<sub>2</sub> (to avoid the reflection from eye surface nearly perpendicular to optical axis [89]), short-pass infrared filter F<sub>2</sub> and enters to lens OBJ<sub>2</sub>. OBJ<sub>2</sub> has focal length 8 mm and F1.6. Lens is mounted to color autofocus camera (not plotted in the figure) with 1/2.5'' CMOS imaging area and 1.25 mm autofocus range.

### **Iris illumination**

Iris and adjacent part of the face around the eye is illuminated by infrared (intensity peak: 820 nm) light-emitting diodes (LEDs) placed on illumination ring around the iris-imaging branch's axis (plotted as two light bulbs close to BS<sub>1</sub>). This ring also contains several white LEDs to control the iris aperture for retina imaging purposes. 50 % of light from illuminating ring is reflected by BS<sub>1</sub> on the iris and scattered light can be collected by iris-imaging system.

### **Retina illumination**

Retina is illuminated in IR part of the spectrum by IR (intensity peak: 780 nm) LED placed behind condenser C<sub>1</sub> and in VIS by white LED placed behind condenser C<sub>2</sub>. The light from both LEDs propagates equally via diffuser, doughnut-shaped diaphragm (to remove unwanted light incidents to perpendicular-to-optical-axis surface of the eye) and condenser to create parallel beam of light. Both beams meet on BS<sub>3</sub> and continue together via linear polarizer P<sub>1</sub>. The P<sub>1</sub> changes the illuminating wave to linear polarized and with P<sub>2</sub> (could be understood as analyzer) creates the second hurdle to eye surface reflections. The doughnut-shaped diaphragm is then displayed by negative lens NL and MIL to the iris plane with the diameter slightly smaller than diameter of eye pupil. The light beyond the iris plane creates divergent cone, which creates retina illuminated uniformly enough for the imaging purposes.

## Eye navigation

To keep the eye in the required position during the imaging and possible examination an eye navigation (fixation) system was introduced. White LED along with diffuser, 1 mm aperture and condenser  $C_3$  create small pale dot, which appears for eye placed at infinity. The right position of the source of this eye navigation allows keep the eye axis identical with the iris/retina-imaging axis.

## Required properties

The optical system designed in form described above has properties required from the very beginning. These properties with simulated values are plotted in Table 2.1.

Table 2.1: Properties of proposed optical system – simulation in ZEMAX® environment.

Property	Iris-imaging	Retina-imaging
Displayed area	$65 \times 60 \text{ mm}^2$	$\varnothing 8.0 \text{ mm}$
Resolution	$> 32 \text{ pixels/mm}$	$> 250 \text{ pixels/mm}$
Color depth	monochrome (8 bit)	monochrome (8 bit) color (24 bit)
Possible eye position displacement corrected by autofocus	restricted by retina-imaging branch	$\pm 15 \text{ mm}$
Possible refractive disorders corrected by autofocus	N/A	$\pm 8 \text{ D}$ 90 % of population [91]
Dominant optical aberration	barrel distortion caused by iris curvature	pincushion distortion caused by retina curvature

The central part of the third generation built two tubes with optics that can compensate the diopter distortion approx.  $\pm 10 \text{ D}$  (diopters). The left tube is connected to the motion screw and the NEMA motor, i.e. we were able to move the frontal (left) tube. The eye is very close to the eyebrow holder. Between these two tubes, we have a semipermeable mirror. Under this mirror is a LED diode, which creates a point for, may look at when the eye of patient focused. The illumination unit and a high-resolution camera are placed on the covering unit behind the mirror. The main board and PCBs (printed circuit board) are placed in the back of the fundus camera, with the connectors and cables. The connection is done using a USB (universal serial bus) cable to the computer.

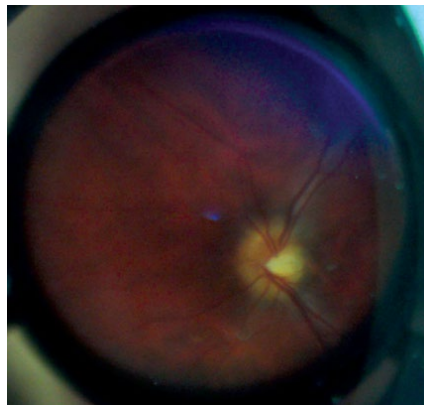


Figure 2.11: Retinal image of a real retina from the 2<sup>nd</sup> version of EYRINA.

The image of a real eye from the second version of EYRINA could be found in Figure 2.11. Now we just use an ophthalmologic eye phantom for version 3.

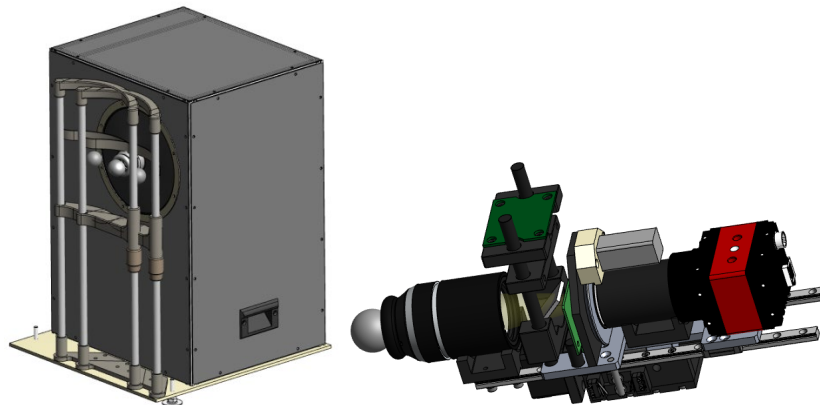


Figure 2.12: Model of the construction of a 4<sup>th</sup> generation device.

Version 3 was able to automatically capture a direct view to the eye, i.e. pupil detection, focusing and taking pictures automatically; however, it is not possible to capture images for retinal images stitching. Moreover, if the user has not centered the optical axis of his/her eye with the optical axis of the camera system, the view to the eye is not correct. The new version 4 has a 5-axes manipulator, which is able to find the centered position of both optical axes (eye and camera) automatically. The other new parts are the compensation of diopter distortion  $\pm 12$  D (with additional rings for up to  $\pm 30$  D), automatic composition of scanned images, automatic recognition of the optic disc, macula, and selected pathologies, and a Wi-Fi/USB connection. The model of the 4<sup>th</sup> version of this fundus camera was finished in autumn 2019. It is visible in Figure 2.12. The result of this model will be presented in chapter 2.5.2.4.

### 2.5.2.3 Experimental Results and Discussion

In the Figure 2.13, the results from our proposed device are shown. On the retinal image there can be clearly seen the optic disc and the blood vessels around. The field of view is comparable with standard fundus cameras. The images were taken in a visible spectrum of light, respectively, by a short-term light pulse to avoid pupil contraction and thus, it resulted in a reduction of field of view.

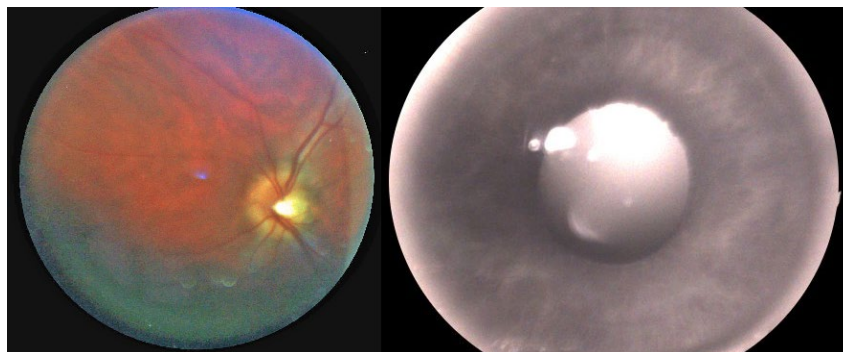


Figure 2.13: Original retinal and iris images from own device EYRINA.

The iris images were taken in infrared light spectrum of 780 nm. There are obvious retinal red and corneal reflexes in the pupil. In addition, some iris artefacts can be seen, however some parts of the image are blurred due to small depth of field of the optical system. This will be solved in the new version of an advanced optical system.

A model of new proposed optical system is shown in the Figure 2.14 although we do not have satisfying results for biometric purposes yet, based on previous experimentation, new results are more promising than older version of optical setup.

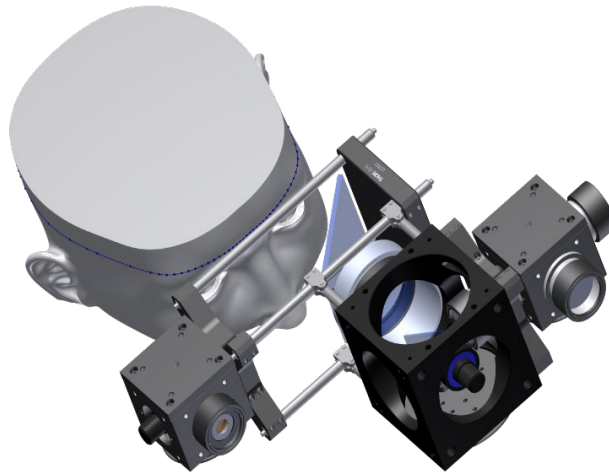


Figure 2.14: Model of experimental setup scaled to human head (2<sup>nd</sup> generation).

#### 2.5.2.4 EYRINA version 4

The device EYRINA, currently in version 4, is a prototyping platform used to develop an autonomous system for sensing and analysing the retina of the human eye. It is a fundus camera mounted on a manipulator, allowing free camera movement and computer control similar to CNC machines.

The basis of the mechanics is a micromanipulator designed for microscopes from TESCAN. It includes linear motion in three basic axes and rotation of the vertical axis (yaw) and side-to-side axis (pitch). This type of freedom allows the camera to be moved and rotated to any reasonable position relative to the front section of the eye. The manipulator is electrically controlled from a main board located in the device, which controls all add-on systems such as camera focus control, lighting built into the camera fundus, and polarizing filter control, among others.

#### Acquisition system

As standard, the fundus camera contains two lenses, before a fixed one used to direct light through the pupil of the eye. The rear one, controllable by a motor, is used to focus the image on the acquisition camera. Between the lenses contains device fixation point, retinal illumination and polarizing filter. The illumination of the retina is realized by means of a ring with embedded LED elements, which is replaceable for the experiments and allows the control of three independent illumination channels. The polarizing filter is used to remove retinal glare, which occurs mainly in younger people, but in older people, it can indicate microvascular abnormalities [94]. For this reason, the polarizing filter is also

motor controllable to allow adjustment of the light polarization angle. The drawing of the optical system of fundus camera can be seen in Figure 2.15.

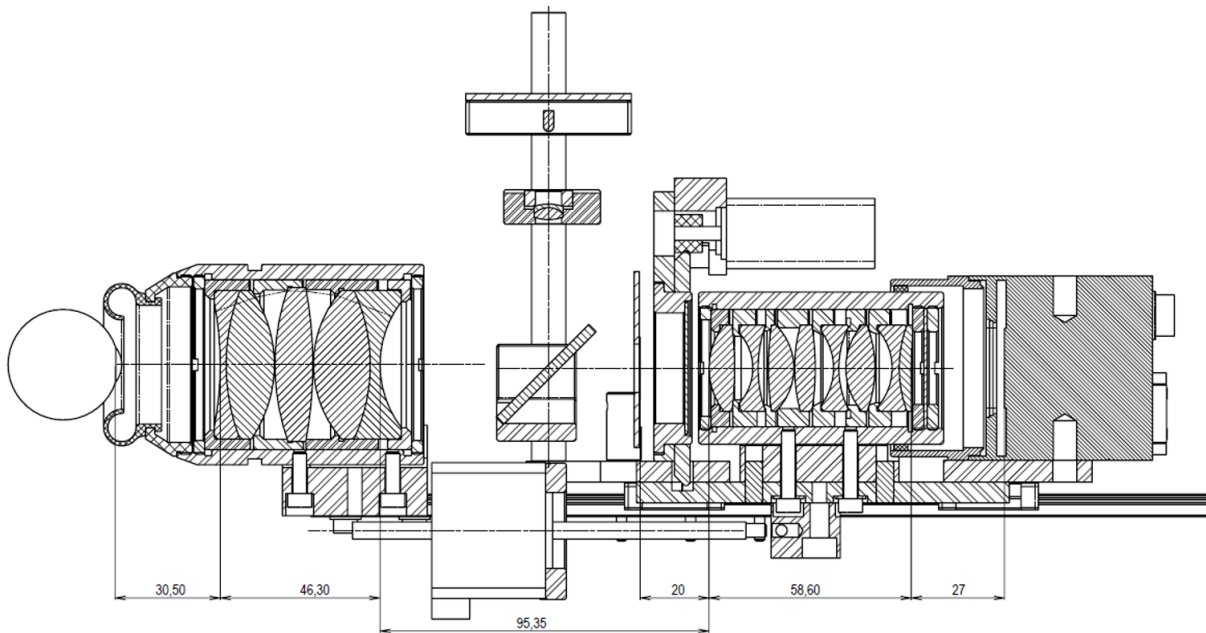


Figure 2.15: Drawing of the optical system of fundus camera EYRINA v.4.

Thanks to the ability of the manipulator to tilt and rotate, it is possible to simultaneously scan the retina not only in plane with the optical axis of the eye but also at an angle, which makes it possible to capture the peripheral areas of the retina where symptoms of diseases may be located. However, as the whole platform is tilted, the fixation point that the person being scanned is also moving, which makes it necessary to move the position of this point so that the optical axis of the eye remains in the same position. The tilt angle is limited by the design of the device and also by the maximum possible angle that can still be compensated by the movable fixation point, which is determined by the characteristics of the front eyepiece and the size of the display. The camera can be tilted by up to  $20^\circ$  in the vertical or horizontal axis, and with the patient's cooperation, the movement of the fixation point can be achieved up to an angle of  $25$  to  $30^\circ$  relative to the original axis of view of the eye.

Allied Vision's color camera, namely Prosilica GT 6400C [95] with Sony IMX342 chip, is used as the fundus camera capture device. The maximum resolution of this camera is 31.4 megapixels, which is a resolution that exceeds that of currently offered high-end fundus cameras from the ZEISS, such as the ZEISS VISUCAM, which has a 24-megapixel camera. However, at full resolution, it is possible to capture at a framerate of 3.8 fps.

### **Illumination**

For the illuminating is used IR part with  $100 \text{ mW/sr}$  and approximate range of 10 cm to cornea of eye. The total irradiance of cornea is  $10 \text{ W/m}^2$ . Which is still below the limit for the lowest safety class device. The benefit of infrared illumination is to highlight certain findings that may be difficult to see under conventional white lighting. Examples of this may be blood spillage under the retina creating

hemorrhages, or spilled vitreous into a tear in the retina. This highlighting under infrared light is caused by absorption of wavelengths of infrared light by the hemoglobin in the blood [96]. Similar highlighting occurs throughout the retinal bloodstream.

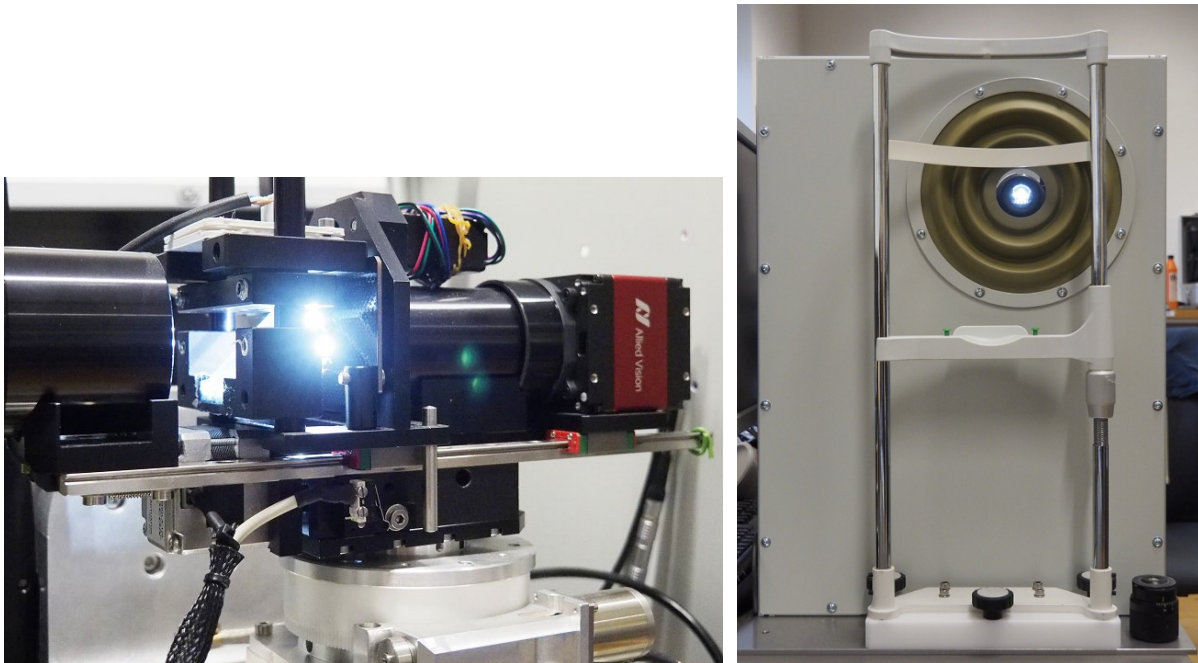


Figure 2.16: EYRINA version 4.

### Eye detection

The subject's head is fixed into the chin and forehead rest. The original position of the device is opposite the opening through which the camera can see out of the device box. In this position, the rear fundus carriage of the camera is moved along with a shift of the entire platform away from the eye. In this position, the camera is focused on the patient's face and has the widest angle of view. Next, the center of the eye is detected, now using a method based on the Timm & Barth algorithm [97]. Which is able to find and track center of eye in images by usage of image gradients. Method has low computational complexity and is invariant to most of the changes in illumination. Once the center of the eye is detected, the platform would be moved and the next cycle would validate the position. Under similar conditions, using significantly inferior optics and camera, it was possible to achieve a detection reliability of up to 97% with minimal deviation from the center of the [124] eye. This phase from initiation to the completion of moving to the center of the eye and approaching it can take around 500 to 2,000 milliseconds depending on how far the eye is deviated from the fundus camera axis.

### Automatic focus

Once the center of the eye is found, the camera is moved to it and the entire fundus camera assembly is moved closer so that the eye itself occupies a larger area of the image. During this move, there is a movement of 5 cm forward in average and thus the plane of focus is shifted behind the eye and the camera needs to be refocused. Contrast calculation is used to determine sharpness using Squared Laplacian which is a method providing good performance and sufficient reliability [98].

At the end of these two procedures, the fundus camera should be pointed at the center of the pupil of the eye and the subject should see the fixation point in the eyepiece (out of focus). At the same time, the fundus camera should be focused on the iris. Alignment of the optical axes is critical, as tilting the manipulator will cause the pupil to appear smaller and as an ellipse. The centering error should be less than 0.2 mm. To correct for this error, which is currently done manually, it is possible to use Terence Brouns' algorithm [99], which allows the pupil and its position to be accurately detected based on the detection of features. However, the disadvantage is the lengthening of the whole process, as it can take around one second. With the improvement of the eye detection accuracy using the Timm & Barth algorithm, the accuracy could be improved and this additional correction might not be necessary.

### **Adaptive retina scanning and stitching**

Although methods based on, for example, direct pixel mapping could be used, as the images will have consistent illumination and scan angle, this is probably the ideal case where the patient will remain perfectly stable throughout the entire scanning. The retinal image also provides a sufficiently contrast image to create features based on gradient, as it does for example with the SIFT method [100]. However, the bloodstream, that is present at least partially in all retinal images, provides scope for a type of feature designed specifically for this particular application and these are features based on the vascular bifurcations and crossings in the bloodstream [101]. These described bifurcations and crossings are then used for matching methods. The most commonly used matching method is Random sample consensus (RANSAC). Since the position of the base images is fixed, it is possible to identify areas of overlap between any two images and look for anomalies (or signs of disease) in these areas. This may involve detection of general anomalies, extending the detection area beyond the most common diseases. If an anomaly is detected, this area can then be added to the image queue to create an image specifically for that potentially problematic area. The overlay of the original image and the newly added image will again be used to detect anomalies and possibly add new images.

## **2.6 Recognition schemes**

The main of not only this part, but also the whole work is determination of the *entropy*. This is one of the important concepts in many areas of theoretical and applied science. It occurs wherever the probability of possible states of a given system is being worked on. It is usually reported as a quantity indicating the "degree of disorder" of the system under study. The notion of entropy as a measure of system uncertainty is more appropriate. Therefore, for example, a normal or uniform probability distribution has a high entropy.

Information entropy (often called the Shannon entropy after Claude Elwood Shannon, who formulated many key findings in theoretical computer science) is very closely related to thermodynamic entropy.

In general, for a system with a finite number of possible states  $S \in \{s_1, s_2, \dots, s_n\}, n < \infty$  and the probability distribution  $P(s_i)$ , the information entropy is defined as the mean value:

$$H(S) = -\sum_{i=1}^n P(s_i) \log_2 P(s_i) \quad (2.1)$$

$(0 \cdot \log_2 0 \equiv 0)$

In short, the information entropy is the mean value of the information of one coded character. The degree of entropy is related to the problem of generating a sequence of random or pseudorandom numbers, because the sequence of completely random numbers should have the maximum degree of entropy. Shannon entropy also forms a limit in lossless data compression [128].

### 2.6.1 Biometric entropy

*Biometric entropy* [59] describes the inherent variability in biometric samples in the population. It can also be understood as the information content of biometric samples is related to many questions in biometric technology. For example, one of the most common biometric questions is that of uniqueness. Such a measure is important for the performance of biometric system, as a measure of the strength of biometric cryptosystems and for privacy measures. It also is relevant for applications such as biometric fusion, where one would like to quantify the biometric information in each system individually, and the potential gain from fusing the systems [38]. For example, biometric entropy of fingerprints is 33 bits and retina is 60 bits [39]. This means  $2^{33}$  or  $2^{60}$  possible combinations. Biometric entropy is a measure of the individuality or randomness or distinctiveness among the biometric templates of different people [17]. Our goal is to estimate biometric entropy of a retina template similar to the work in fingerprints by Zhu et al., [79]. In this paper, we describe our first step in order to achieve our goal by investigating how often bifurcations and crossings occur in different parts of a retinal image.

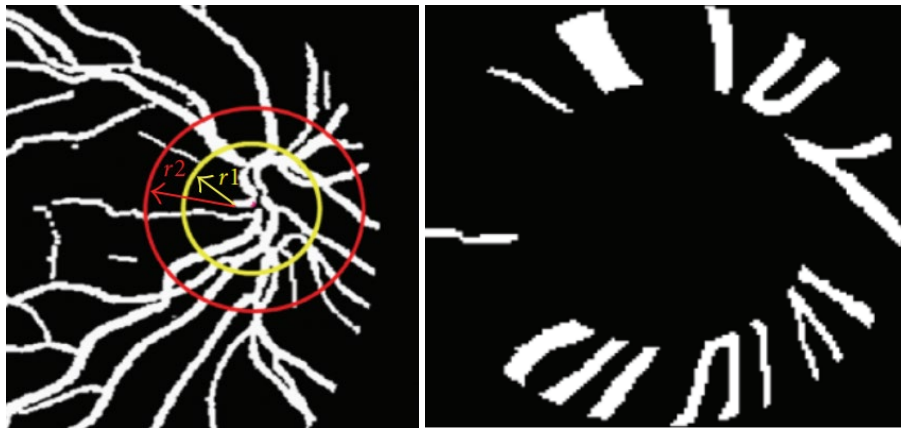


Figure 2.17: Region of interest around optic disc after blood segmentation and masking.

Authors of the related work [40] counted the biometric entropy in annulus around optic disc. Every vessel segment is represented by the triplet: position (in degrees around annulus), width (thickness in degrees) and angle (the angle the segment makes with a radial line from the annulus, passing the centroid of the segment). The result of the biometric entropy was approximately 17 bits [40].

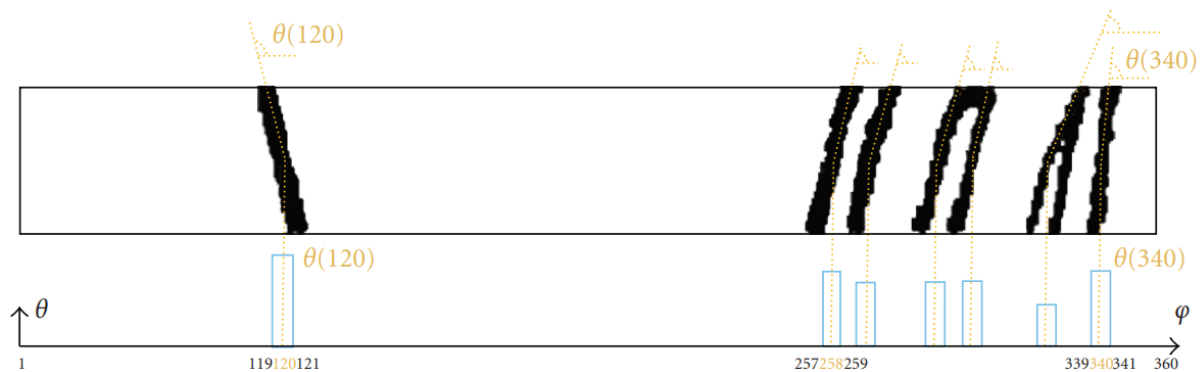


Figure 2.18: Construction of feature vector, the horizontal axis shows the position of vessels (in degrees) in polar coordinates and the vertical axis shows the angle (in degrees) between corresponding vessel orientation and the horizontal axis in the polar image.

In introductory chapter, there is described an overview about existing work on retina recognition. There are several schemes, which could be used for the recognition of retinal images. For example, there are different approaches for retina image biometric recognition. Farzin [10] and Hill [55] segment the blood vessels (Figure 2.17), from which it generates features and stores up to 256 twelve-bit samples reduced to a reference record of 40 bytes for each eye (Figure 2.18). Contrast information is stored in the time domain. Fuhrmann and Uhl [68] extract vessels, from which retina code is obtained. This binary code describes vessels around optic disc. However, as far as we know, there is no previous study that addressed the problem of estimating biometric entropy of retina using statistical models on bifurcations and crossings. Our idea of localization points in the retinal vascular bed is based on the similarity of the structure with the ridges in the fingerprints. There, type (bifurcation and line ending), position and direction of the minutiae are extracted. In retinas, blood vessels are not as severely terminated as in fingerprints, gradually diminishing until lost. Therefore, we do not detect termination. In addition, the complicated structure of several layers of blood vessels over one another is virtually crossing the vessels in the image. It is not easy to know what is crossing and what is bifurcation, so we detect these features together. According to these points, we then perform biometric recognition.

We are also looking for the center of optic disc and fovea (see Figure 2.19). We create a coordinate system with the center in the middle of abscissa between the center of optic disc and center of fovea. The individual points are then represented by the angle and distance in these units, i.e. the results are a set of vectors showing the concrete place in the retinal image. Thus, we are invariant to the different way of acquiring the retina, since the optical axes of the eye and the sensing device may not always be unified.

In the retina the situation is relatively simple because the algorithms are searching the image for *bifurcations* and *crossings* of the retinal vascular system, whose positions clearly define the biometric instance (i.e. the retina pattern). The example is shown in Figure 2.19. Recognition becomes problematic when a stronger pathological phenomenon (e.g. a hemorrhage) occurs in the retina that affects the detection and extraction of bifurcations and crossings. For biometric systems, it should be noted that their use also includes the disclosure of information about their own health status since, as mentioned above, a relatively large amount of information on human health can be read from the image of an iris,

and that is especially so from a retina as well. It is therefore up to each of us on how much we will protect this private information and whether or not we will use the systems. However, if the manufacturer guarantees that the health information does not get stored, and only the unique features are stored (not the image) in the template, then the system may be used based on data protection legislation (e.g. GDPR) [30].

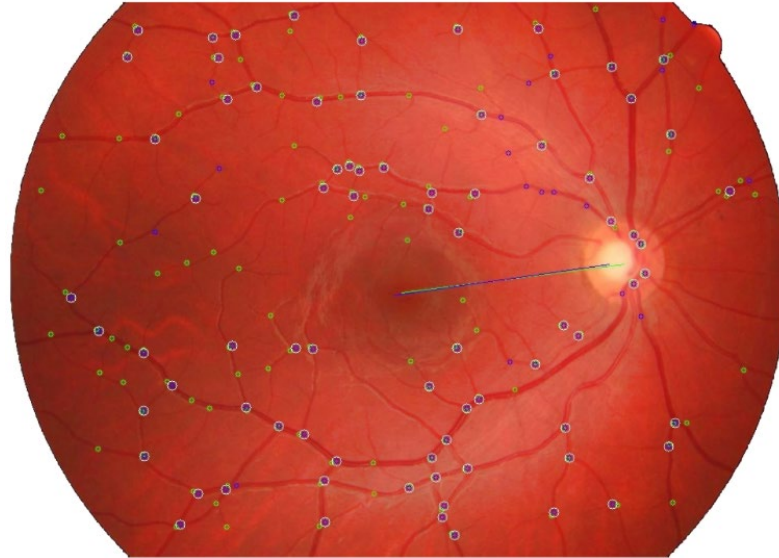


Figure 2.19: Extracted features (bifurcations and crossings, incl. connection of macula and optic disc) in the retina [126].

## 2.7 Limitations

Some limitations in retinal biometrics discourage greater use in biometric systems. There is currently no system that can remove these shortcomings to a greater extent [55]:

- *Fear of eye damage* – the low level of infrared illumination used in this type of device is completely harmless to the eye, but there is a myth among the lay public that these devices can damage the retina. All users need to be familiar with the system in order to gain confidence.
- *Outdoor and indoor use* – small pupils can increase the false reject rate. Since the light has to pass through the pupil twice (once in the eye, secondly outwards), the return beam can be significantly weakened if the user's pupil is too small.
- *Ergonomics* – the need to come close to the sensor may reduce the comfort of using the device.
- *Severe astigmatism* – data subjects with visual impairment (astigmatism) are unable to focus the eye onto the point (a function comparable to measuring the focusing ability of the eye for an ophthalmologist), thus avoiding the correct generation of the template.
- *High price* – it can be assumed that the price of the device, especially the retroviral optical device itself, will always be greater than, for example, the price of fingerprint or voice recognition capture devices.

The use of retinal recognition is appropriate in areas with *high security requirements* such as nuclear development, arms development, as well as manufacturing, government and military bases, and other critical infrastructures.

## 3 Retinal diseases and their effects

The main focus is on ophthalmology in regard to examining the retina of the eye, of course taking into account the overall health of the eye (e.g. cataracts or increased intraocular pressure). In the retina, there is a relatively large line of diseases and damages that interest medical doctors, but they are detailed in an encyclopedia of ophthalmology with hundreds of pages (e.g. [7] (1,638 pages) or [5] (2,731 pages)). The large group is diabetes and age-related macular degeneration (ARMD). Occasionally exudates/druses or hemorrhages (bleeding or blood clots) appear in the retina, however, as mentioned above, potential damage (e.g. perforation or retinal detachment) or retinal disease is such a matter. We will be interested in diseases that visually affect the retina and therefore can affect the recognition of people based on this biometric feature. Biometric entropy thus increases, but it is not the way we would expect to increase value. From a statistical point of view, it is instead a limitation of the different situation of points [4].

This work and the developed programs do not only try to detect diseases. Detectors can correct minor visual manifestations on the retina for biometric processing. And tools for automatic disease detection are also being developed in collaboration with ophthalmologists.

### 3.1 Retinal diseases

In comparison with other biometric characteristics (e.g. fingerprints, vascular pattern of hand or finger), the role of diseases connected to a concrete biometric information carrier (e.g. finger, hand) plays a very important role. It is not only the ageing factor, which can bring some changes into the retinal image sample, however the pathologies on retina can disable the subject to use the biometric system. The most common disease manifestations are related to diabetes mellitus and ARMD, whereas these pathologies (e.g. hemorrhages and aneurisms) can change the quality of the image so much that the vascular pattern is partially covered or completely not visible [6]. Therefore, a short description of the most important and the mostly widespread retinal diseases are mentioned and shortly described to get the feeling how much they can decrease the biometric performance of the recognition algorithms.

#### 3.1.1 Diabetes mellitus

*Diabetes mellitus (DM, diabetes)* [6] is a disease characterized by elevated blood glucose (hyperglycemia) due to the relative or absolute lack of insulin [5] – the hormone produced in Langerhans' pancreatic islets. Chronic hyperglycemia is associated with long-lasting damage, dysfunction and failure of various organs of the human body – especially eyes, kidneys, heart and blood vessels. The consequences of long-term diabetes include diabetic retinopathy with possible loss of vision, nephropathy leading to renal failure, peripheral neuropathy with the risk of ulceration in the lower limbs

or amputation. Patients with diabetes also have a more frequent occurrence of cardiovascular disease and susceptibility to high blood pressure (hypertension).

### **3.1.1.1 Classification**

The vast majority of diabetes types [6] fall into two broader categories, type 1 and type 2 diabetes. In patients with diabetes, first type is the cause of the disease produced by insulin deficiency. This is caused by an autoimmune process resulting in the destruction of insulin-producing  $\beta$ -cells Langerhans islets of the pancreas [46].

In the predominant category of diabetes of the second type, the cause of the insulin secretion is impaired by  $\beta$ -cell paclitaxel and insulin resistance, which results in a decrease in the effect of insulin in the target tissues [6].

### **3.1.2 Diabetic retinopathy**

While diabetes mellitus (diabetes) has been described in ancient times, *diabetic retinopathy* [8][9] is a disease discovered relatively late. Diabetic retinopathy (DR) is the most common vascular disease of the retina. It is a very common late complication of diabetes. It usually occurs after more than 10 years of diabetes. The better the way diabetes is compensated, the more complicated the eye complications occur later. Approximately 2 % of all diabetic patients become blind due to retinopathy. In industrially developed countries, the most common cause of the blindness of working-age people and in view of the constant increase in the number of diabetics, diabetic retinopathy is a serious health and social problem. Statistics show that diabetic blinded by retinopathy does not survive an average of five years after the disease of the body (the kidneys, the heart, the brain).

Diabetic retinopathy occurs in several stages. The first stage can only be detected by fluorophotometry. The next stage is called *simple, incipient, or non-proliferative diabetic retinopathy* (NPDR). It is characterized by the formation of small micro-aneurysms, which often crack and result in another typical symptom – the formation of small intraretinal or pre-retinal hemorrhages. With blood, however, high-molecular proteins, such as fibrin and fibronectin, come into the retina. Micro-aneurysms are not a physiological form, blood is often precipitated in them, and their clogging often occurs, which can lead to obliteration of the capillary. The process leads to the formation of hypoxia – microinfarcts of the retina, which is manifested as if on the retina lying with wadding. Microinfarcts have a white color, a fibrous structure and are therefore also referred to as "cotton stains". If the capillary obliteration is repeated at the same site, heavy exudates arise. They are a sign of chronic oxygen deficiency. They are yellow, sharply bounded, and are formed by fat-filled cells [9]. Due to the lack of oxygen in the corresponding area of the retinal tissue, the retina reacts with the formation of new vessels in order to ensure sufficient oxygen. This stage is called *proliferative diabetic retinopathy* (PDR). Newly formed vessels are pathological (disease-related), growing up in the wrong place – in the front of the retina. Not only do they not bring oxygen to the retina but have catastrophic consequences for the eye. They are

very fragile, often bleeding into the glass. The resulting blood deposits prevent the retina from picking up the image [8][9].

### **3.1.2.1 Diabetic retinopathy manifestations on retinal images**

Pictures of the retina may have diabetic retinopathy symptoms in multiple forms. We will introduce only the most important ones.

#### **Microaneurysms**

*Microaneurysms* (MA) [8][9] are considered to be basic manifestations of diabetic retinopathy. Although micro-aneurysms are characteristic of diabetic retinopathy, they cannot be considered a pathognomic finding for this disease. They can manifest in many other diseases. MA are the first lesions of the DR that are proved by biomicroscopic examination. The flowing MA leads to the formation of edema and annularly deposited exudates. Their size is between  $12\ \mu\text{m}$  to  $100\ \mu\text{m}$ . These are round dark red dots, which are very difficult to distinguish from microhemorrhagia. Unlike these, they should have more bordered edges. If their size is greater than  $125\ \mu\text{m}$ , it must be taken into account that they may be microhemorrhagia. As mentioned above, their color is similar to the vascular pattern and there is expected to influence the biometric recognition performance.

Microaneurysm can affect automatic image processing and consequently biometric identification seemingly insignificantly. Small microaneurysm have the same color as the vessels, and if one appears near the vessel, the site may be identified as a bifurcation, or two bifurcations.

#### **Hemorrhage**

Depending on the location in the retina, we distinguish hemorrhage intraretinally and subretinal [8][9]. *Hemorrhages* occur secondarily as a result of rupture of microaneurysms, veins and capillaries. Spotted hemorrhages are tiny, round red dots and are kept at the level of capillaries and only exceptionally deeper (see Figure 3.1). Their shape is dependent on their location, but also on the origin of the bleeding. Sometimes they are surrounded by a fine ring of dye. This phenomenon reminds the stains of the hemorrhagic position of the newly cracked microaneurysm. Spataneous hemorrhages have a characteristic appearance of stains and their color is light red to dark. Pataloid hemorrhages are deposited in the retinal surfaces of the retina and have the appearance of rich flower planks. Their shape resembles the shape of the chrysanthemum. They are mostly on the retina periphery. In the neighborhood, micro-aneurysms are often found. Cracked hemorrhages are caused by bleeding from newly created vessels. If the source of bleeding stops alone, the blood is absorbed very quickly. As mentioned above, their color is similar to the vascular pattern and is expected they influence the biometric recognition performance. The vessels detector may replace hemorrhage as a part of the vessel, and after the transfer to vessels mask, the area can be evaluated as two parallel vessels. Thus are added two bifurcations to biometric recognition. A similar detection problem can occur with very strong vessels.

## Exudates

*Hard exudates* (Figure 3.1) [8][9] are not only characteristic of diabetic retinopathy. They are also found in many other diseases. Hard exudates are deposits of lipids, proteins and fibrin in different layers of the sensory part of the retina. Hard dotted exudates are round, clear yellow dots. They create different clusters with a pronounced tendency to migrate. Hard exudates are predominantly surface-shaped and have the shape of a hump. Placoid hard exudates occur in the foveal area where they cause a marked decrease in visual acuity. Hard exudates can generally be spontaneously reabsorbed. The color of this pathology is different from the vascular structure, so it does not affect the biometric recognition performance, but it can affect the ability of preprocessing algorithms to prepare the image for venous structure extraction.

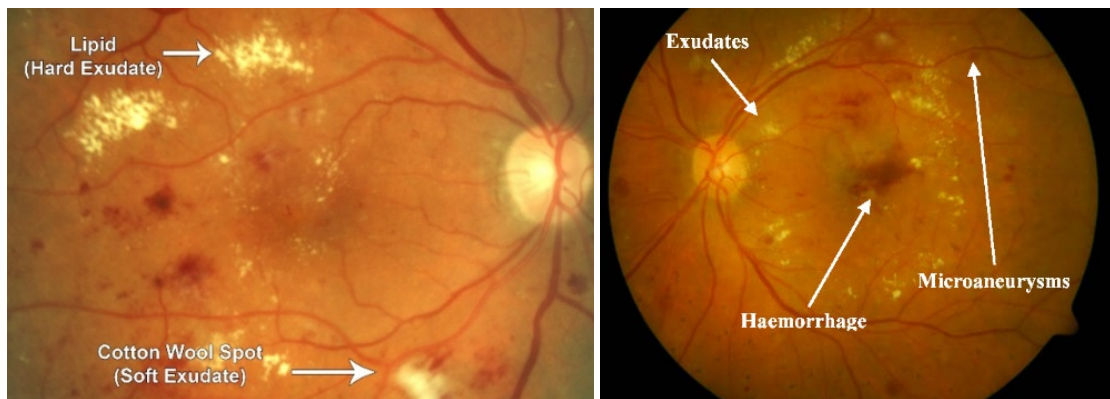


Figure 3.1: Hard and soft exudates (left) [61] and hemorrhage and micro-aneurysms (right) [62].

*Soft exudates* (Figure 3.1) [8][9] are considered to be a typical manifestation of diabetic retinopathy, but can also be found in other diseases. They result from arteriolar occlusions (closures) in the nervous retinal layer. They are often accompanied by plague-like hemorrhage. Along the edges, there are often extended capillaries. The color of this pathology is different from the venous structure, so it does not affect the biometric recognition performance, but it can affect the ability of preprocessing algorithms to prepare the image for venous structure extraction.

Although the exudates have a significantly different color, they can easily cover relatively large parts of the image. In the case of a larger number of exudates, biometric identification may also be impossible.

### 3.1.3 Age-related macular degeneration

*Age-related macular degeneration* (ARMD) [11][12][13] is a disease that has been over the last decade. This is a multifactorial disease – many factors affect this. In addition to age, cigarette smoking, improper nutrition, obesity, diabetes mellitus, hypertension (high blood pressure), oxidative stress, gender, race, heritage, and others may be the cause [5]. However, the only reliably proven cause of ARMD development is age, therefore this diagnosis is particularly affected by older patients. There are also physiological processes that are natural and disease-causing (ARMD). These processes can affect

all macular structures. ARMD is characterized by a group of lesions, among which we classically include accumulation of deposits in the depth of the retina – druses, neovascularization, fluid bleeding, fluid accumulation and geographic atrophy.

### **3.1.3.1 Classification of ARMD**

Based on clinical manifestations, we distinguish between dry (atrophic, non-exudative) and wet (exudative, neovascular) disease [11][12][13]. The dry form affects less than 90 % of patients and about 10 % moist. However, the moist form is much more serious because it can very quickly and easily disrupt the anatomical arrangement of the macula and thus also the central visual functions (sharpness, color, contrast sensitivity adaptation to light conditions, etc.). Both forms can be combined during the illness.

ARMD can manifest itself in very different ways. In most cases, it is an overlap of a relatively large part of the retina. On the other hand, if it overlaps the most sensitive part of the retina - the fovea, where the vessels are the finest and the detector does not find any important points for identification, the changes in the biometric template may be relatively small.

#### **Dry form**

It is caused by the extinction of capillaries. The affected person complains of a gradual decrease in visual acuity associated with metamorphosis (enlarged / diminished image). Problems are mostly reflected in reading. Clinical findings found in the dry form of ARMD include druses, changes in pigmentation, and some degree of atrophy. Terminal stage is called *geographic atrophy* [46]. As an early stage of dry form, we find the finding (in patients over 50 years) of some of the symptoms: soft druses, areas of hyperpigmentation associated with druses, or areas of hypopigmentation associated with druses. The *druses* [5] are directly visible yellowish deposits at the depth of the retina, corresponding to the accumulation of pathological material in the inner retinal layers. They contain neutral fats and phospholipids around the perimeter. The druses vary in size, shape, appearance. Depending on the type, we distinguish between soft and hard druses.

*Soft druses* [5] are larger and have a "soft look". They also have a distinct thickness and a tendency to collapse. Depending on the size, we describe small and large druses. Druses that are less than half the diameter of the vein at the edge of the target are referred to as small (up to 63  $\mu m$ ) and respond to hard druses. Druses  $\geq 125 \mu m$  are large and respond to soft druses.

*Hard druses* [5] are not ophthalmoscopically trapped up to 30-50  $\mu m$ . Better are visible in red-free light. These can be clearly demonstrated by fluorescence angiography. In a smaller amount, this is probably a physiological condition. The pseudo-soft druses are initially small; they are growing in time, coming close to each other until the appearance of fading. This can be excluded by photographic (red-free) or fluorescence angiography. The cluster size does not exceed 250  $\mu m$ . *Beginning atrophy* [46] precedes the final stage (geographical atrophy). Using autofluorescence and its changes, it is possible to monitor the rate and direction of atrophy propagation, thus predicting the risk of visual acuity deterioration and

visual field changes. We observe it as a region of hypopigmentation RPE (*retinal pigment epithelium*) [46], the retinal tract appears to be more pink than the surrounding background, and the druses in this area tends to be pale and harder. *Geographic atrophy* [14] (Figure 3.3) is the final stage of the dry, atrophic form of ARMD (Figure 3.2). It appears as a sharp borderline oval or circular hypopigmentation to depigmentation or direct absence of retinal pigment epithelium. Initially, atrophy is only light, localized and gradually spreads often in the horseshoe shape around the foveola. The development of atrophy is related to the presence of druses and, in particular, their collapse or disappearance [11][12][13].



Figure 3.2: ARMD – soft druses (left), ARMD – hard druses (right) [12].

### Moist form

It is caused by the growth of newly formed vessels from the vasculature that spreads below the Bruch membrane [46]. In the Bruch membrane, cracks are created by which the newly created vessels penetrate under the pigment tissue and later under the retina. These newly created vessels have pathologically increased permeability, i.e. increased fluid transduction under the retina. Vessels are fragile and often bleed into the sub-retinal space. The leakage and bleeding stimulate the formation of fibrous tissue and in the macula forms a connective tissue called pseudotumor or disciform macular degeneration. Compared to dry form, the change in wet form is faster and more dramatic. The main symptoms of the wet form include blurred vision, image distortion, and disturbance of sharp vision, especially close [11][12][13].

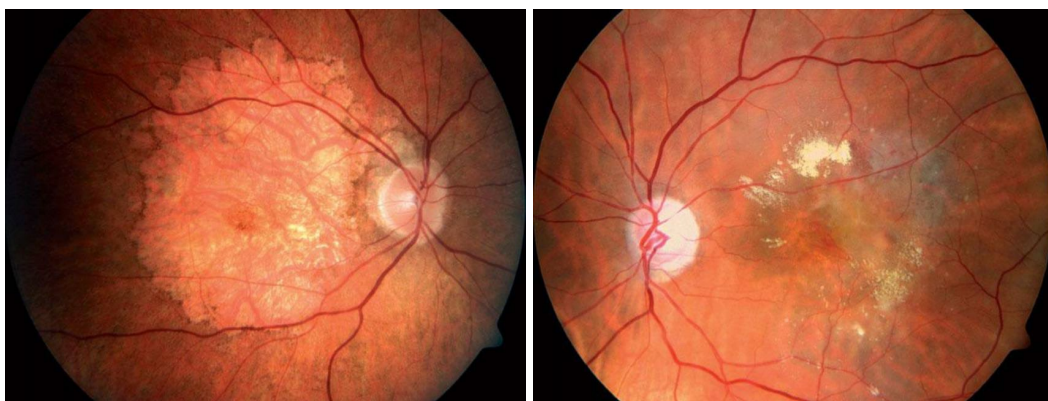


Figure 3.3: Geographic atrophy (left) [12]; wet form with edema (right) [15].

In this case, soft and hard druses are not comparable in color and shape with vascular pattern in retinal images, however they can influence the image preprocessing algorithms, which are preparing the image for extraction of the vascular pattern. Herewith the biometric recognition performance can drop down, however it is not a big change. All the algorithms for retinal image preprocessing should be adopted to treat such diseases to be able to reliably extract the vascular pattern.

### 3.1.4 Retinal detachment

This is a very serious illness that can affect a person at any age, more common in the middle and elderly decades of life. There are flashing eyes, small dots, or dark shadow in the field of view. The retinal detachment of the eye occurs when a variety of cracks appear in the retina, causing the vitreous fluid to get under the retina and lift it up (thereby removing the retina from the pigment cell layer). As a result, nutrients and oxygen do not get into the retina, so cells present in the retina die quickly. Most often, this detachment occurs at the edge of the retina, but from there it slowly moves to the center of vision when untreated. In some cases, retinal detachment has also caused the wrinkle of the vitreous, which usually occurs in the aging process. During aging, sometimes in the case of injury or myopia or inflammation, may cause to create small deposits in the retina, which can create a new connection between the vitreous and the retina. These connections cause the part of the retinal tissue to escape when the shrinkage increases. If a physician discovers cracks or holes in the retina before the deviation occurs, laser coagulation is used to connect the retina to the other layers of the eye wall. However, if the retinal detachment has already occurred, the only solution is surgery under general anesthesia [13][16]. This disease totally destroys concrete (up the complete) parts of the retina, whereas the vascular pattern is lifted and moved in space, i.e. the original structure before and after this disease is so much different that the subject will not be recognized using a biometric system based on retinal images (Figure 3.4).

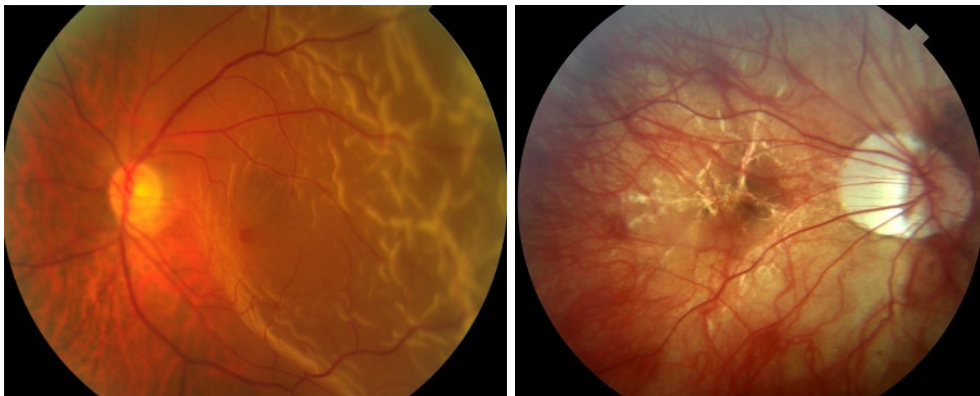


Figure 3.4: Retinal detachment (left) [63]; retinal (lacquer) crack (right) [64].

In the case of the other mentioned diseases, in addition to the already mentioned overlap of the retina, other visual lines may also appear which after detection are then considered as vessels on which many more crossings appear.

### 3.1.5 Cracked retina

The retina can crack in the eye of a person for various reasons. This may be due to the complications of another eye disease, it may be a degenerative form of eye disease, or it can also occur when eye or brain injury occurs. This cracking usually occurs because the retina is not properly perfused for a long time. The effect of rupture may also be due to the age of eyeballs. If there are small cracks in the retina, the patient may not be aware of any visual problems, but he may still notice various symptoms such as bright flashing in front of the eyes, narrowing of the visible field, and more. However, if the retina of the eye is disturbed more severely, it can lead to significant visual impairment, as well as loss of vision. Treatment of cracks can be done using laser, cryotherapy and surgery. The physician always decides on the form of treatment depending on the extent, type and location of the crack (Figure 3.4) [13][16].

It means that the venous system beneath the top layer of the retina begins to intermingle, i.e. a new venous structure appears in the retinal image that is difficult to distinguish from the top layer, disabling recognition from the originally stored biometric template. However, it is possible to create a new biometric template in the actual status of the disease that is adapted to the current status after every successful biometric verification.

### 3.1.6 Retinal inflammation

This disease is also known as *retinitis* [5]. It appears with blurred vision and moving spots in the field of vision. Typical is also high sensitivity to light and tearing. Inflammation of the retina of the eye can cause viruses and parasites, but the most common cause is bacteria. The patient's infection into the retina can get blood from the inflammatory deposit virtually anywhere in the body. The retina may become inflamed even after an accident or if the infection is directly in the eye (for example, eye flushing). When the body heals the infection, the immune cells also damage the cells in the retina, which can lead to visual impairment. In many cases, inflammation of the retina is not isolated and is accompanied by inflammation of the blood vessel, which holds the retina with blood. The doctor usually prescribes antibiotics to treat eye retinal inflammation, and in more serious cases it may also prescribe corticosteroids. Usually it depends on what caused the inflammation. Of course, antibiotics are not prescribed when the disease is caused by viruses, in which case antiviral agents are used [13][16].

Retinitis creates new and distinctive patterns, mostly dark in color, which greatly complicate the extraction of the venous structure, thus having a very strong influence on biometric recognition performance.

### 3.1.7 Retinal swelling

Swelling of the retina, or diabetic macular edema [5], affects diabetics, as the name suggests. This swelling occurs after leakage of the macula by the fluid. Retinal swelling causes the ability to feel light diminishes. As a result, the patient has a blurred vision and is unable to focus on the eye. This swelling

may occur for data subjects who suffer from long-term diabetes, or if they have too high glucose levels during treatment. Swelling is caused by damage to the retina and its surroundings. These catheters then release the fluid into the retina, where it accumulates, causing swelling [13][16].

If treatment fails, the retinal swelling can lead to complete loss of vision. Treatment of retinal swelling has to be done depending on the treatment of diabetes, where the blood sugar level is maintained at appropriate levels. Swelling of the retina is usually treated with laser eye surgery, the laser burns the leaking blood vessels, and thus closed up.

The influence to biometric recognition performance is comparable with the manifestation of retinal detachment – the structure is changed in space having impact to the position of vascular system in the retinal layer.

### **3.1.8 Circulatory disorders of the retina**

Relatively frequent diseases of the retina are circulatory disorders, where the retinal vessel closes. These closures arise mostly as a result of arteriosclerosis, which is a degenerative vascular disease where it is narrowing and a lower blood supply to tissues. The formation of arteriosclerosis is supported by some general diseases such as high blood pressure, diabetes, fat metabolism disorders, etc. [13][16].

*Central vision artery occlusion* [71] causes a sudden deterioration in vision. On the ocular background, there is a narrowed artery, retinal dyspnea and swelling. It is important that the treatment be started on time, preferably within two hours of the first symptoms. Drugs for vascular enlargement, thrombus dissolving medicines and blood clotting drugs are applied. In spite of timely treatment, retinal function is often reduced [13][16].

*Closure of the central retinal vein* [72] is manifested by rapid deterioration of vision, thrombus causes vein overpressure, vein enlargement is irregular and retinal bleeding occurs. Drugs are used to enlarge the blood vessels, after time the thrombi are absorbed, or the circulatory conditions in the retina are improved by laser [13][16].

Circulatory disorders always have a very significant effect on the color of the cardiovascular system, making the veins and arteries very difficult to detect, especially when the vessel is combined with its hemorrhage. In this case, it is not possible to reliably detect and extract the venous system, thereby dramatically reducing biometric recognition performance. Even image preprocessing algorithms will not cope with this problem.

## **3.2 Automatic retina processing**

The next part of this chapter discusses our developed detectors of diseases in eye retina images. We have a database (and we still get new images) with retinal diseases. We introduced our own software solution for detecting and localizing hemorrhages and druses. Disease notification then can modify behavior of the biometric systems when evaluating data subjects. In this subchapter, we discuss

pathologies, which could be detected in retinal images taken by patients in hospitals. This software is a supporting tool for medical doctors, however in connection with the device described in subsection 2.5.2 gives a quick information about health status of the user.

This chapter will introduce an approach of detecting symptoms of human eye retina and its implementation. Parts of this chapter have already been published as final theses together with our research group [117][118][119][120][121]. Because the retina contains various structures (yellow spot, optic disc and blood vessels) that do not present disease and could adversely affect the result, they should also be detected and omitted from the whole disease detection process. In this way, the accuracy of this algorithm will increase. The order of each subchapter corresponds to the algorithm processing steps.

The first steps described can be used also for other detections on healthy retinas, which will be described later. For example, extraction of the vascular bed to find points of intersection and bifurcation of individual vessels. Detection should also include the detection of previously mentioned diseases, because they can affect biometric recognition and also the calculation of biometric entropy itself. Most crossings and bifurcations are still visible and in the same places, but some diseases may overlap the detected points or create new ones.

### 3.2.1 Pre-processing

For every processed image, its resolution is changed before further processing. The main reason is to speed up the calculation, where the total number of pixels to be processed is reduced, thus reducing the number of calculations to be made. Another advantage is the setting of parameters for individual calculations of each image. If all the input images are converted to a certain resolution interval, there is no need to define these parameters for too wide resolution. In this case, the image width ranges from 2,500 pixels to 900 pixels, which was selected. If a wide-angle input has a pixel amount greater than 2,500 pixels, its resolution is reduced. To create one new pixel, four original pixels are required. In this way, the resolution of the image will be reduced to half and keeping the aspect ratio. Conversely, if an input image is narrower than 900 pixels, its resolution is doubled. If any of the images fall into this interval, they are kept unchanged. The next step is to determine the above-mentioned calculation parameters. These include the size of the filter matrix for retrieving the background mask (filter 1) and the filter matrix size for further processing (filter 2). These parameters are determined based on three categories that are given by the width of the input images. An overview of these values can be found in Table 3.1. Adjusting the resolution of the input image should fall into one of these categories.

*Table 3.1: Overview of algorithm calculation parameters.*

Image width (in pixels)	Filter 1 (in pixels)	Filter 2 (in pixels)
2,500–1,951	9×9	13×13
1,950–1,401	7×7	11×11
1,400–900	5×5	9×9

### 3.2.2 Obtaining a background mask

The main reason why it is necessary to separate the background from the foreground is the efficiency. Excluding the background from the next processing will speed up the overall calculation. Another reason is the unwanted background noise, which could be detrimental to the detection process. Each background can be of different shape and size, and color is not uniform as well. That's the reason why we focused on detecting by the sharp edge background interface and the retinal image.

In order to automatically separate the background mask from the retina, it is necessary to first convert the default image to gray, apply smoothing to it by averaging a standard mask of the size given by filter 1 (see Table 3.1) and then selecting the threshold value that will allow this separation. For some images the background not pure black, which can cause problems in properly separating the mask from the effective part of the image. For this reason, this value is calculated for each image separately.

First of all, squares are obtained from each corner of the image, where the side length of each area is equal to one-tenth of the height of the image. Subsequently, the average intensity of each area is calculated and then the average of the four intensities is calculated. Finally, this diameter is rounded off and added to the value 5. This gives the threshold size. Subsequent thresholds will have the correct background separation from the foreground. However, if certain objects appear in the background, such as marking an image, these unwanted elements need to be removed. This is done by looking for contours in the acquired mask, where the largest contour belongs to the retina. This will be left and the other contours will be discarded. When consulting Figure 3.5, it is at first sight clear which part of the image belongs to the background and which to retina.

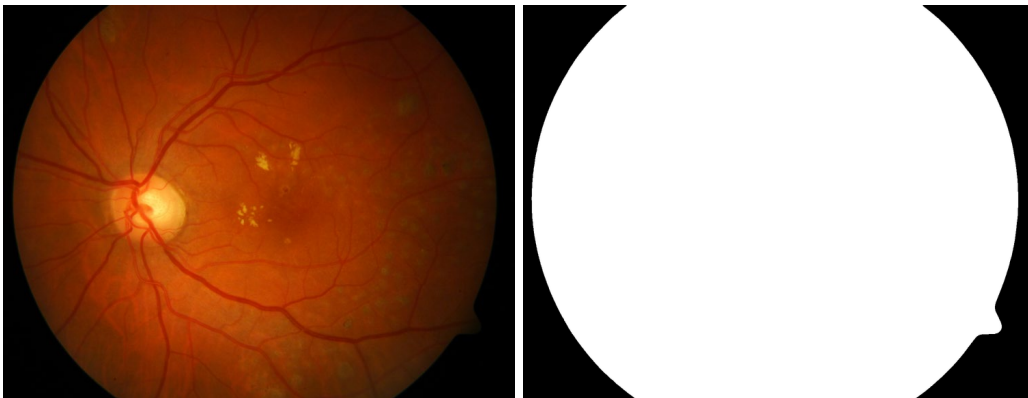


Figure 3.5: Default image (left); Background mask (right).

### 3.2.3 Obtaining properties of the retina

For further steps in the algorithm, it is necessary to obtain the basic properties of the region of the retina, such as the center and the radius of the area. For this purpose, a Hough's transformation [70] is used to find circles. This algorithm for extracting properties is computationally challenging, but the appropriate setting of limit values where the circles are to be searched will make the overall calculation significantly faster. These limits include the minimum distance between the centers of individual circles and the minimum and maximum radius. As the minimum distance between centers, a larger value is

chosen from the number of rows and the number of columns in the slide where it is assumed that the required circle will be only one. It also follows that its average cannot be greater than the number of those rows or columns. By dividing that number by two we get the maximal radius. The minimal radius is calculated from the formula for the content of the circle where the content is determined by the size of the retina. If the background mask is not available and the whole image is filled with the retina, the center of the image is working, and the larger the number of rows and the number of columns is chosen as the radius.

### 3.2.4 Optical disc detection

Heavy exudates look similar to an optic disc. It may happen that they are changed with the detection and therefore need to be detected and excluded from further processing. The optical disc is approximately oval, which often has the highest intensity in the retina. Thanks to this feature, we can detect it. However, the problem cause druses and exudate, which may be similar or even more intense than the optical disc. For this reason, the size of the optic disc must also be considered. After experimenting with the image database, the optical disc radius was determined to be one-seventh of the radius of the retina. Therefore, an area with a certain area of the brightest pixels is searched.

For automatic detection of the optic disc, it is necessary to process a default image. A green component of RGB (red, green, blue) color model is extracted from it, showing the contrast of structures on the retina and its background (see Figure 3.3). The detection algorithm calculates the area in which it will be searched. A band forms it across the width of the image with a height corresponding to one-fifth of the diameter of the retina. This strip can be seen in Figure 3.6. The reason for reducing the area in which the optical disc is searched is to eliminate possibilities of the wrong detection. Once this area has been obtained, smoothing is performed by means of a standardized filter 2 (see Table 3.1).

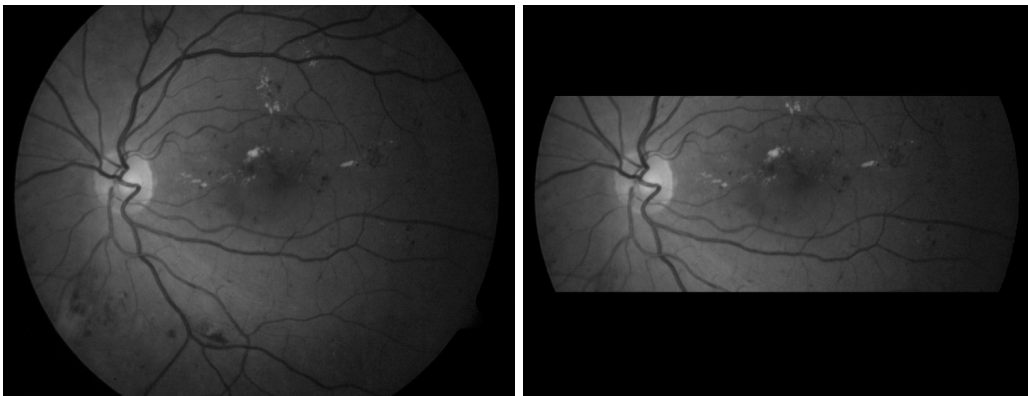


Figure 3.6: *Extracted green channel (left); taper region (right).*

Detection is based on a cyclical binary threshold that starts at a maximum of 255 and gradually decreases that threshold. After each threshold, the contours of the obtained areas are searched in the image to calculate their content. A contour that contains at least 11 times more pixels than the radius of the retina is calculated by the circle that describes it. If its radius is less than or equal to 1.2 times the radius of the optical disc, this area belongs to it. We have achieved these values by experimenting on the database of

the most successful images. The result of the last threshold is shown in Figure 3.7 left. Then we calculate the center of gravity of the acquired area that will serve as the center of the optical disc. Based on the location of this area, it is determined whether it is the right or left eye of the data subject, and accordingly, the center moves two-fifths of its radius in the given direction. The result is shown in Figure 3.7 right.

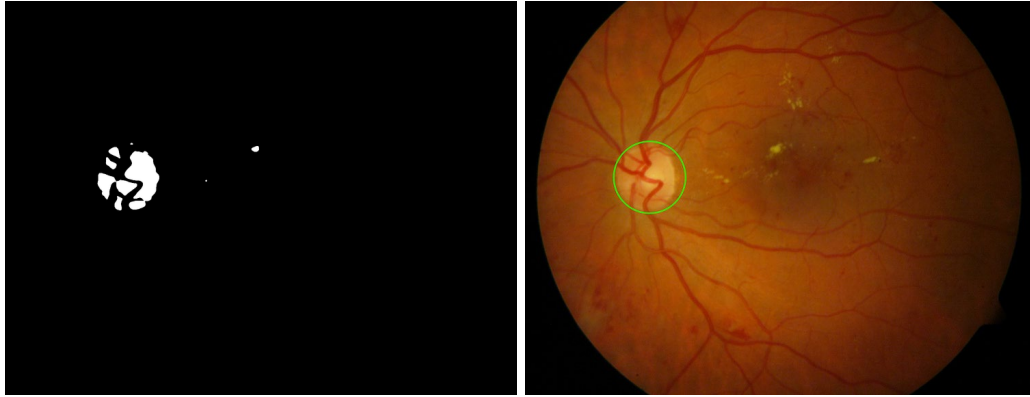


Figure 3.7: End of binary thresholding (left); detected optical disc (right).

To obtain a more accurate mask of the optic disc, including the smaller areas it belongs to, an additional processing is performed. From the default green channel, the computed area of the optical disc (see Figure 3.8 left) is extracted, on averaged with a standard 5×5 pixel mask. Subsequently, one threshold is made with a threshold value of 2 lower than the threshold at which the optical disc area was found. In this way, much better results will be achieved. The difference can be seen in Figure 3.8 middle and right.



Figure 3.8: Optical disc area (left); found area (middle); resultant mask (right).

### 3.2.5 Fovea detection

In order to correctly classify symptoms of ARMD, you need to detect a fovea. Another reason why the fovea should be detected is the possibility of assessing the severity of the disease, as mentioned earlier, fovea is the structure of the retina, representing the place of the sharpest vision. As a result, it has the greatest impact on the quality of vision and injury of this area is significantly reducing it. Fovea is a circular or oval area, which is opposed to the optic disc by one of the darkest spots on the retina. This, in some cases, may lead to erroneous detection when the fovea merges with the background of the picture or when the retina is severely damaged. In retinal images, the fovea always occurs relatively in the same place relative to the optic disc, approximately two and a half times its width [58].

When fovea is detected, the green source channel is again working. From this, the area under consideration is determined by moving the center of the optical disc only to a distance of two and a quarter of its diameter. This is because the radius of the optical disc is calculated to include an area slightly larger than the disc itself. The radius of the examined area is then two times the radius of the optical disc (see Figure 3.9).

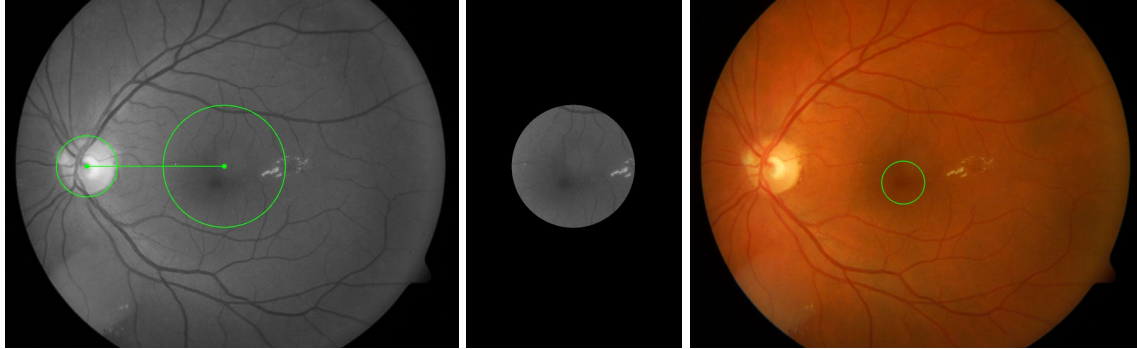


Figure 3.9: Green channel (left); Determined fovea area (middle); Detection result (right).

The studied area is then smoothed out by a standardized filter 2 (see Table 3.1). The fovea detection itself is based, similarly to the detection of an optical disc on a cyclic binary threshold, with the difference that the threshold value starts at zero and gradually increases. The size of the search area also has an upper limit. The lower limit is 6 times greater than the radius of the retina, and the upper limit is 2.4 times greater than the lower limit. These values were also obtained by experimenting with the database of images. The first area that falls within these limits is fovea. The result is shown in Figure 3.9 (right).

### 3.2.6 Blood stream detection

Detection of symptoms of the disease on the retina occasionally has the problem of some parts of the blood stream appearing to be a finding. The reason was the size of the vessel, its shape, and intensity in poorly illuminated images or extensive retinal damage. The initial measure was an additional check to see if it was a part of the bloodstream. However, it was not very successful, because despite the fact that a part of the mistakes detected had been eliminated, many of them still remained. With this low success, we needed to find solutions elsewhere. Very good results compared to the previous procedure were achieved in the detection of retinal blood flow and its exclusion from the obtained results.

First of all, a background mask is applied to the default image (Figure 3.5 left), which eliminates the area beyond our interest, and then extracts the green channel. As mentioned above, the contrast of the retina background and the structures found on it, including the bloodstream can be clearly seen on the green channel. This Gaussian adaptive threshold is applied to this channel, which transforms the image in grayscale into a binary image. The threshold is calculated individually for each pixel where this calculation is obtained by weighted sum of the neighboring pixels of the given pixel from which a certain constant is deduced. Together with the size of each pixel, it represents Gaussian adaptive thresholding parameters. The smaller the environment, the more sensitive this method is to small units and the greater

the environment, the smaller the formations are lost from the result. If the pixel environment is too small, areas that do not belong to the bloodstream and may contain any findings may also be included in the results. Therefore, it is important to choose the size of the environment so that the result is sufficiently detailed and at the same time that there are not too many correct areas. After experimenting with different images, we chose parameters 49 for the size of the surroundings and 3 for the subtracted constant. These values have achieved the best results (Figure 3.10 left).

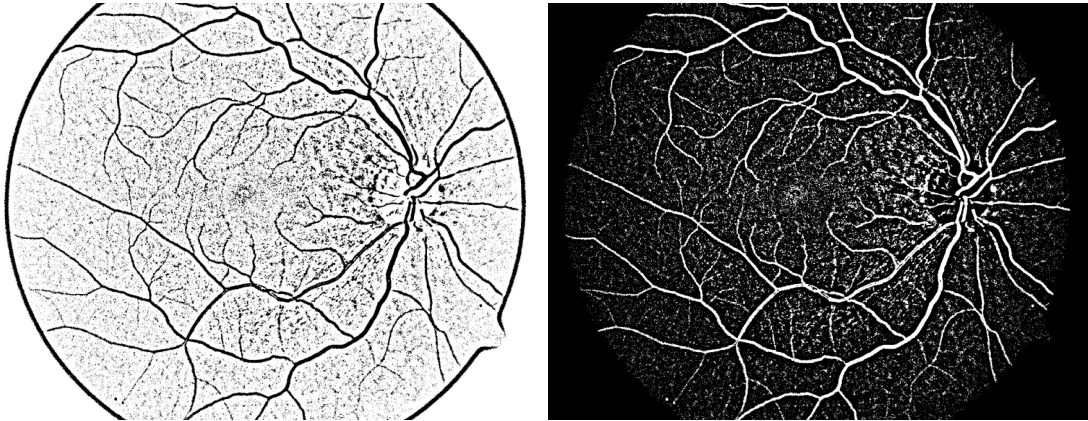


Figure 3.10: Gaussian adaptive thresholding (left); inverted threshold output (right).

The threshold output also includes the border region between the retina and the background image that was improperly detected. We will get rid of this area by re-applying the background mask. First, however, the image is inverted because it requires further processing, and if the mask applied first, it would also invert it and then apply it again. The mask has to be adjusted before it can be used, since the border area in some cases slightly extends into the retina. To remove this overlapping part, the retina erosion is performed in the mask. The result of this processing can be seen in Figure 3.10 right. It is now followed by median smoothing with a  $5 \times 5$  matrix size that reduces salt and pepper noise type. The resulting image will once again undergo this smoothing with the same matrix. This will help to further reduce unwanted areas of the image (see Figure 3.11 left).

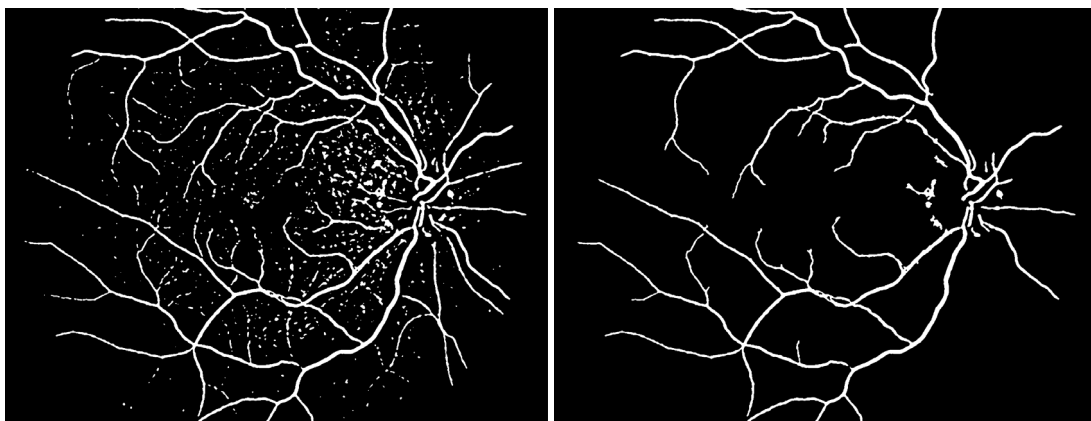


Figure 3.11: Second median smoothing (left); seed filling (right).

To obtain the resulting mask of the bloodstream, seed filling begins with the vessels in the optic disc. For this reason, it is necessary to calculate the set of starting points (seeds) and the parameters of the

optic disc that has already been detected are used for this. Firstly, a new mask containing a circle around an optic disc is created, which is then bit-multiplied by the Gaussian adaptive threshold output. New lines are now detected by Hough's transformation. In the area of the optical disc, the vessels have the largest diameter, so this property is used to find these lines by specifying their minimum length. Now there is a series of seed fill, which uses the centers of the detected lines as starting points. The result after this operation is visible in Figure 3.11 right.

Adaptive thresholding and smoothing of the original image in the bloodstream detection process may disrupt the vascular continuity and therefore some parts of the bloodstream are not included in the resulting mask. To prevent the loss of these vessels, a mask (see Figure 3.12 left) from which the bloodstream was extracted by seed filling, undergoes further processing. This includes finding the remaining areas and their classification to determine whether it is a part of the bloodstream or other object. The first criterion examined is the content of the area. If the content is greater than 4,500, the aspect ratio of the smallest rectangle bounded by the given area is calculated, and if this ratio is greater than or equal to 8, it is a part of the vessel, otherwise it is discarded. If the content is greater than 1,600, areas with an aspect ratio greater than 10 are left, otherwise the average width of the area is calculated, and if it is less than 6.8 (which would roughly correspond to the width of the vessel), the area remains, otherwise it is discarded. If the content is greater than 300, the aspect ratio is again calculated for the area, and if it is greater than or equal to 5, it is a part of the vessel, otherwise it is discarded. Other areas containing less than 300 are discarded. The overall result of blood flow detection is shown in Figure 3.12 right.

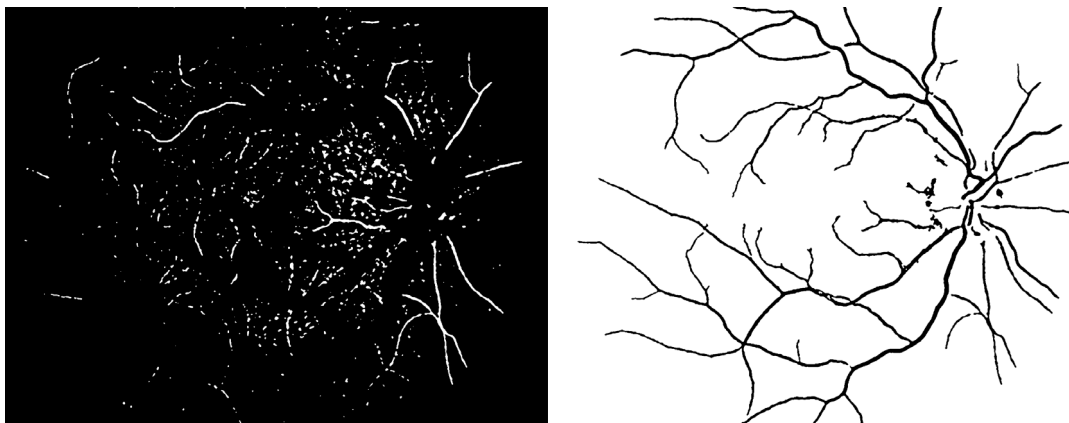


Figure 3.12: Missing vessel mask (left); blood flow detection (right).

### 3.3 Automatic disease detection

One of the problems of biometric recognition is the possibility of some diseases affecting the biometric feature of the retina. In this case, the person may not be correctly recognized or identified. One possibility is to detect these diseases and remove the affected parts of the image from the biometric template. The following paragraphs describe possible procedures for these detections, which can also be used for medical purposes. For example, if the following algorithms were implemented in the

scanning device, the scanned subject may be alerted to the possibility of the disease before coming to the ophthalmologist. In this case, it would have to be ensured that this information is communicated only to the scanned person and is not stored. This is very sensitive medical information.

Some diseases are more common, so there is the possibility of more approaches to the detection of visual manifestations. For comparison, we enclose individual methods for finding areas damaged by diseases.

### 3.3.1 Detection of druses and exudates

Due to the lack of images with ARMD during the creation of this work, the images with exudates will be used as well. Druses arising from ARMD are very similar to those exudates that occur in diabetic retinopathy. For this reason, it is possible to detect these findings with the same algorithm. In both cases, there are fatty substances deposited on the retina, which have a high intensity yellow color. Their number, shape, size and position on the retina differ from patient to patient.

#### 3.3.1.1 Hard exudates detection

Hard exudates, as opposed to soft ones, have very pronounced edges, which greatly affected the resulting algorithm. The first step in the detection is the already mentioned modification of the retinal image. Subsequently, a Gaussian anti-aliasing algorithm is used, which removes excess noise from the image. Adaptive thresholding, in particular Gauss adaptive thresholding, is applied to the image thus modified. This step will provide us with candidate areas where exudates could be located. This threshold works very similarly to classical adaptive threshold, but the threshold values are calculated from the environment based on Gaussian values. To find suitable candidate areas, the most difficult part of the algorithm development was to find the right way of thresholding. Gaussian thresholding gives the best results among the tested algorithms. After choosing the algorithm, it was still necessary to choose the best size of the area from which the threshold value will be calculated. The best results are summarized in Table 3.2.

The smaller area proved to be insufficient and very few exudates were detected. Conversely, when using areas with a larger area to be treated, too many areas where no exudates were found were detected. An important part of the algorithm is to remove places where there are no exudates from the candidate areas. This elimination is performed by morphological operations.

Table 3.2: Overview of filters used in the detection of hard exudates.

Image size	Below 2,000×2,000	Above 2,000×2,000
Gaussian filtration	13×13	13×13
Gaussian thresholding	11×11, $\sigma = -1$	71×71, $\sigma = -20$ and 11×11, $\sigma = -1$
Median filtration	5×5	5×5
Morphological opening	2×2	2×2
Morphological dilatation	4×4	4×4

After obtaining the candidate areas, those that overlap with the locations located in the pre-prepared mask, are removed from the image. Thus, all candidate areas that are close to the veins, background, or optical disc are removed. After the removal of these areas, there are still many places that are marked as candidates, but there are no exudates. These areas are almost always very small, where more contrast was accidentally created. Median smoothing and subsequent morphological opening surgery are used to remove these areas. The size of the areas used by the algorithms in the calculation was obtained from experiments and extensive testing so that the results were as good as possible. Subsequently, a morphological dilation operation is used to restore the objects to their previous size. The detected areas usually do not have a completely exact shape like the original exudates in the image, but in our case the number, size and location of these exudates are important. After this step, we get a map of the hard exudates found in the picture, if there are any.

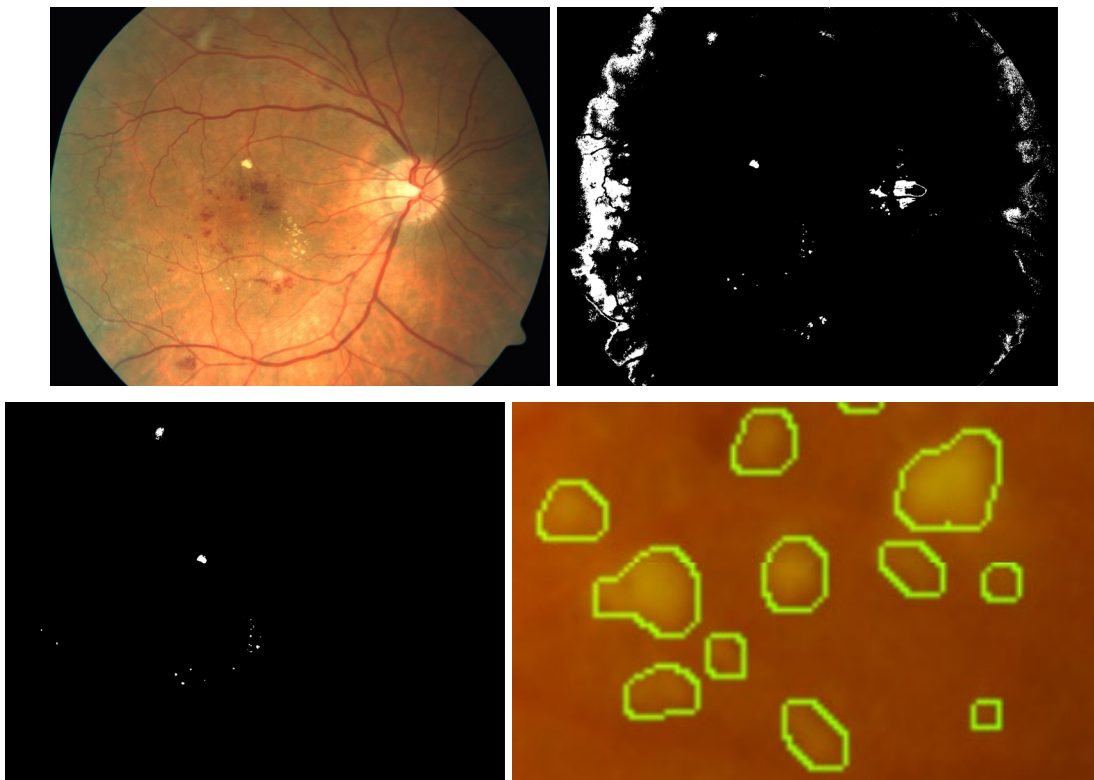


Figure 3.13: Original image (top left); first detection (top right); after filter bad areas (bottom left); example of detected hard exudates (bottom right).

In cases where the part with the occurrence of exudate is less sharp, it may not be marked. However, after reducing the sensitivity, many more false areas are detected. For this reason, we had to add a method to the algorithm that additionally removes all detected areas in which no exudates occur.

The advantage of this method is that it also serves to obtain more precise edges of the detected areas with exudates. We experimentally found that the exudates have a range of color values in the HSV [73] as follows: Hue in the range of 11-50, Saturation 100-255, Value 50-255. These values are filtered from the original image, and then the AND operation is applied to the filtered image and to the image with detected areas. This step removes areas that do not meet the color range. The range of values adapts to

each image based on the average colors in that image. This procedure has proven to be very effective in removing poorly detected areas, but also in refining the results. Figure 3.13 shows the operation of this procedure.

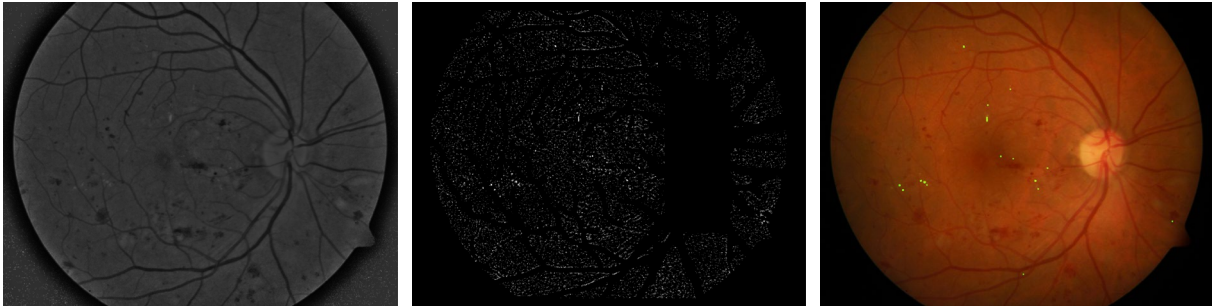


Figure 3.14: Image after adjustment (left); before application of opening and dilatation operations (middle); result (right).

### 3.3.1.2 Soft exudates detection

Soft exudates [5] are larger cotton wool deposits. In the images, the retinas are yellow, but in most cases their color is less pronounced than in the case of hard exudates. As they are also yellow, their detection is complicated by the same parts of the image as with hard exudates. For this reason, the pre-processing is identical to the previous algorithm. After adjusting its constants, very good results were achieved with soft exudates. The most significant difference between the two processes is in the size of the region used in Gaussian adaptive thresholding [74]. As the soft exudates are much larger, this area must also be larger. Subsequently, a pre-obtained background mask, optical disc and bloodstream mask is used for the result of the passing step. Different area sizes are also used in the subsequent reduction of suspicious areas. Table 3.3 shows the sizes of the areas used by the individual filters, Figure 3.14 shows the process for detecting soft exudates.

Table 3.3: Overview of filters used in the detection of soft exudates.

Image size	Below 2,000×2,000	Above 2,000×2,000
Gaussian filtration	23×23	23×23
Gaussian thresholding	201×201, $\sigma = -16$	201×201, $\sigma = -23$
Median filtration	19×19	19×19
Morphological opening	10×10	10×10
Morphological dilatation	7×7	7×7

Another way to refine and detail the results from a relatively large candidate area is to use morphological reconstruction [75]. The morphological reconstruction consists in the gradual dilation of the image in which the candidate area was marked. In this way, black spots are gradually filled with their immediate surroundings, i.e. a healthy retinal background. The exudates are then obtained by thresholding the absolute difference between the original and the reconstructed image. In these places, there is a big difference between the color of the exudate in the original image and the dilated image. The reconstruction procedure is shown in Figure 3.15.

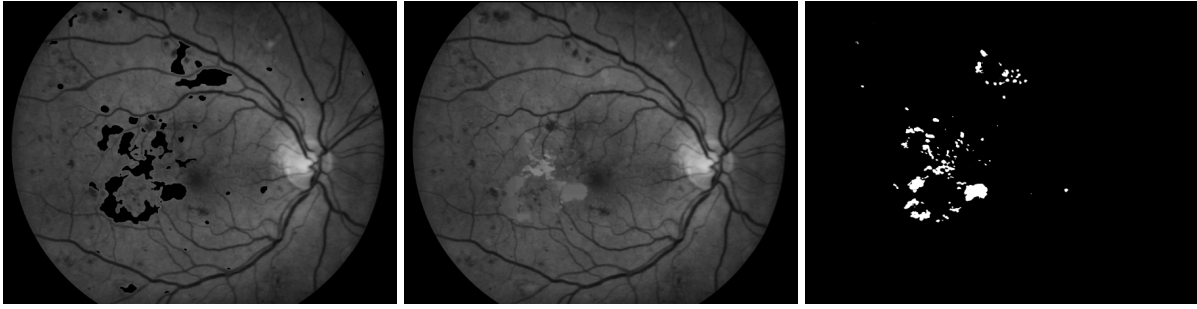


Figure 3.15: Candidate area (green channel) (left); reconstructed image (middle); difference between images (right).

Morphological reconstruction has relatively good results for the separation of exudates from the retina. Nevertheless, some margins are not very precise and include part of a healthy retina, or more exudates are joined together. Therefore, the found places are further modified. Contours are found in the candidate area and a point with maximum intensity is determined for each of them separately. By thresholding with a threshold value 70 times lower than the intensity of the found pixel, the exudate is separated from the surroundings. From the newly found contours in the thresholded image, the resulting candidate area of exudates is created, which has more precise boundaries. A comparison of exudate detection before and after treatment is shown in Figure 3.16. The last phase of processing is the evaluation of whether it is a finding or an incorrectly detected bright area of the retina. The following is the distinction of unwanted areas and exudates based on shape, shade, lightness, and their comparison with the immediate surroundings.

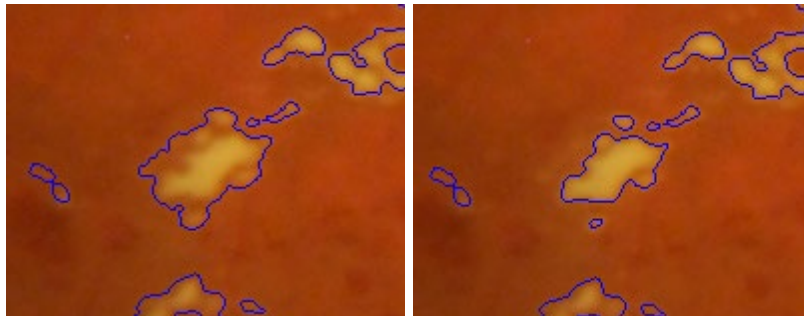


Figure 3.16: Comparison of exudate detection before (left) and after edge refinement (right).

To compare the color properties of the found areas, the original image was converted to an HSV color model, to which histogram equalization was applied by the CLAHE method [76]. The exudates have relatively sharp edges, and therefore the difference between the shade inside and outside the detected contour should be noticeable. To obtain the surroundings, the formation is dilated and the difference between the original and extended area is the nearest surroundings. For each finding, its average shade inside and outside the contour was evaluated. The experimentally determined values of exudates in the HSV color model are 18-50 for hue, 122-255 saturation and 75-255 value of brightness. The shape of the exudate was also evaluated using its circumscribed circle. If the formation is narrow and fills only a small part of the content of the circle, it is probably nerve fibers. Exudates, on the other hand, should fill most of the circumscribed area with their oval shape.

### 3.3.1.3 Contrast-based localization

The first candidate area is created based on the bright yellow color of the exudates. The areas of the retina that contain exudates are characterized by a high contrast between clear diseases and the background of the retina. The problem, however, could be found in the blood vessels, which are dark in the images in color compared to the background and also create a high contrast. Therefore, the first step is to remove them. A size 17 core closure is applied to the image. The size of the core should be greater than the maximum width of the vessels. In the closed image, a selection variance is calculated for each pixel. The resulting image  $E$  is obtained according to the formula:

$$E(x) = \frac{1}{N-1} \cdot \sum_{i \in W(x)} \left( E_1(i) - \mu_{E_1}(x) \right)^2 \quad (3.1)$$

where  $x$  denotes all pixels in the window  $W(x)$ ,  $N$  is the number of pixels in  $W(x)$ ,  $\mu_{E_1}(x)$  is the average value of  $E_1(x)$ . The window is set to  $7 \times 7$  pixels. The result can be seen in Figure 3.17. Otsu thresholding [77] is applied to the resulting image, and areas of the optical disc and the outline of the background mask are removed from the image. Since the candidate areas should not only be the outlines of the exudates, the last step is to fill the holes of the resulting contours.

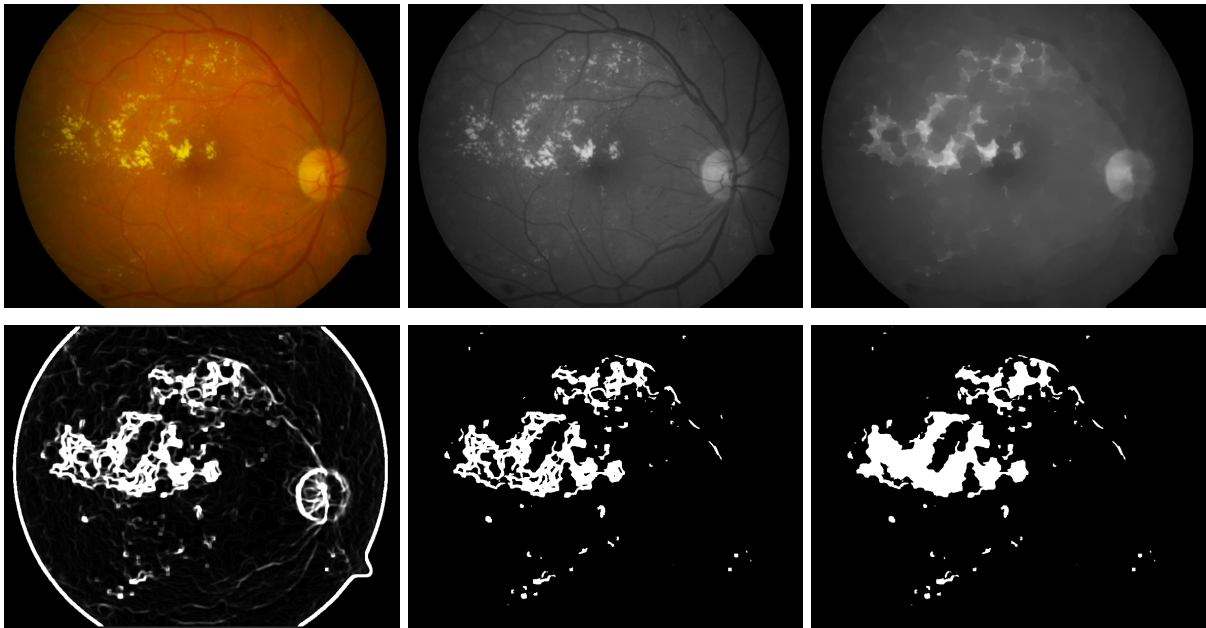


Figure 3.17: Segmentation of candidate areas based on intensity (from top left to bottom right): input image; green channel; closure; selective variance; Otsu and mask and optic disc removal; candidate areas.

### 3.3.1.4 Edge-based localization

When searching for second candidate areas, the *region-growing* algorithm [78] is used. The region-growing algorithm is applied to the green channel of the input image. The connectivity of the algorithm is set to 4 surrounding pixels and the threshold to 3. The algorithm gradually selects the pixels of the image for the seeds, which have not yet been included in any area. After selecting the seed  $p$ , its 4 surrounding pixels are checked. If the difference between their values is less than 3, the new pixel  $p_{new}$  is assigned to the area and becomes  $p$ . This process is repeated until all the pixels in the area have

neighbors with a value equal to and greater than 3 from their own value. Then, the average value of the pixels in the area is calculated. This value fills the area. We get an image with a uniform background color, from which sharply demarcated objects emerge (Figure 3.18).

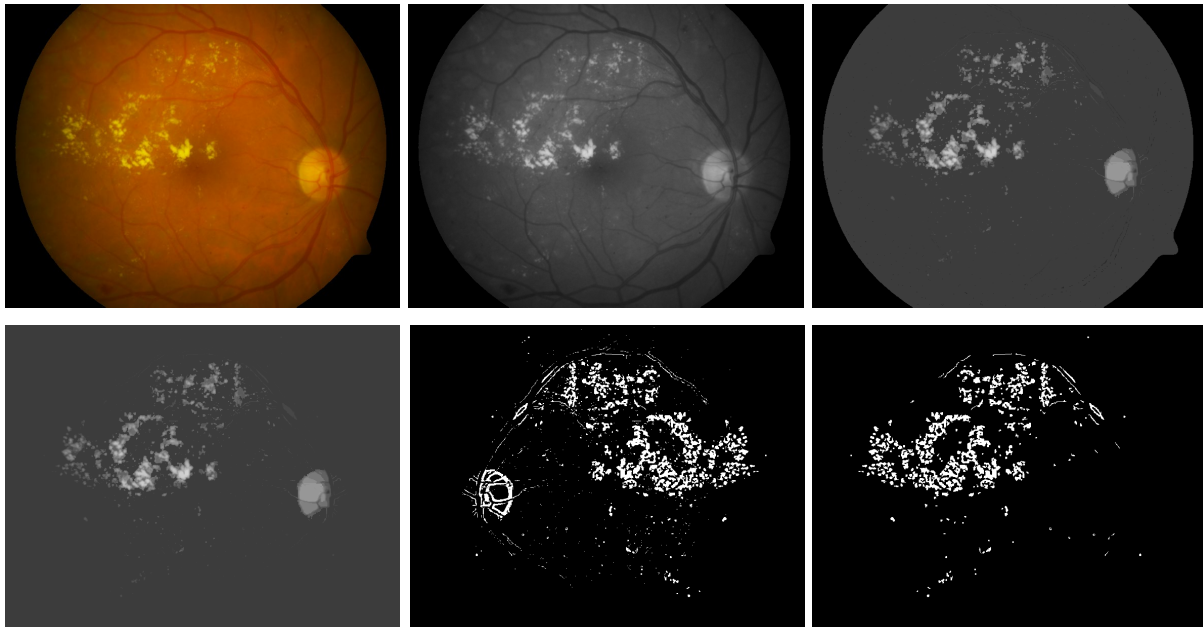


Figure 3.18: Segmentation of candidate areas by boundary (from top left to bottom right): input image; green channel; region growing algorithm; removal of dark areas; adaptive thresholding; candidate areas after noise removal and optic disc.

Because the exudates of interest have a lighter color from the background, all darker objects than the background are removed from the image. The value that appears most frequently in the image is selected as the background color. In the next step, adaptive thresholding is applied to the image. This gives a binary image, which, however, contains a small amount of noise, where the image was not smoothed before processing due to the region growing algorithm. Therefore, all contours that are less than three pixels are removed from the image. The last step is to remove the optic disc area.

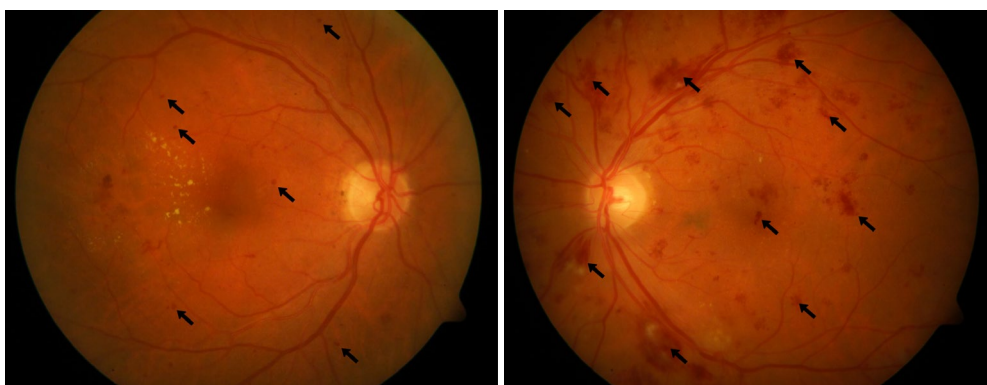


Figure 3.19: Microaneurysms (left); hemorrhages (right).

### 3.3.2 Microaneurysm and hemorrhage

Microaneurysm and hemorrhage are typical symptoms of diabetic retinopathy. Microaneurysm is small sac-like extensions of retinal capillaries. Hemorrhage is caused by rupture or overflow of microaneurysm, veins or capillaries. Their occurrence depends on the physiological factors of the patient

and his degree of disease. In Figure 3.19, we can observe the differences between microaneurysms and hemorrhages. With smaller hemorrhage, it is very difficult to distinguish whether it is a microaneurysm as a hemorrhage. Their characteristics are very similar, so we will look for them as one type of symptom.

### 3.3.2.1 Preprocessing

We extract again the green image channel. Then we apply Gaussian blur. As a result, too small areas merge with the background. If we omit this step, the region-growing algorithm would evaluate these small areas as separate areas, and this would rapidly slow down processing and adversely affect detection. Here, however, care must be taken to ensure that microaneurysm do not flow into the background. This is affected by the size of the Gaussian core. After experiments with core size, the best value of  $5 \times 5$  core size was obtained. Consequently, areas that are too bright, above the gray value of 50, are removed by thresholding. These areas are too bright for microaneurysm or hemorrhage, and removing them will speed up further processing. We do not set the threshold value exactly to the brightness limit of the findings. But we leave a sufficient reserve to create contours during the subsequent processing, according to which we detect microaneurysms or hemorrhages.



Figure 3.20: Hemorrhage (left); detection of suspected areas (center); and hemorrhage (right).

### 3.3.2.2 Suspicious areas and their evaluation

Suspicious areas are obtained using the region-growing algorithm as in exudates. Thanks to region growing, the retina is segmented into homogeneous areas. In this case, the parameter determining the range of pixel values that merge to form an area is set to 10. The maximum size of the findings was 77 pixels, which means that all larger areas can be removed. This also applies to the maximum color value of 45. Areas above this value are too bright to be found and can therefore be removed as well. To declare the suspicious area as a finding, we will use the fact that the real microaneurysms and hemorrhages form contour lines that darken towards their center. Figure 3.20 shows an example of creating contours.

### 3.3.2.3 Incorrect detection

The veins or capillaries have very similar properties to these findings and, in the procedure described in the previous section, also form contour lines. These contours are incorrectly classified as findings. We eliminate the problem by detecting the veins. However, it also has side effects. If there is hemorrhage close to a vein or capillary, it is incorrectly classified as a vein due to binary adaptive

thresholding. Here it is necessary to choose a compromise between the number of incorrectly marked veins as findings and the number of correctly detected findings even near the bloodstream. An example can be seen in Figure 3.21.

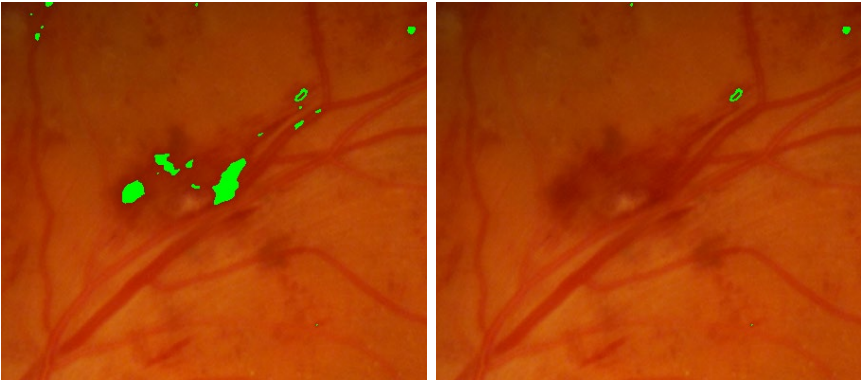


Figure 3.21: Area with hemorrhage - without (left) and with (right) vein detection.

Correction for vessels that would not be removed by a bloodstream mask may also be as follows. Large vessels tend to have a clear line at their center, which may be misclassified as a feature. Thus, the desired step is to remove these areas by morphological closure with a structural element smaller than the diameter of the vessels, and subsequent smoothing. The adjustment is shown in Figure 3.22.

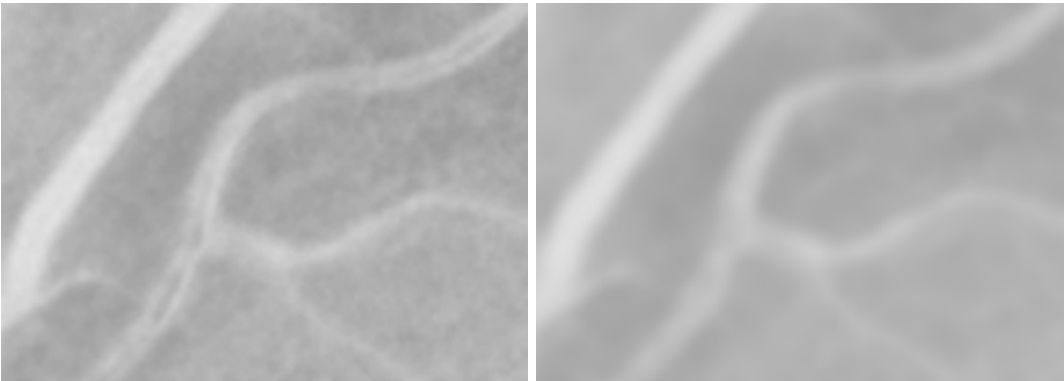


Figure 3.22: Smoothing the center of large vessels.

Incorrect detection of findings is also affected by the fovea, which also forms contour lines and is classified as a finding based on them. This will remove unwanted detection by detecting the fovea. Another factor adversely affecting detection is related to the patient's treatment. Not only

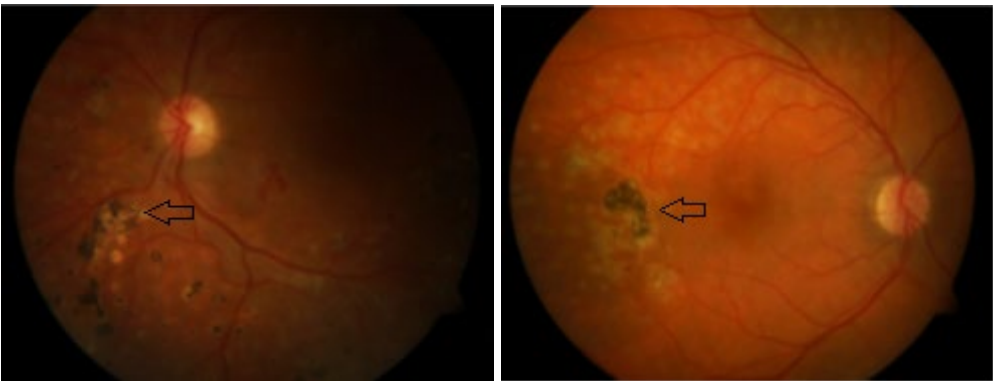


Figure 3.23: Photocoagulation scars.

photocoagulation points are formed during laser treatment but also photocoagulation scars can also form. These scars vary in size, are dark in color, see Figure 3.23. As with photocoagulation scars, this will not prevent us due to already active treatment.

#### 3.3.2.4 Bloodstream masks editing

Retinal images, whose bloodstream contrasts very well with the retina, cause the contours of these vessels to be included in suspicious areas. To prevent this, it is necessary to adjust bloodstream mask before it is used. Editing is a dilation of this mask in order to enlarge the blood vessels. The difference between the original and the dilated mask is shown in Figure 3.24.

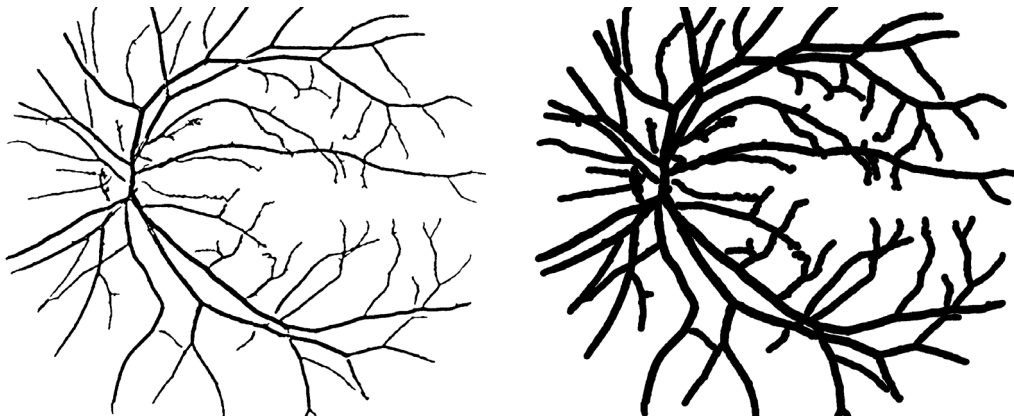


Figure 3.24: Original mask (left); mask after dilatation (right).

As soon as this mask is applied, unwanted contours are excluded from the image being processed. A comparison between suspicious areas using an untreated and modified mask can be seen in Figure 3.25.

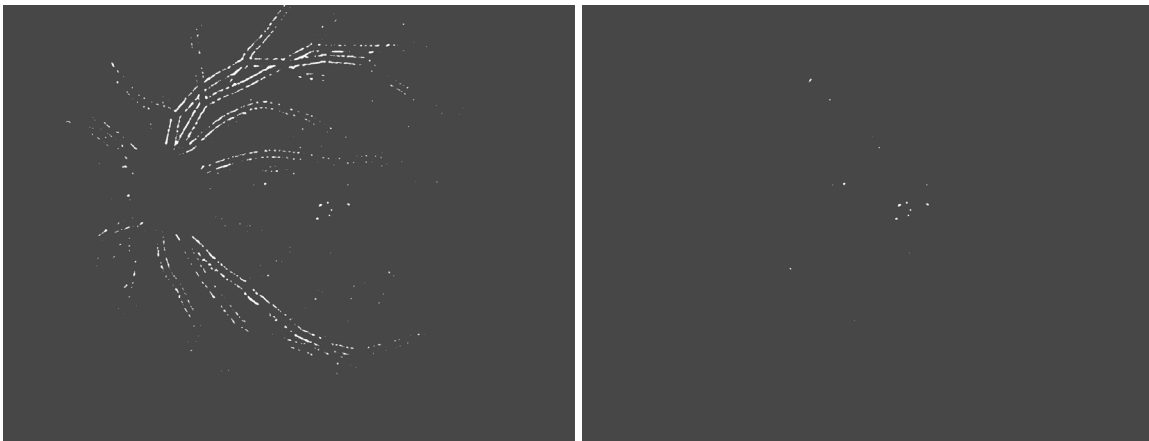


Figure 3.25: Suspicious areas with untreated (left) and modified (right) mask.

The final step is to determine which of the suspected areas are druses or exudates and which not. For this purpose, the HSV color model is used to which the input image is converted.

First, the contours of suspicious areas are determined to calculate their contents. If the content of a given area is greater than 3 pixels, the corresponding area in the HSV image is located. From this result, the average color tone, saturation, and brightness of this area can be calculated. Experimenting on the different images set out the limits summarized in Table 3.4. If one of the areas falls within one of these limits, it is a druse or exudate.

Table 3.4: Overview of HSVs for classification of suspicious areas.

Value	Limit 1	Limit 2	Limit 3
H	30–12	30–15	30–19
S	255–170	255–120	255–187
V	255–120	255–84	255–75

Once a region has been classified as a finding, its center of gravity is calculated using the mathematical moments, which represent the center from which a circle is created to indicate the finding. Labeling is first performed in a blank image, from which external contours are selected after checking all areas. These are plotted in the resulting image so that individual circles do not overlap the detected findings. The result of the detection can be seen in Figure 3.26.



Figure 3.26: Hard exudates detection result.

### 3.3.2.5 Specification of suspicious areas

Detection of droplets and exudates again works with the green channel of the default image (Figure 3.27 left). Normalized blur [80] with a mask of 7×7 pixels is used. This is due to the exclusion of small, unmarked areas that are sometimes difficult to classify by an experienced ophthalmologist. This Gaussian adaptive thresholding is then superimposed on this fuzzy image, which is very effective in defining suspicious areas. As mentioned above, the threshold for Gaussian adaptive thresholding is calculated individually for each pixel where this calculation is obtained by the weighted sum of adjacent pixels of a given pixel from which a certain constant is subtracted. In this case, the surrounding area is 5 pixels, and the reading constant is 0, so nothing is deducted. The result of this threshold can be seen in Figure 3.27 middle. Only now a mask can be applied containing areas of the bloodstream and optical disc that have already been detected earlier. If this mask was used at the beginning, it would adversely affect this threshold because it would create too much contrast in the image between the excluded areas and the rest of the retina. This would cause the contours of the blood vessels and the optical disc to be included in suspicious areas, which is undesirable. After the mask is applied, the image is then subjected

to a median smoothing with a 5×5 matrix size to remove the noise. The resulting suspicious areas are shown in Figure 3.27 right.

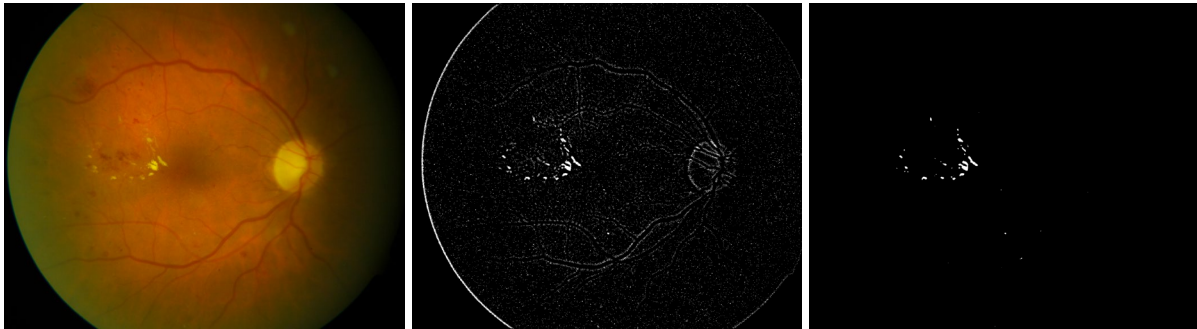


Figure 3.27: Original image (left); thresholding (middle); obtained suspicious areas (right).

### 3.3.2.6 CLAHE method detection

The candidate area is obtained by adaptive thresholding, which calculates the threshold from an area one-tenth of the diameter of the retina. A constant 9 is added to the average value obtained. Subsequent use of erosion [81] and opening [82] removes the slight noise generated by thresholding. The modified image contains hemorrhages along with larger vessels that need to be separated. Because the difference in color of hemorrhages and the retina itself is not as pronounced as in exudates, the refinement of the candidate area is based primarily on shape. A circumscribed circle is specified for the found contours, and those are selected that fill at least one-fifth of its area. This eliminates long, narrow pieces of blood vessels. A morphological opening is applied to larger oval contours, which removes vascular rests that may coincide with hemorrhages. At the same time, a rectangle is designed for small areas, which encloses them. If its aspect ratio is less than one third, it is a small piece of blood vessel and is excluded from the candidate area. A bloodstream mask is applied to selected structures, which removes the remaining parts of the vessels. The fovea area is also excluded, which in some cases is included in hemorrhage due to its dark color. The candidate area thus formed is extended by dilatation to include the margins of hemorrhages, and is used for morphological reconstruction, the principle of which has been described for the detection of exudates. Subsequent thresholding of the original and reconstructed image yields an area of hemorrhage to which an algorithm for refining the edges by thresholding is applied, similarly to exudates.

The last step is to classify the areas according to color and decide whether it is hemorrhage or part of the retina. The HLS (hue, saturation, lightness) color model with an equalized histogram using the CLAHE method has been selected for this task. For each shape, the average color shade of the inner contour part and its surroundings, is compared which was obtained by expansion. In the same way, the intensity of the green channel is compared, which should be lower in the areas of hemorrhages than in the areas of the retina. Experimentally, the areas corresponding to hemorrhages were found to have hue values in the range of 0-22, lightness values of 30-135, and saturation values of 120-255 in the HLS color model. Steps and result of the detection are shown in Figure 3.28.

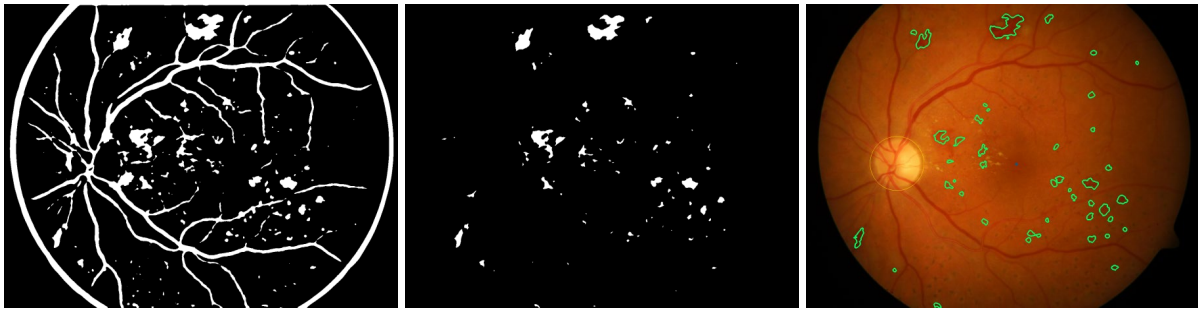


Figure 3.28: Adaptive thresholding (left); after application of bloodstream mask and fovea (middle); result (right).

## 3.4 Testing

The following section describes the testing of these algorithms. In most cases, the databases listed in Chapter 5.3 were used. Their overview is also listed in the Chapter 3.4.2. For implementation and testing there, were used mainly databases DB\_TIF and DIARETDB1.

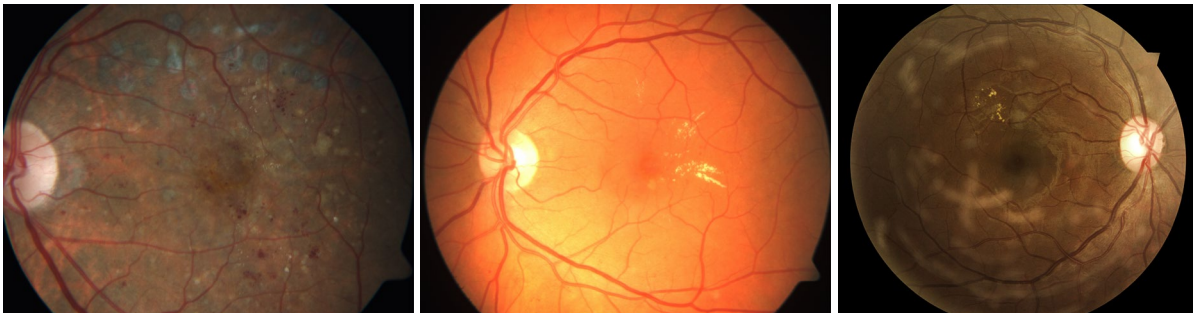


Figure 3.29: Examples of very different images used for testing: image of the retina after laser treatment (left), image with very high brightness (middle), image of the retina with unwanted light reflection (right).

### 3.4.1 Hard and soft exudates detection

There were used 70 images for testing, selected from the two previously mentioned databases. All selected images had a correctly detected optical disc and extracted bloodstream. These images were selected to test as many cases as possible during detection. This means that in addition to the images containing exudates, the selected photographs also received low light images, photos showing an artifact, healthy retinas, retinas with various other diseases, and also retinas after laser treatment. It was also necessary to test the detection results of photographs taken by various retinal imaging devices. These cameras have different shooting parameters that can significantly affect the quality of processing. Testing was largely part manual, as this method of checking the correctness of detection was faster than developing another test-only application. The control of the detection results took place during the whole development of the algorithm and was a necessary part of the development. After the completion of the algorithm, a large test was performed and a subsequent consultation with an experienced ophthalmologist. The feedback helped to reveal the shortcomings of the algorithm.

The main shortcomings in the detection of exudates were erroneous detection areas after previous laser treatment of the retina and the non-detection of larger exudates with unclear boundaries. The areas after the laser treatment turn yellow at the edges and have a very similar color to the exudates sought.

In the resulting test, each image was divided into smaller areas that were 100 pixels in size. Subsequently, for each image, it was determined in which of these areas the exudates were located. These areas were compared with the result of algorithm, which was also divided into equal parts. The result of this comparison is the number of percentages with which the algorithm detected exudates. The final detection results are shown in Table 3.5. The error rate of the algorithm is also very important in detection. These are these areas that the algorithm detected as exudates, but they are not really there. Table 3.6 shows the number of false detections and their ratio to correctly detected exudates.

Table 3.5: Results of exudate detection testing. Table expresses success of the algorithm detection against the actual results.

Database	Areas with exudates		
	Total number	Correctly detected	
TIF	1,315	1,186	90.19%
DIARETDB1	556	499	89.75%
Sum	1,871	1,685	90.06%

Table 3.6: The table shows the number of incorrectly marked exudates in relation to correctly marked exudates.

Database	Badly detected exudates	
	Number	% from correctly detected
TIF	37	3.12
DIARETDB1	11	2.20
Sum	48	2.85

### 3.4.2 Microaneurysm and hemorrhage detection

The algorithm in Chapter 3.3.2 have been primarily designed to detect findings in DIARET databases, but we also use images from the HRFIDB, DRIVE, and 4 pictures from the bottom of a camera located in the biometric laboratory at the Faculty of Information Technology, Brno University of Technology, to test the robustness. These databases differ in image quality, which greatly affects the accuracy of detection. Table 3.7 shows their basic characteristics. In the initial testing of other databases, the algorithm seemed entirely unusable. After analyzing the problem of incorrect detection, the parameters were modified and the algorithm achieved better results.

To evaluate the success of detecting the background mask, optic disc, and fovea, an ophthalmologist is not required. These parts of the retina may also be determined by a layman after initial training on the basic anatomy of the retina. However, to evaluate the accuracy of detection, it is necessary to compare

these results with the actual results, where a manual physician, optimally an ophthalmologist, performed detection. These findings are relatively difficult to identify and detection requires practice.

Table 3.7: Database characteristics.

Database	Number of images	Format	Size	Camera	FOV
DIARETDB 0	89	PNG	1,500×1,152	-	50°
DIARETDB 1	130	PNG	1,500×1,152	-	50°
HRFIDB	16	JPG	3,504×2,336	Canon CR-1	45°
DRIVE	20	TIF	565×584	Canon CR5	45°
BUT retinal database	4	PNG	3,888×2,592	Canon CR-1	-

Evaluating images is also time consuming. Determination of the findings was carried out manually on the basis of a test program in the presence of a student at the Faculty of Medicine at the Masaryk University in Brno. In addition, the DIARETDB0 and DIARETDB1 databases are attached to *diaretdb0\_groundtruths* and *diaretdb1\_groundtruths*, where there is information about what symptoms are found in the image (red small dots, hemorrhages, hard exudates, soft exudates, neovascularization). In order to detect microaneurysms, hemorrhages, exudates, and druses, a test program has been developed to speed up and automatically evaluate this process. The test program will display two windows to the user. The first window will display an original image overlapped by the matrix with the 30x30 pixels cells. This matrix contains automatically marked cells with detected diseases. On this matrix, there is possible to click to cell to change of mark as finds. In the second window there is an original image from the database – see Figure 3.30.

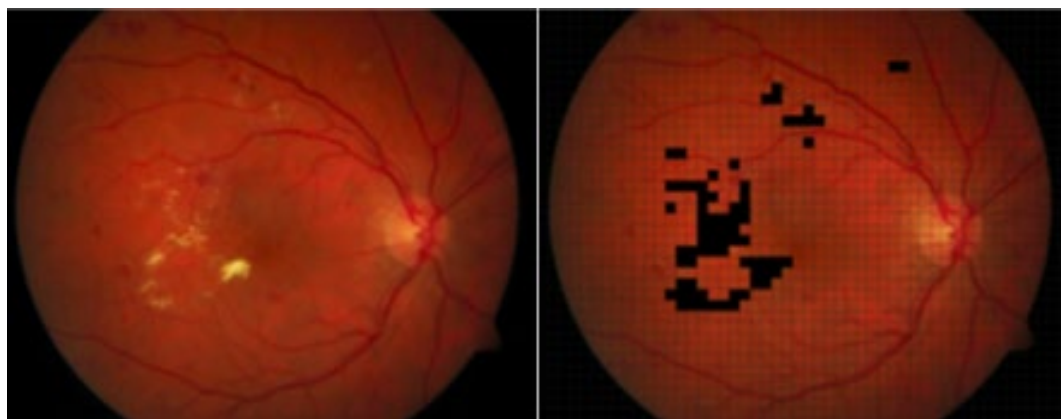


Figure 3.30: Making ground truths by marking of disease manifestation.

### 3.4.3 Additional test algorithms

The output from the test program provides four types of data: true positive, false positive, true negative, false negative. We obtain these values by comparing ground truth and automatically evaluated areas for each image. For the testing of biometrics system success are used terms from category of sensitivity and specificity. The resulting values are averaged from all images in order to determine overall sensitivity and specificity. Sensitivity for us in this case represents the percentage of the actually

affected parts of the retina classified by automatic detection as affected. The true positive rate (TPR) refers to the probability of a positive test, conditioned on truly being positive and is obtained using the equation:

$$TPR = \frac{TP}{TP+FN} \quad (3.2)$$

Specificity, or true negative rate (TNR) refers to the probability of a negative test, conditioned on truly being negative. In our case, means the percentage of healthy parts classified by automatic detection as a healthy retina. We will calculate it according to this relationship:

$$TNR = \frac{TN}{TN+FP} \quad (3.3)$$

As we can see in Table 3.8, the optic disc was misidentified in 8 cases. Incorrect optic disc detection is caused by poor image quality; these images contain shadows or light reflections from the bottom of the camera. In one case, incorrect detection is caused by error in image, which has the same size and intensity as the optic disc.

Table 3.8: Optic disc detection.

Database	True positive	False positive	Success rate [%]
DIARETDB0	85	4	95.29
DIARETDB1	126	4	96.82

The following tables show the results of individual flaw detection tests. See Table 3.9 and Table 3.10:

Table 3.9: Results of DIARETDB0 and DIARETDB1.

	Sensitivity [%]		Specificity [%]		Success rate [%]	
	Dia0	Dia1	Dia0	Dia1	Dia0	Dia1
<b>Exudates and druses</b>	94.26	90.28	99.41	99.32	99.65	99.65
<b>Microaneurysms and hemorrhages</b>	92.66	91.46	99.24	99.35	99.24	99.42

To test the possibility of using the algorithm for other fundus cameras, we use images from the HRFIDB [27] and drive [43] databases, along with 4 images from the BUT retinal database. In the first test, the algorithm over these databases showed zero usability. This result causes a various image quality. Table 3.10 shows the success of optic disc detection. The best results were obtained over the HRFIDB database and on the pictures from the BUT database. These pictures are of good quality and do not contain significant disease manifestations.

Table 3.10: Results of optic disc detection in databases.

Database	True positive	False positive	Success rate [%]
HRFIDB	16	0	100.00
DRIVE	19	1	94.73
BUT retinal database	4	0	100.00

Table 3.11 shows the success of detecting findings: exudates, druses, micro-aneurysms, hemorrhages.

*Table 3.11: Results of databases HRFIDB, DRIVE and BUT retinal database.*

	Sensitivity [%]			Specificity [%]			Success rate [%]		
	HRF	Drive	BUT	HRF	Drive	BUT	HRF	Drive	BUT
<b>Exudates and druses</b>	69.81	63.63	N/A	98.76	99.70	99.93	98.36	99.70	99.93
<b>Microaneurysms and hemorrhages</b>	18.30	N/A	N/A	99.87	98.63	99.97	99.51	98.53	99.95

## 4 Synthetic retinas

The idea of this algorithm was to create a basic image generator for synthetic retinas. The generated images should be as close as possible to real images. The main motivation for creating an application is that obtaining a larger database of real retinal images is relatively difficult. People are not willing get acquired a picture of the eye retina. One of the reasons may be the possibility of finding out a person's health. To collect retinal images from subjects, you need the appropriate equipment (minimally digital ophthalmoscope or even better a fundus camera) and you need to find the volunteers who will be willing to let their retinas are acquired. The best way, comparably with fingerprint areas in biometric systems (synthetic image generators SFinGe, Anguli, and SyFDaS), is to use a generator of synthetic images.

Using a program that would generate artificial images of the retina, it would be possible to create an arbitrarily large database of retinal images. Such an extensive database is very useful in the development of various algorithms working with retinal images for their testing, or for training using machine learning. Especially with the occurrence of COVID-19, the possibilities of creating basic databases have decreased significantly, since people need to be in close contact with the doctor taking the picture.

Therefore, testing was performed by comparing results from real and synthetic retinas. For testing the reality of application results there were used, two other applications. The first one searches for crossings and bifurcation images and combines and displays the other results from all retinas.

### 4.1 Synthetic retinal images generator

We are able to generate a synthetic retinal image, including the optic disc, macula, and vascular patterns with randomly generated or predefined features (crossings and bifurcations). Now we are working on the additional features that will decrease the quality of such images, e.g. reflections, diseases etc. We are also working on supplementing that with something that will generate diseases and damage on the image of retina, so we can create a unique database for deep learning. It is possible to generate any large-scale database, where you can predefine (in a configuration file) the setting, i.e. how many images with which background, distortions, and features should be generated. Therefore, this part is very important for biometric systems, because with this way the training and testing of algorithms for biometric retinal recognition could be done on large-scale databases. It is important that the quality of the images correspond to the real images, i.e. some work is still ahead of us.

First, a basic idea of how the generator will work and how its main parts are identified is described. Furthermore, the designs of the individual parts of the generator are described in greater detail and are intended to create partial sections of the resulting image. The aim is to design the generator so that it generates images as close as possible to real images of the retina. Real images often have a very different

look in terms of color distribution or detail. One of the test options, where we checked the reality of created images is using the bifurcation and crossing searching described in Chapter 5.2.

The generator is able to create the desired number of randomly generated synthetic retinal images at the selected resolution and the selected general properties, such as the image angle or the zoom rate according to the specified parameters.

The generator can then generate a large number of images of the retina, where it is possible to train and test various algorithms. If we add a disease creation module to the generator, we can also test algorithms for future work.

### 4.1.1 Vascular bed layer

The retinal vasculature of the retina consists of the arterial and venous channels. Both of these beds can be divided into upper and lower branches, which are further divided into nasal and temporal branches.

When generating the texture of this layer, the generator uses pre-generated branching positions for the arterial and vein branches. The method for generating these positions is described in Chapter 4.1.4. Generally, the generator first creates separate textures of the arterial and venous channels, which then merge into one final texture (see Figure 4.1). This division is necessary due to the way the vascular bed is rendered. It counts that blood vessels do not cross each other.

Partial textures are merged so that when the artery and vein are in the same position, a new value of the color and transparency of the texture is calculated at that position. In this calculation, both original colors are used with respect to transparency, with the unified textured vein being drawn above the artery. If only the artery or vein is at the given position, it will be redrawn into the resulting texture unchanged. If there is no vessel in the position, this position remains transparent on the resulting texture.

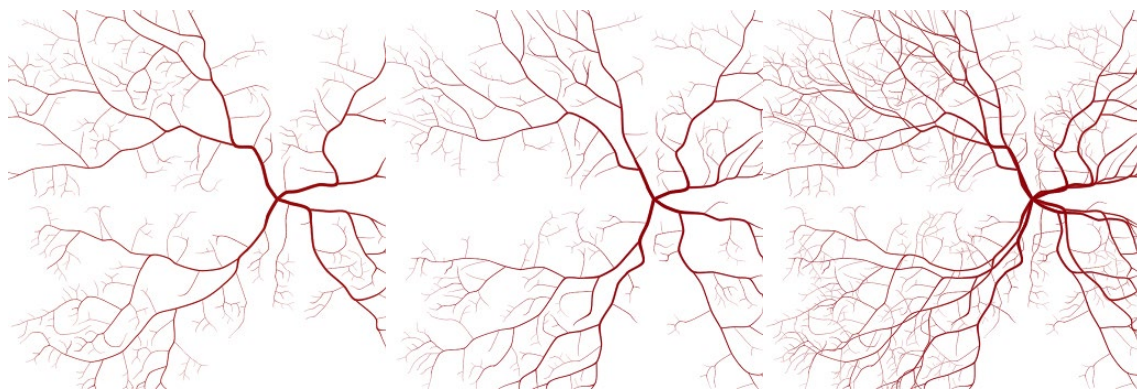


Figure 4.1: Arterial fluid texture (left); vein texture (middle); resulting vascular fluid texture (right).

Partial textures then arise through the gradual plotting of the individual branches of the arterial or venous passages. In order to a natural resulting vessel shape, it is necessary that the connectors between the individual branches take the form of a curve without significant sharp breaks at the branching points. Because the curve is the link between the sequences of points, it cannot be divided into several parts at

one point. Therefore, the branched tree of the given branch is plotted sequentially, as shown in Figure 4.2. A description of this plotting is given in Chapter 4.1.4.

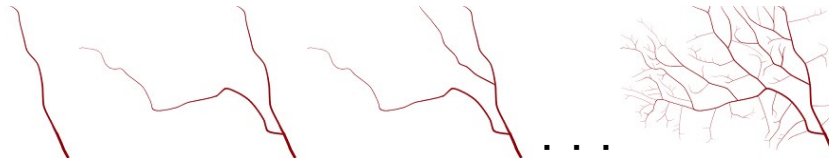


Figure 4.2: Gradual rendering of the upper temporal branch.

Gradual rendering takes place by gradually forming a curve from the initial point of the branch of the vascular stream, which passes through the next branches, where it continues with a wider vessel at someone of the end points of the vascular bed. As soon as the vessel is drawn from the beginning to the end, a new starting point is chosen as one of the already drawn branch points, in which the beginning has the widest still unrefined vessel. The vessel with this starting point will be drawn in the same way as the first vessel. This procedure is repeated until all the blood vessels of the branch are drawn. The cubic Bézier curve [83] is used to plot the vessel. It uses two control points for every two points it goes through.

Figure 4.3 shows a curve along with the parameters needed to create it. The curve begins at the start point  $A$ , continues through the branch point  $B$  and ends at the end point  $C$ . The curve is made up of two partial control polygons that make up points  $(A, c_{A2}, c_{B1}, B)$  and  $(B, c_{B2}, c_{C1}, C)$ . Control points of the control polygon are at one quarter of the length of the polygon between the start and end points of the control polygon that are multiplied by  $rand(0.8, 1.2)$  for each control point.

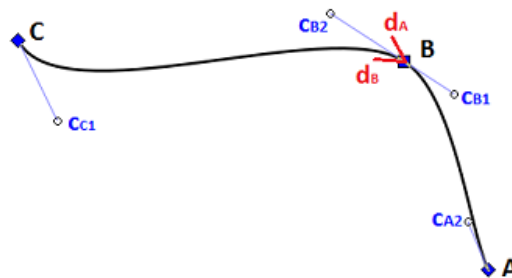


Figure 4.3: Cubic Bezier curve and its parameters.

To determine the position of the control point, apart from the distance from the point to which it belongs to, is necessary to calculate an angle indicating the direction from which the point comes. At the starting point of the curve, this angle is equal to the direction in which the next branch point lies through which the curve passes. At the endpoint of the curve, this angle is calculated by adding a deviation of size of  $60-90^\circ$  to the direction in which the previous branch point is located.

The inner points of the curve are 2 control points. The direction of the second control point is calculated as the midpoint between two angles, indicating the direction from the previous point to the current point and from the current point to the next. The direction of the first control point is exactly opposite (rotated by  $180^\circ$ ). This calculation is graphically depicted for points of control  $c_{B1}$  and  $c_{B2}$  in Figure 4.3 for point  $B$ , where  $d_A$  and  $d_B$  indicate the directional angles used in the calculation.

The vessel is plotted sequentially from the starting point to the end point following the pair of branching points running consecutively. For each point's pair and the relevant control points that affect the shape of the curve between them, the partial points of the curve are then calculated.

The step size  $k$  in calculating the Bézier curve points is determined with respect to the distance  $d$  between the start and end points of the curve by the relationship

$$k = \frac{1}{2d} \quad (4.1)$$

Calculated Bézier curve points are then linked by lines whose points are calculated using the Bresenham algorithm [84]. A texture of the blood vessel is drawn around this curve, consisting of partial segments. For each point of the curve, a semicircle is drawn in the direction of the line below which the point belongs to. The Bresenham algorithm is also used to draw this semicircle, with the radius of the circle (line length) equal to half the width of the vessel at that point. In this rendering process, all points belonging to the texture of the vessel are rendered, but for one point, its color is calculated several times with different parameters. The resulting color is selected as the color whose individual components have the highest value. The lightest and least transparent color corresponds to the smallest distance from the center of the vessel.

This method of selecting the resulting point color is the reason why arteries and veins have to be plotted separately and then combined into one texture in another way. However, it is used when plotting a new vessel to connect this vessel to the already drawn vessel at the branch point - see Figure 4.4.



Figure 4.4: Connecting the new vessel to the already depicted vessel at the branch point.

The basic RGB color of the texture is in the artery (160, 15, 15) and in the vein (150, 5, 15). The individual color components are adjusted for each frame by multiplying by *rand* (0.99, 1.01).

### 4.1.2 Layers

When looking at the real images of retinas, it is possible to easily identify four different parts of the image that can be generated separately and then be combined into a final image. These sub-parts are represented as image layers in the generator, where the lowermost layer contains the background texture of the retina. Here the layer containing the texture of the optic nerve target overlaps. Both of these layers are covered by another layer containing the texture of the vascular bed. All layers then overlay the textured frame layer. Figure 4.5 shows the plot of the individual layers in the given order.

The layer has the shape of a square surface on which the texture is applied. The dimension size of this area is equal to the shorter side of the rendering window, which is multiplied by two scaling parameters. The center of the layer is aligned to the center of the rendering window, with only the parts of the generated text within the rendering window being included in the resulting image. Because of the layer

size and texture variable applied to it, the generator uses a custom coordinate system to create textures, where it then maps the individual pixels of the texture.

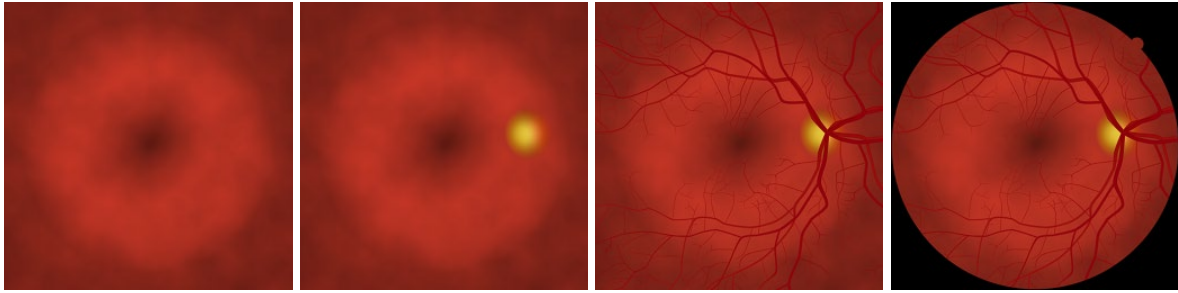


Figure 4.5: A gradual render of layers: Background layer (left); adding a layer of the optic nerve target (left middle); adding a vascular bed layer (right middle); adding a layer of frame (right).

Scaling, shifting, and rotating the layer and the texture are designed to be independent of texture generation. While scaling modifies the layer size and does not manipulate the coordinate system, rotation and displacement do not change the position of the layer but are applied to the coordinate system.

As can be seen in the real frames shown in the earlier sections of this work, the images of the retina do not always occupy the whole area of the image, or sometimes they are partially cut off. Therefore, we resize the layer so that the size of the rendering window does not change, as well as the resolution of the resulting image.

As with the first case, but this time without changing the frame texture layer size, it is possible to choose how much of the retina is presented in the image, so be sure to choose the pixel size of the fundus camera that would capture such a frame. Different settings for this parameter are shown in Figure 4.6.

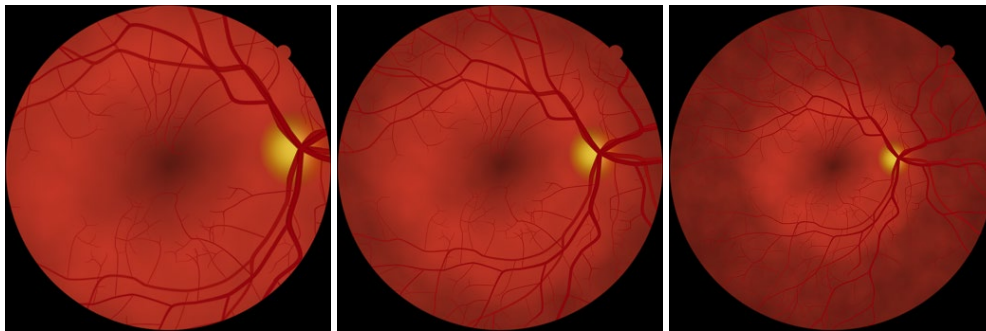


Figure 4.6: Different sizes of the retrieved part of the retina: maximal zoom (left); central zoom (middle); no zoom (right).

Real-motion capture is not always ideal. The image is more or less rotated and possibly slightly shifted. The displacement may also be deliberate if another part of the retina is being captured. For this reason, these transformations also allow the proposed generator. Both transformations are applied to the coordinate system, not to the layer itself. First, a shift is made followed by rotation. For each layer, it is possible to set the own rotation and displacement size with both layers transforming over layers. Thus, when the background is rotated and shifted, the target of the optic nerve and the vascular bed is shifted. Further transformation at the optic nerve target layer can then change its position relative to the background. Likewise, the position of the vascular bed can be changed to the lower two layers. Since

these transformations are intended to simulate a different eye position when capturing the retina, they are not applied to the frame layer.

### 4.1.3 Background layers

The retina background is mostly reddish; the fovea and ex-macular periphery is darker. The area between the fovea and the border of the macular area is then lighter. In a more detailed view, smaller objects of different colors and intensities are visible throughout the area, creating a dense vascular network of the cavity. The generated background texture is opaque to basic RGB color (200, 60, 40). Figure 4.7 shows the resulting background texture.

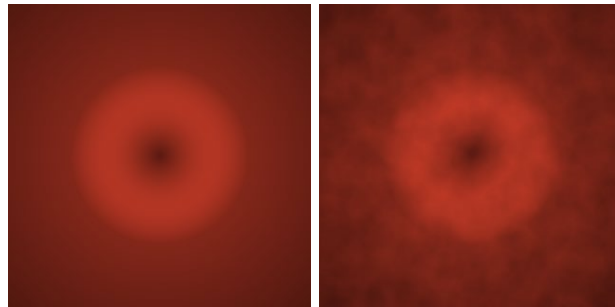


Figure 4.7: The resulting background texture without a noise function (left); with a noise function (right).

This function describes the randomness of the background texture and is generated by the shadowing choroid. It uses Perlin noise [85], which has 3 octaves, frequency and amplitude set to 1, and returning values from interval  $<-1;1>$ . Perlin noise is also initialized by a random number, making it different for each frame.

Graphically, the function is depicted in Figure 4.8 where the dark areas indicate the positive values of the noise and the light areas of the negative values. When the dark area is getting lighter, the closer value of the function is set to 1 and when the light area is getting lighter, the function's value is closer to -1. At the transition of dark and light areas, the function has a value of 0.

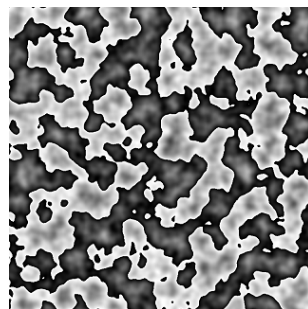


Figure 4.8: Noise function.

The texture of the optic disc (OD) target is largely transparent except the ellipse-shaped area that contains the texture of the OD target itself. When generating a texture inside this ellipse, the base color of the RGB value is again returned (250, 250, 150). Each folder is multiplied by the function  $rand(0.98, 1.02)$ , as well as background textures to ensure the variability of the base color for different images.

Figure 4.9 shows the resultant texture of the optic disc target (cut from the overall layer texture) together with the individual color components from which it was composed. However, the color of the texture still changes in the final rendering, and because of its partial transparency, its color also affects the color of the background texture beneath it.

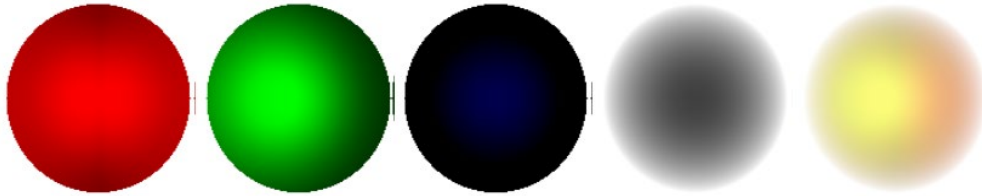


Figure 4.9: The texture of the optic nerve target and its parts: red texture color component (left); green (left middle); blue (middle); texture transparency (right middle); resulting texture (right).

For each image, the final position of the optic disc is slightly different due to accidental slight rotation and displacement. When the left-eye image is generated, the rotation is 180°.

#### 4.1.4 Generating a vascular bed

Before drawing a vascular bed, it is first necessary to generate the branch positions of the blood vessels and properties of these points needed for plotting. These points are generated separately for each of the major branches of the artery and vein. Branching points are generated for all branches by the same algorithm with different values of some parameters. Their generation is divided into two parts. First, a tree of branch points is generated, and then the positions of individual points are gradually calculated with respect to the already calculated positions of the other points in the tree.

Each branch point has several properties that need to be generated:

- **Point position** (counted later)
- **Distance from previous point** – length of line between these two points
- **Vessel width** – value from interval  $\langle 0;1 \rangle$ , where 1 has a vessel at the starting point of a given branch, and a value of 0 has the endpoints of a given branch
- **Point type**
  - Y-branching – the vessel is divided into two approximately equally wide vessels
  - T-branching – the vessel is divided into a wide and narrow vessel
  - no branching – the vessel is not split, just passing through the point
  - end of vessel
- **Type of vessel** (see Figure 4.10)
  - left and right strong blood vessels (blue)
  - left/right wider weak blood vessel emerging from the left/right strong blood vessel (green)
  - other blood vessels (red)

The root of the branch tree is the point located at the center of the optic nerve target. It creates one of the following branching points, and then generates the tree recursively so that each new branching point generates the following two branch points. Generation ends when the vessel's width at the newly created point is  $\leq 0$ . The properties of the following branch points are also calculated, and the design of the method of calculating some of them was based on the information published in [34].

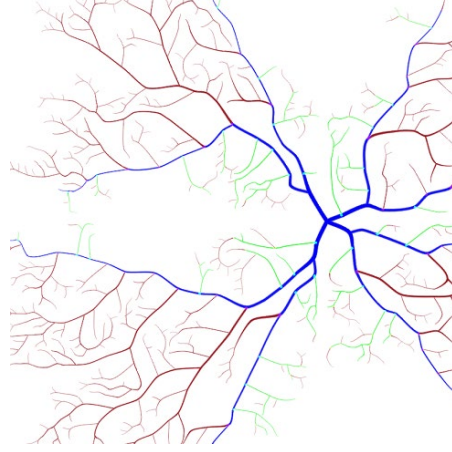


Figure 4.10: Color illustration of different types of vessels.

The distance from the previous point  $d$  is calculated for the following two points according to the vessel width  $w_a$  at the current point as follows:

$$d = \begin{cases} \text{rand}(0.15,0.05) & \text{for } w_a > 0.15 \\ \text{rand}(0.05,0.02) & \text{else} \end{cases} \quad (4.1)$$

This has the consequence of the narrow blood vessels having more branches.

First, depending on the type of branch of the current point, the ratio is calculated to which the right and left successor are divided. If it is the current point Y-branch, the ratio of right and left successors is calculated as  $r$ :  $(1 - r)$ , where  $r = \text{rand}(0.45, 0.55)$ . In case of T-branching, it is 50% probability  $r = \text{rand}(0.95, 0.99)$ , otherwise  $r = \text{rand}(0.01, 0.05)$ .

If the current point is a part of the leftmost or rightmost strong blood vessel, this probability is altered in the T-branch, such that the weaker T-branch branches are generated towards the boundary of the quadrant. In the beginning, there is a 70% probability that the weaker vessel is generated towards the boundary of the quadrant. If this happens, this probability will decrease by 10% for the type of vessel (left –  $w_l$  or right –  $w_r$ ); if not, the probability will increase by 10%.

The value of the vessel's width is then calculated for both of the following branch points using their distance from the actual point, the vessel width at the current point, and the division ratio as follows:

$$w_r = (w_a \times \sqrt{r}) - \left(w_a \times \frac{d_r}{10}\right) - \frac{d_r}{20} \quad (4.2)$$

$$w_l = (w_a \times \sqrt{1-r}) - \left(w_a \times \frac{d_l}{10}\right) - \frac{d_l}{20} \quad (4.3)$$

Parameter  $d$  is different for left ( $d_l$ ) and right ( $d_r$ ) type of vessel. If the width of the calculated vessel at the next point is not positive, this point is marked as the vessel endpoint. If the calculated width is negative, the distance of that point from the previous point is adjusted to the width of the vessel, which at that point is equal to zero.

In other cases, it is decided whether the following point will be a Y-branch or a T-branch. One of the auxiliary features of a point is the probability of selecting the Y-Branch for its following branching points, that is, at the starting point, set to 20%. If the selected branch type of the next branch is the Y-branch, then this probability is set to 0% at this next point. If the T-branch is selected and the next

point is the weaker T-branch of the current point, the probability for this next point is set to 40%. Otherwise, the probability is increased by 25%.

First, the position of the leftmost and rightmost points of thick blood vessels (type 1) is calculated, then it points the position of the left/right wider weak blood vessels resulting from vascular type 1 (type 2) and finally position of the other vessel (type 3). Within these types of vessels, the order of points in the calculation of the positions is given by the width of the vessel at a given point, with the positions of the wider vessels being counted first. Point positions are counted in this order because not all tree branch points generated will eventually be used.

When calculating the position of a particular branch point, the set of positions on which this point may be located is first determined. From the beginning, these are the positions around the previous branch point at the distance that this particular point has generated as a property. Then, depending on the direction of the vessel at the previous point, this set is limited by the interval of angles in which the position of the point may be. For each of the remaining positions, the weight of the position is calculated based on the deviation from the center of the interval.

On the real images, the observed part of the retina is circular and the rest of square image is black. A majority of the right-hand portion of the image tends to see a smaller part of the retina in the shape of a semicircle or rectangle. Accordingly, is it possible to find out, if is the image rotated.

The generator allows you to choose which quadrant the mark will be in, and also whether the mark will have the shape of a semicircle or rectangle. The generated texture has a black color and, depending on the coordinates, only the transparency of the texture changes.

#### 4.1.5 Image result

The program gradually generates and combines all the above layers into one image. For the credibility of the image, it covers the image with a notched frame, of which shape can be adjusted too. The resulting application is run from the command line with individual parameters, as described in the corresponding work of our research group [125]. An example of the generated images is shown in Figure 4.11. Testing of these results is described in Chapter 5.8.

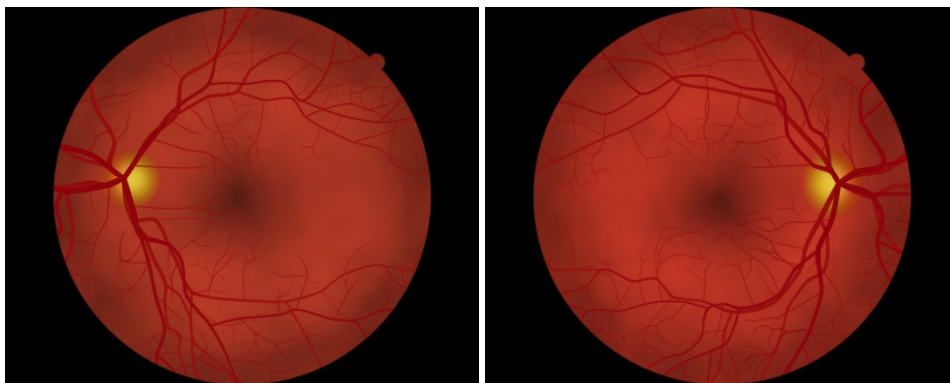


Figure 4.11: Example of the resulting images of generated synthetic retinas.

## 4.2 Algorithm improvements

This chapter work with existing bloodstream images. These were obtained from the *Messidor* database [26]. The data were selected completely randomly, the factor of the same image location is suppressed by the *Messidor* project by its definition (see 5.3). The properties of branching of the main vessels are observed in the images. Individual features are measured, statistically processed and subsequently evaluated. The recording of point positions for regression programs was performed in the web program *Desmos*, which also subsequently presents approximation curves. The measured data are processed by mathematical software for creating nonlinear regressions. Two mathematical programs *CurveExpert Basic* [87] and *RegressionTools* [88] are used to increase the number of solution models. *CurveExpert Basic* is an easy-to-use GUI application that allows to quickly and easily calculate linear and nonlinear curve approximations using built-in approximation models. The tool allows to define own models. The application uses its own metrics to determine the best curve to show the user's most suitable models for the points. The calculated approximations can also be displayed in graphs and visually compared with each other [87]. The *RegressionTools* web tool calculates both linear and nonlinear regressions using a set of primitive functions. This set contains over 100 functions. Depending on the number of entry points, the program composes primitive functions and creates a more complex model from them [88]. The *Desmos* application exists as a web version. This GUI provides a canvas with a coordinate system for points and mathematical curves. A key feature for selecting this software is the ability to insert an image into the desktop. Each created object creates its own layer. These layers can be overlapped. This feature allows drawing curves and inserting points over an embedded image [86].

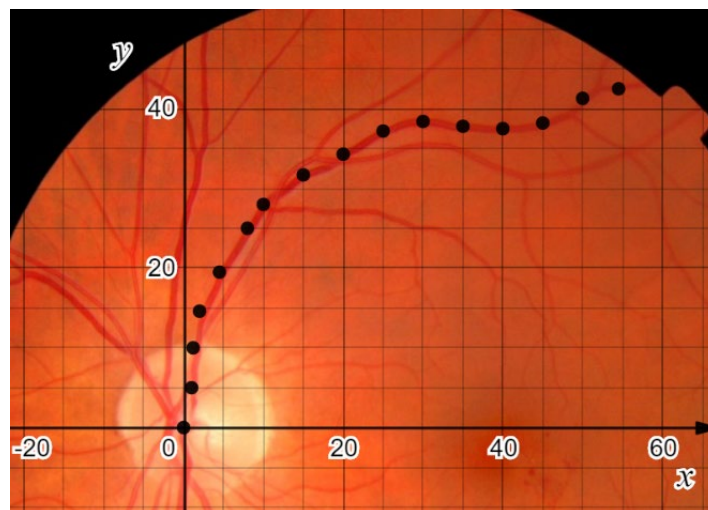


Figure 4.12: Image from the *Messidor* database in the *Desmos* application and interspersed with points.

### 4.2.1 Retinal vessel shapes identification in macular and nasal bloodstream

Due to the time-consuming processing of individual images, only 80 vessels were processed. For data processing was used the *Desmos* application. The inserted image was enlarged to  $170 \times 20$  internal program units. Subsequently, it was shifted so that the point of the coordinate system  $[0; 0]$  have

the same position as the entry of the vessel into the retina in the blind spot. A group of points that overlap the vessel in specific places records the course of a vessel. The distance between the individual points of the group is around five units. The initial placement of the image in the environment, enlargement, displacement and interposition of the vessel are shown in Figure 4.12.

The choice of the image size at  $170 \times 120$  units determines the definition range of the functions as well as their range of values. This coefficient corresponds to almost ten times of the image when it is inserted. The reason for enlarging all images is better work with regressive models. Selected programs work better with the interval  $\langle 0; 170 \rangle$  than with the original values, which were from the interval  $\langle 0; 17 \rangle$ . By processing all randomly selected images, the assumption was made that the behavior of macular vessels could be expressed by a mathematical function. This assumption will be verified in the section 4.2.1.1. The obtained results further create the assumption that the lower macular vessels are identical in shape with the upper macular vessels. This property of blood vessels is also verified by same section.

#### 4.2.1.1 Approximation of detected macular vessel shapes by nonlinear models

In the first part, the data were divided into upper and lower macular (temporal) vessels. These two data sets were passed to the regression programs (*CurveExpert*, *RegressionTools*) to calculate approximation functions. The programs created a list of mathematical functions, which they sorted according to internal metrics. The best-rated models were selected, which further fulfilled the natural development beyond the last point. The obtained functions represent only one lower and one upper specific vessel, so it was necessary for one preselected parameter of the function to take on an interval of values. These intervals were determined empirically to cover at least 90% of the measured points in the data set. Selected parameters are specified in Table 4.3.

$$f(x) = \frac{a+bx}{1+cx+dx^2} \quad (4.4)$$

$$f(x) = ae^{-e^{b-cx}} \quad (4.5)$$

$$f(x) = \frac{a}{1+be^{-cx}} \quad (4.6)$$

$$f(x) = \pm a\sqrt{x} \quad (4.7)$$

Table 4.1: Calculated parameter values for the polynomial equation (4.4).

Parameter	Parameter value upper blood vessels	Parameter value lower blood vessels
<i>a</i>	4.418165	-6.832217
<i>b</i>	2.839498	-2.704067
<i>c</i>	0.037768	0.027136
<i>d</i>	$3.901618 \cdot 10^{-4}$	$4.183364 \cdot 10^{-4}$

Table 4.2: Calculated parameter values for the Gompertz function (4.5).

Parameter	Parameter value	Parameter value
	upper blood vessels	lower blood vessels
$a$	48.634152	-40.084039
$b$	0.580623	3.591731
$c$	0.127587	0.176445

The first mentioned function (4.4) represents a *rational model*. The parameter values are shown in Table 4.1. The variable  $b$  represents a predefined parameter that takes values from the interval given in Table 4.3. *Gompertz function* (4.5) represents another model, the values are represented in Table 4.2. The range of values of the interval parameter  $a$  is also represented by Table 4.3. The *square root model* for upper vessel (4.6) represents the last representative of this group. The calculated parameter for  $a$  is 6.032641. The modified *square root model* is then used for the lower vessel. The calculated parameter for  $a$  is 6.59736. Last two functions does not offer the option to select an interval parameter, so the only possible one is selected. The range of values is shown in Table 4.3.

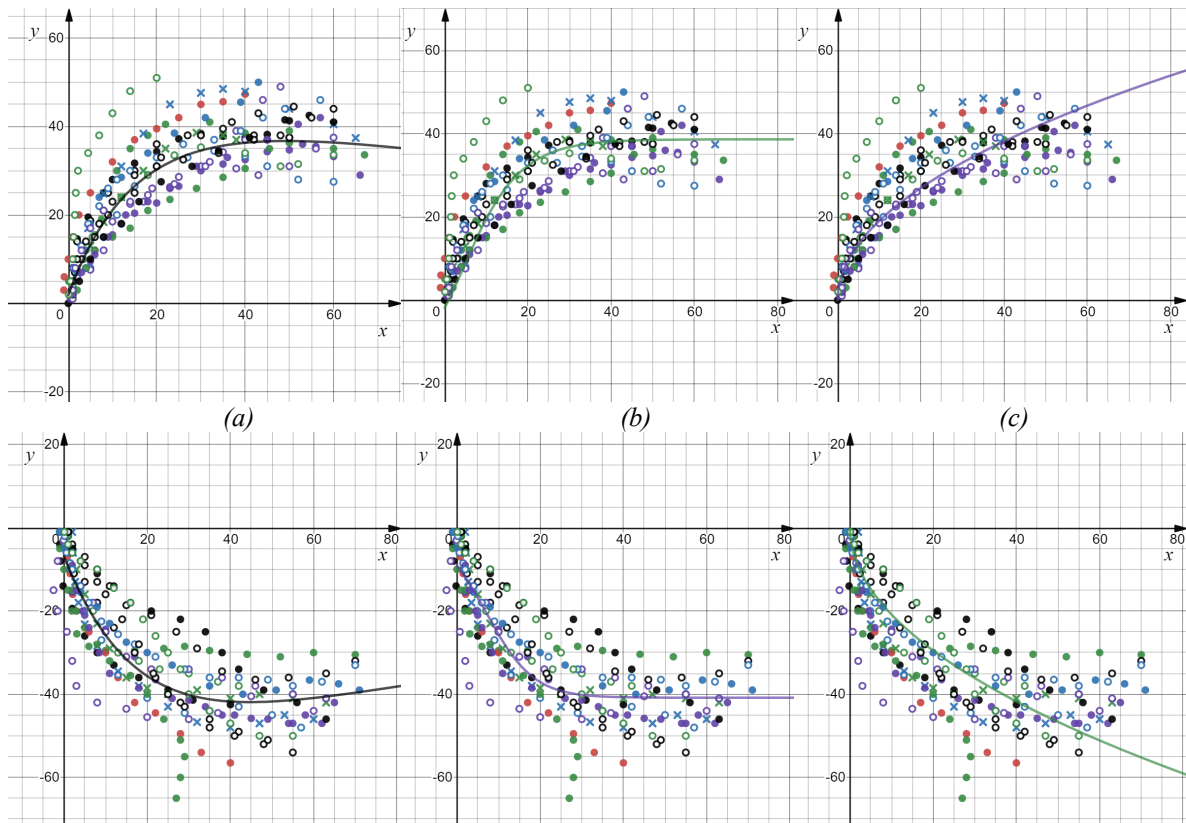


Figure 4.13: A mathematical functions plotted in the coordinate system for the upper (top) and lower (bottom) vessels. Rational model (4.4) (a), Gompertz function (4.5) (b), square root function (4.6) and (4.7) (c).

#### 4.2.1.2 Correction of interval parameters for upper macular vessel models

Table 4.3 describes the range of individual mathematical models. These are shown in Figure 4.14. The given parameter range of values first was optically set to contain the largest possible number of points. In the next phase, the estimated values were corrected. Graphs in Figure 4.14 was added to other

random images of real retinas. This was done as described in subchapter 4.2.1 (the entry of the vessel into the image in the *optic disc* corresponds in the coordinate system of the point  $[0; 0]$ ). 200 randomly selected vessels from the *Messidor* database were used for correction. The parameters were adjusted until at least 90% of the vessels were in the area. This limit seems sufficient for further work. This creates space to create another mathematical model that will cover other blood vessels.

Table 4.3: Parameter for specific functions and their interval range of values.

Mathematic function	Parameter	Start of interval	End of interval
Rational function (4.4)	$b$	2.135	3.824
Gompertz function (4.5)	$a$	39.143	55.876
Square root function (4.6) and (4.7)	$a$	0.014	0.043

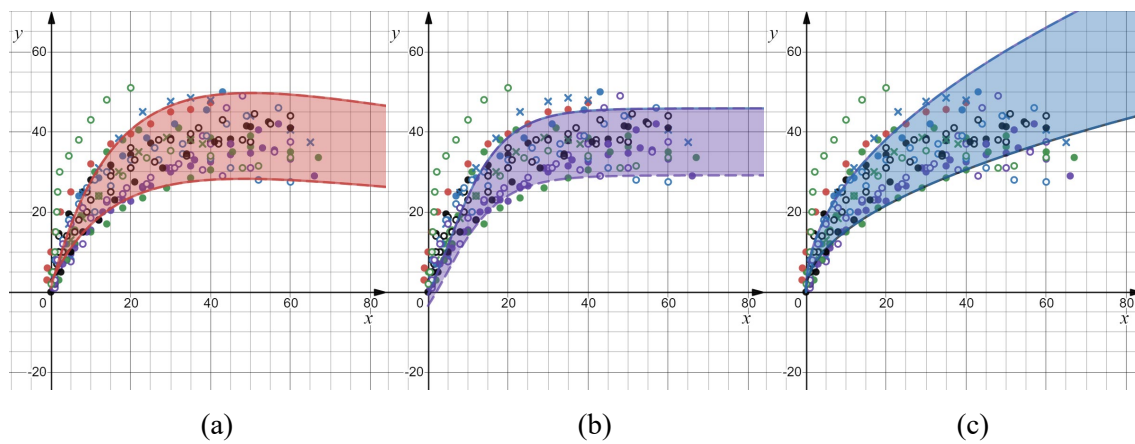


Figure 4.14: Areas covered by functions, plotted in a coordinate system. Area covering rational functions (4.4) (a), area defined by Gompertz function (4.5) (b), space occupying square root function (4.6) (c).

#### 4.2.1.3 Evaluation of similarity of upper and lower macular models

To determine the identity of the models with the upper macular vessels, the functions were moved from the *IV* to the *I* quadrant of the coordinate system. The transfer was performed by an absolute value function. The values were mirrored over the  $x$ -axis of the coordinate system. The relocated functions were compared with the areas of the upper macular models. The *Gompertz* region was associated with a *logistic regression* curve. The remaining models were associated with areas that created identical models. The results are represented by a set of Figure 4.15. From this finding, it is possible to use upper macular vessel models to form the lower macular vessels. This transformation can be realized by multiplying the range of values with the constant  $-1$ . The measured points of the lower macular vessels were transferred from the *IV* to the *I* quadrant of the coordinate system and the parameters of the enumerated models for the upper macular vessels were corrected.

#### 4.2.1.4 Detection of the direction and shape of the upper and lower nasal vessels

80 vessels from the *Messidor* database were also used for processing as when working with vessels in the macular area Figure 4.12. Marking of points took place in the *Desmos* web program.

The same magnification and shift of the image was used as in the case of detection in the macular area. The image was enlarged to 170×120 and shifted so that the vessel's entrance into the retina corresponded to the origin of the coordinate system ([0;0]). The distance between the individual points of a given curve was close to the five internal units of the program.

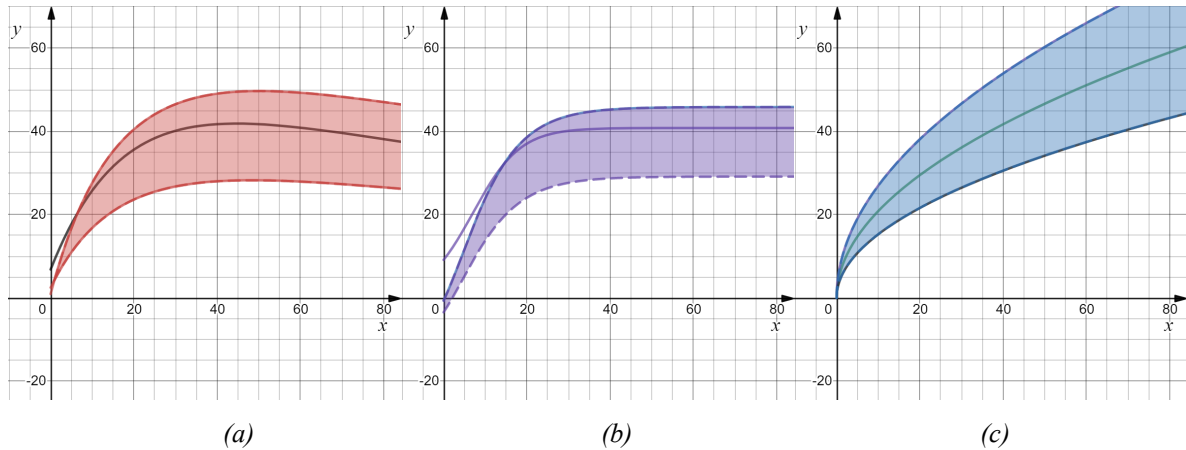


Figure 4.15: Areas covered by upper macular vessel models in which the lower macular vessel curves are found in absolute value. Rational model (a), Gompertz function and logistic regression model.

#### 4.2.1.5 Approximation of detected nasal vessel shapes by nonlinear models

The knowledge from subchapter 4.2.1.3, similarity of upper and lower macular vessels, was used in this approximation. This knowledge was transferred to the lower and upper nasal vessels. First, the unified nasal data was unified. The points of the lower nasal vessels were transformed from the *III* to *II* quadrant of the coordinate system as a function of the absolute value. *CurveExpert* and *RegressionTools* processed double the amount of data. They created a list of the most suitable mathematical models. The individual results were optically validated to see if they met the natural shape of the vessels. This inspection mainly focused on the location behind the last measured point. Subsequently, the interval parameters for the individual functions were determined. The conclusion of the subchapter describes the verification of the validity of the similarity of the upper and lower nasal vessels. This was done by comparing the areas that fill the individual models with the measured points for the lower nasal vessels.

$$f(x) = \frac{ax}{x-b} \quad (4.8)$$

Table 4.4: Determined parameters for the function from equation (4.8).

Parameter	Parameter value
<i>a</i>	48.712318
<i>b</i>	26.837965

#### 4.2.1.6 Acquired nasal vessel functions

Selected models with the best ratings show the mathematical rules in this section. A table of parameters that specify the function also belongs to the individual regulation. The end of the subchapter shows the selected curves. These show only one specific vessel. The following section deals with the issue of transferring one vessel to the whole area.

$$f(x) = a(-x)^b \quad (4.9)$$

Table 4.5: Determined parameters for the function from equation (4.9).

Parameter	Parameter value
$a$	3.734543
$b$	0.533671

$$f(x) = c \left( \frac{bx}{a} \right)^{\left( \frac{1}{b} \right)} \quad (4.10)$$

Table 4.6: Determined parameters for the function from equation (4.10).

Parameter	Parameter value
$a$	0.323413
$b$	1.896438
$c$	1.412325

The first model represents the polynomial function (4.8), the calculated parameters of the model are shown in Table 4.4. The power model (4.9) represents another of these curves. The determined parameter values for this curve are shown in Table 4.5. The last representative represents the square root function (4.10), where the specified values of the variables are contained in Table 4.6. The individual functions of the nasal vessels are shown in Figure 4.16 in the coordinate system.

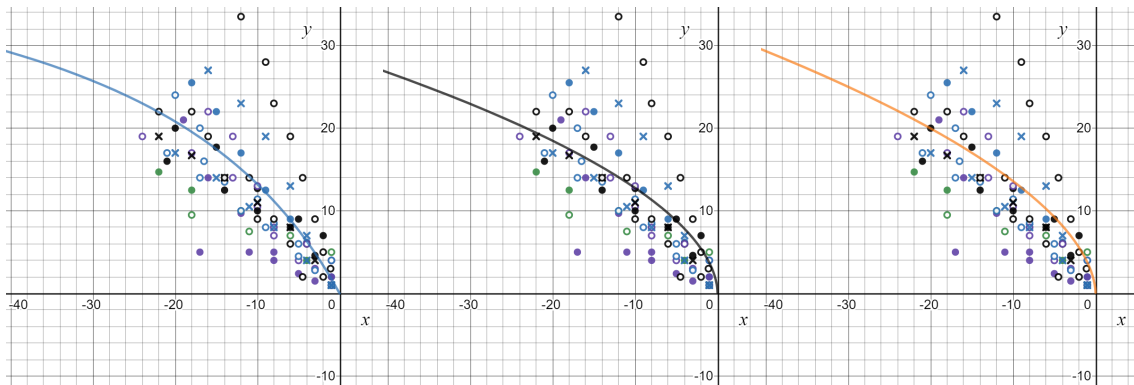


Figure 4.16: Mathematical models displayed in a coordinate system. Angled function (4.8) left, power model (4.9) middle and square root curve (4.10) right.

#### 4.2.1.7 Determination of interval parameters and their correction for nasal vessel models

In this part, the parameters for individual models of nasal vessels were determined. It is necessary that the predetermined parameter acquire an interval of values. This guarantees better randomness of the vessels. The interval limits were set so that at least 90 % of the measured points fit within the marked area. The resulting values is showed in Table 4.7. Graph set in Figure 4.17 shows the areas that define the individual models with their parameters.

Subsequently, the empirically determined ranges of values were corrected. 100 images were randomly selected from the *Messidor* database. The images entered in the coordinate system were compared with the model areas. Their parameters were adjusted until at least 90% of the vessels were in the areas. This

boundary seems to be precise enough for further work. If the accuracy created in this way is not sufficient, it is possible to add another model that will cover the identified shortcomings.

Table 4.7: Field of parameter values for specific models of nasal vessels.

Mathematical function	Parameter	Start of interval	End of interval
Rational model (4.8)	$a$	22.4563	110.4456
Powers model (4.9)	$a$	1.3234	8.7434
Square root function (4.10)	$c$	0.8124	2.6235

#### 4.2.1.8 Lower and upper nasal vessels similarity verification

To verify the similarity, the knowledge in subchapter 4.2.1.3 on the similarity of the upper and lower macular vessels was used. This finding was also used for the nasal part of the retina. Validation for nasal vessels was also performed by comparing the areas of individual mathematical models with the measured points of nasal vessels. The second phase of verification compared the lower nasal vessels from the existing retinas of the *Messidor* database with the areas that define the calculated models. The functions covered over 90% of the measured points of the lower nasal vessels. The success of verification using existing retinas achieved almost identical results. This knowledge can also be used to create nasal vessels.

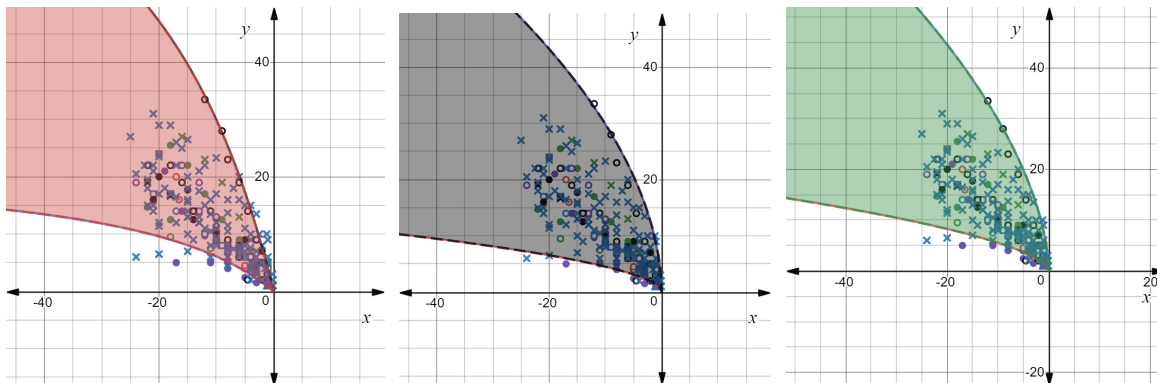


Figure 4.17: Areas filled with functions for nasal vessels. The area filling the rational model (4.8) (left), the area defined by the power of the function (4.9) (middle), the space defined by the mathematical model of the square root (4.10) (right).

## 4.2.2 Identification of vessel shapes and branches

The observed part of the retina was divided into four sectors. The division is described in Figure 4.18. The retina was divided into nasal and macular parts. The two parts are separated by a curve representing the main vessel. Each of these sectors represents a different behavior of the blood vessels that are found in it. The examined images come from the *Messidor* database.

All sectors were observed. Firstly, were detected the points of these vessels. Above the set of points, a mathematical apparatus was created that brings the behavior of these vessels as close as possible. The next part of the chapter is devoted to determining the correct angle between two vessels at the point of their branching. To avoid a large number of branches, the maximum number of branching was measured in subchapter 4.2.2.4.

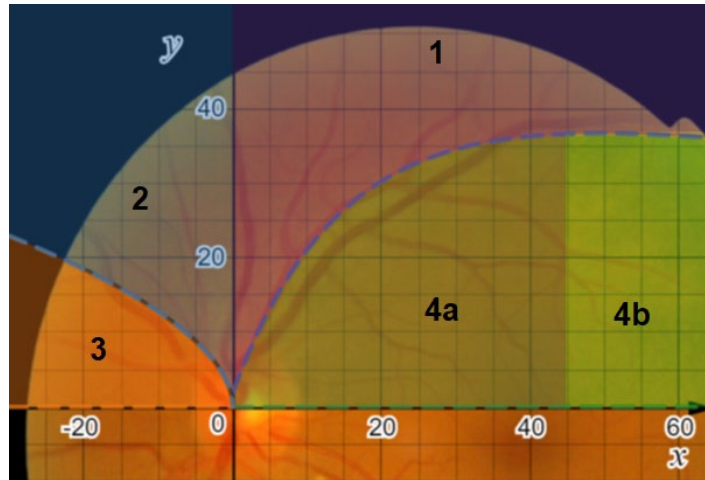


Figure 4.18: An image of the eye retina divided into four parts. The macular vessels above the main macular vessel (1), the nasal vessels in the direction of the y-axis (2), the nasal vessels parallel to the x-axis (3) and the macular area where the vessels point to the fovea - this part is later divided into vessels pointing to the fovea (4a) and vessels to the x-axis (4b).

#### 4.2.2.1 Detection of vessel direction and shape

Marking and presentation of points took place in the *Desmos* program. The image was enlarged to  $170 \times 120$  units. The image was shifted so that the branching of the examined vessel was located at the start point of the coordinate system  $[0; 0]$ . The distance between the individual measured values was close to the five internal units of the program. The obtained data is displayed in a set of Graphs on Figure 4.19.

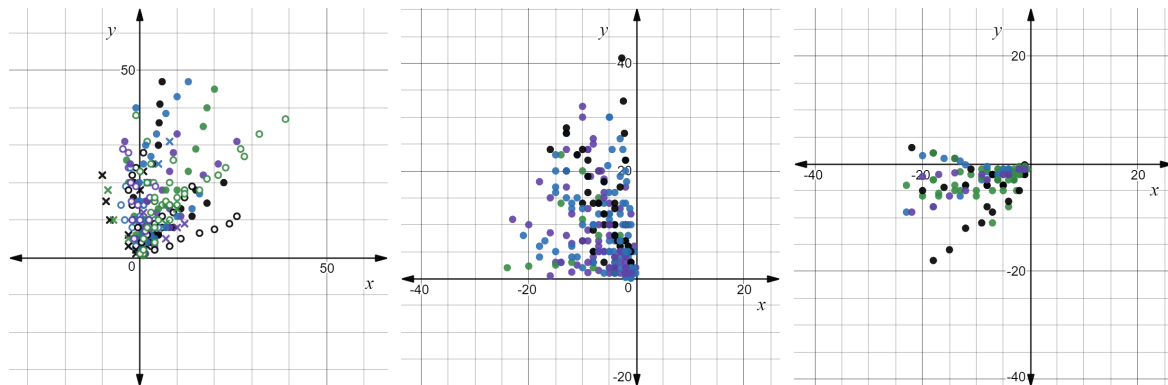


Figure 4.19: Measured points of vessels emanating from the main vessels in the coordinate system. Upper macular sector (left), upper nasal part (middle), lower nasal vessels (right).

The obtained data were processed by *CurveExpert* and *RegressionTools* applications. The resulting curves for each part of the retina did not correspond to an exact approximation. The resulting functions did not reach the accuracy of previously obtained models. The main problem with the inaccurate approximation seemed to be a very wide triangle of data, where the data occupied almost the entire quadrant of the coordinate system with almost identical representation of points. Figure 4.19 middle shows this phenomenon the most.

The calculated results excluded the possibility of using mathematical functions to represent the measured values. Another important factor that prevented the use of this approach was the inability to define multiple values from a range of values in a function for one value from a domain.

The area of the vessel pointing to the *foveal* area (area 4 in Figure 4.18) was not measured in the same way as the others. The area has different and better-monitored characteristics. The most important observed pattern of behavior appeared to be the target vessel. These generally point, when inserting the image into the coordinate system (subchapter 4.2.2.2), to the  $x$ -coordinate axis. This pattern can be divided into two subcategories according to the position of the vessel. In the first group, the vessels point to the *foveal* part (area 4a in Figure 4.18). The second group of vessels, which points to the  $x$ -coordinate axis, shows a different behavior (area 4b in Figure 4.18).

The boundaries in the each monitored retina areas was differed. Even in most cases, they intersected and it was not possible to clearly identify the turning point. The best approximation of this boundary appeared to be the end of the *foveal* region. The vessels point to the *foveal* area, but are no longer visible in this area. Visually, they disappear at the edge of this space, some disappear before this horizon.

#### 4.2.2.2 Realization of vessels using vectors

Better predispositions have vectors. By their definition, they eliminate the problem of mathematical functions, namely to assign more values from the range of values to one value from the domain.

The problem of misidentification of the directions and shapes of the vessels come out from the main macular and nasal vessels could not be solved with one variable (vessel vector). Another element had to be added. The angle at which the vessels were branched was chosen as a suitable element.

To eliminate the problems, it was eligible to keep the vectors in a normalized shape. This represents the vector component  $x$  to keep at size 1. Each vector takes on the value  $x$  from the set  $\{-1; 1\}$ . The  $y$  component represents information about what slope and direction the given vector represents.

The vector representation removes realistic vascular curvature and sets only a straight line. To create a more realistic behavior of the vessels, it was necessary to add mechanisms for curving the vector. The first mechanism is a longer-term solution. In each calculation of the direction of the vessel is take into account the direction of the vessel from which it branches. The calculation of the new direction represents the equation (4.11);  $x$  and  $y$  represent the components of the newly obtained vector for the direction of a particular vessel; the symbols  $x_a$  and  $y_a$  represent the individual components of the vector that describes the current vessel;  $x_p$  and  $y_p$  represent the vessel vector from which the currently counted vessel branched. The coefficient of similarity with the parental vessel  $c$  was set to 0.2.

$$\begin{aligned} x &= \frac{x_a + x_p c}{|x_a + x_p c|} \\ y &= \frac{y_a + y_p c}{|x_a + x_p c|} \end{aligned} \quad (4.11)$$

If the parent vessel is represented by a mathematical function and not a vector, the derivative over this function will be calculated and converted to a vector. Avoiding derivation would mean a big simplification of the calculation, so an alternative was realized where an approximate derivative is created by subtracting the value ( $x$ ) from ( $x + 1$ ). Where  $f$  represents the function of the vessel shape.

The second local mechanism performs a random deviation from the original exact point value that the vessel interpolates. The entry of partial inaccuracy is described by mathematical equation (4.12). This mechanism adds or subtracts a maximum of 5% of the current function value. For the correct operation of the mechanism, it is necessary to generate random values of the parameter  $c$  in the interval  $\langle -1; 1 \rangle$ .

$$y = y + 0.05yc \quad (4.12)$$

The creation of a new vessel, which will be represented by a vector, arises as follows. It is necessary to know the vector that represents the vessel from which the branching takes place. If this vessel is represented by a function, it is necessary to calculate the derivative and convert it to a vector (see above). Using equations (4.13), the current vector is converted by an angle  $\alpha$ . The newly created vector must pass normalization by rule (4.14), because the transformation of the rotation does not leave the component of the vector  $x$  in one form.

$$\begin{aligned} x &= x_p \cos \alpha + y_p \sin \alpha \\ y &= y_p \cos \alpha - x_p \sin \alpha \end{aligned} \quad (4.13)$$

In Equation (4.13),  $x$  and  $y$  represent the components of the newly formed vector. The symbols  $x_p$  and  $y_p$  define the original vector. The  $\alpha$  character specifies the size of the angle by which the vector will be rotated.

$$\begin{aligned} x &= \frac{x_p}{|x_p|} \\ y &= \frac{y_p}{|x_p|} \end{aligned} \quad (4.14)$$

Regulation (4.14) describes a vector, which normalize the component  $x$  from the original  $|x_p|$ . The same division at  $y$  is also performed, where the original value of  $y_p$  is divided by  $|x_p|$ .

#### 4.2.2.3 *Measurement of angle sizes at vascular branch points*

To create a branching of vessels is necessary to know the angle at which they will diverge. In the first part of this section were measured several vessels in the existing retinas. Due to the problems associated with the measurement, the empirical determination of the size of the angle was changed. To maintain compatibility with the existing instrument, it was necessary to introduce the percentage width of the vessels into the measurement. In the resulting relationship (4.15), this represents  $r$ . This symbol indicates what percentage of the original width represents the newly formed vessel during branching. If two branches of the same size are formed from branching, this unknown one will take the value 0.5. The sum of the vessel widths must reach 1 for each branch.

The original vessel, from which branch another, deviates in the opposite direction, this was found during measurement. The size of the angle by which the original vessel deviates from its direction depends on the size of the new vessel width. To perform this phenomenon can be used a relationship (4.15) with the width of the original vessel and multiplying the size of the angle by -1. Variable  $r$  takes values from the

interval  $\langle 0; 1 \rangle$ . The resulting magnitude of the angle  $\alpha$  contains the values from the first quadrant of the goniometric circle  $\langle 0; \frac{\pi}{2} \rangle$ .

$$\alpha = \frac{\pi}{2} - \frac{r\pi}{2} \quad (4.15)$$

The ratio system of vessel branching widths was taken from the original generator in Chapter 4.1 and slightly modified. From empirical testing, the branches of similarly large vessels reached widths in the range of  $\langle 0.55; 0.7 \rangle$ . Small vessels, which mainly go to the fovea area, take values from the interval  $\langle 0.04; 0.08 \rangle$ .

#### 4.2.2.4 Determination of vascular branching depth

Depth of branching was also observed for more accurate vessel behavior. This property describes how many times a given vessel branches above the visible part of the retina. The measurement was applied to the areas of the retina (shown in Figure 4.18). The nasal parts showed almost the same results, so the two areas were merged into one. A description of the procedure for classifying individual vessels into groups of immersion levels is shown in Figure 4.20. The measured vessel belongs to only one group, according to all the branches shown by the visible part of the retina.

Retinal images is from the *Messidor* database, where were randomly selected 25 images. Measurements in each image detected retinal veins and arteries. Measurements were performed with 50 vessels in each area. The number is on the verge of relevance. The results were unambiguous, so it was not measured on a larger sample of data.

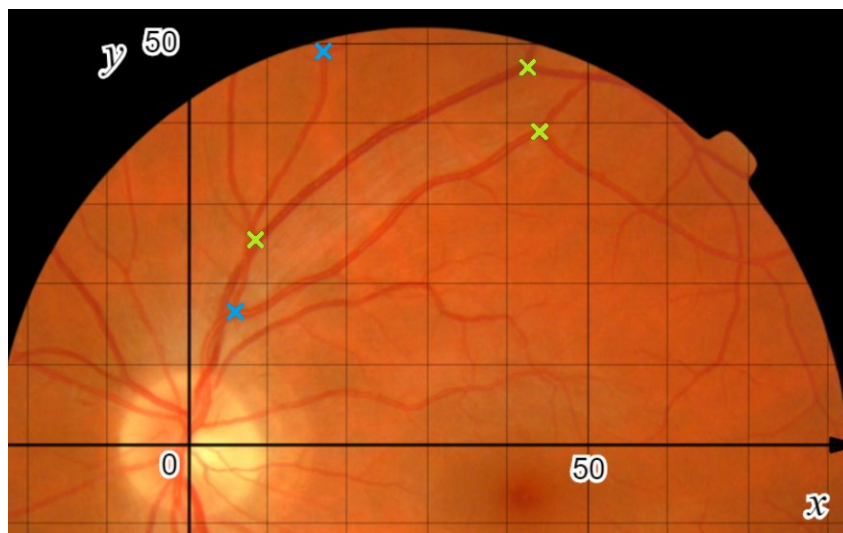


Figure 4.20: Image of the retina displayed in the coordinate system. Blue crosses indicate a vessel that belongs to the group of the second level of immersion. The vessels marked in green fall into the first level of immersion. Some vessels that branch above the macular curve are marked.

The results obtained for vessels leading to the macular area are shown in Table 4.8. These most often branch twice with a measured probability of 56.7%. Branching of vessels that branch four times is negligible, with a probability of 1.8%.

Table 4.9 describes the measured results of vessels that branch above the macular curves. Those with more than a two-thirds probability branch only once on the visible part. The group of three branches with a probability of 4.1% shows almost negligible results.

Nasal areas are shown in Table 4.10. It contains data for all vessels that branch in the nasal area. In the vast majority of cases, they branch only once with a measured probability of 80.6%. With a minimum percentage, a group with three branches appears.

*Table 4.8: Values describing immersion in vessels leading to the fovea.*

Branching level	Number of vessels	Percentage
1	40	23.4%
2	97	56.7%
3	31	18.1%
4	3	1.8%

*Table 4.9: Results describing immersion in vessels above the macular curve.*

Branching level	Number of vessels	Percentage
1	67	68.4%
2	27	27.6%
3	4	4.1%

*Table 4.10: Values describing immersion in blood vessels throughout the nasal area.*

Branching level	Number of vessels	Percentage
1	83	80.6%
2	18	17.5%
3	2	2.0%

#### 4.2.2.5 Approximation of branching positions from vessels prescribed by a mathematical function

As part of the more regular branching of the vessels was measured the number of vessels branching from the main macular vessel. The values were then empirically adjusted and rounded. These branch points are generated, when generating a riverbed for one vessel is started. These points are stored in the queue and subsequently removed from it when they are created. Empirically determined values are shown in Table 4.11.

*Table 4.11: The number of branches at the main vessels and the range of positions they can assume.*

Interval	Number of branches		
	I	II	III
1	{3;24}	{2;15}	{2;15}
2		{20;40}	{15;35}
3			{35;60}

The first position is randomly calculated from the interval. The value of the distance from the center of the previously generated point is also added to the calculation of other positions. This correction ensures that the generated points will have a certain distance from each other.

### **4.2.3 Summary of achieved results**

In this chapter was identified the shape of the main vessels, which are located in the visible part of the eye's retina image. Were calculated three mathematical models for each group of major vessels. For each model, the calculated parameter values were verified and corrected with real retinal images. An assumption was made about the same vascular behavior in the upper and lower regions. This assumption was confirmed by proper testing of upper vessel models on measured lower vessel values on existing retinal images. This feature allows the unification of the logical parts of the retina of the eye. It will also be possible to work only with the upper nasal and macular areas. The results of this work were transferred to the corresponding lower areas.

The second part dealt with the vessels that emanate from the main curves. The first assumption of the use of mathematical functions was not fulfilled. The observed blood vessels showed significant deficiencies. Vectors that are more flexible in many ways are a better model. Therefore, a branching system using vectors was designed. It uses an object rotation transformation. The vector is rotated by a certain angle, which affects the width of the newly formed vessel. The width of the vessel is used by the existing synthetic retina generator, and this feature has been retained and used to ensure compatibility. In the last part, the chapter dealt with the number of branches of each vessel. The measurement divided the retina into three parts due to the similarity of the results. The number of branches was measured for each area. More detailed results and implementation of the acquired knowledge into the synthetic retina generator from Chapter 4.1 can be found in [122].

This whole work deals with the identification of significant points for the purposes of biometrics. The last mentioned chapter can be a guide for the continuation of this work, or suitable for understanding the dependence of blood vessels in the vascular bed. This makes it possible to find connections between bifurcation positions and thus slightly reduce the resulting biometric entropy. However, this effect is probably very small, so we will not count on it further.

## **4.3 Synthetic images generated via neural network**

In another application, we first generate healthy images, where we can train algorithms for detection and extraction of the optic disc and fovea. Furthermore, we generate diseased retinal images with manifestations of ARMD and diabetes, e.g. hemorrhages, exudates. The neural network learns such images, which we have in the training set. Now, we only have images for ARMD and diabetes; however, new images are stored in the database, i.e. it is possible to add new features representing new ophthalmologic diseases.

In biometric systems, it is often the case that a damaged image does not pass through the recognition. However, there is often not enough training data for detection algorithms. Therefore, it is advisable to create large databases of synthetic images with diseases.

We have trained Generative Adversarial Networks (GANs) [32] to generate synthesized retinal images. A GANs-based retinal image synthesizer consists of two neural networks: a generator (G) and a discriminator (D). We have not used any extra information (such as blood vessel trees) to generate retinal images using GANs. However, we have emphasized maintaining a balance between the two competitors G and D during training. We have found that if this balance is not kept, G may end up generating only blurry retinal images without high-level structures, such as blood vessel trees, optic disc, macula, etc.

Algorithm of GANs based Retinal Synthesizer is as follows:

- For  $k$  times
  - Prepare a mini-batch of retinal images  $\{(x, \hat{x})_{i=1}^m\}^{kn}$  where  $m$  is the mini-batch size.
  - Update  $D$  using  $\{(x, \hat{x})_{i=1}^m\}^{kn}$ .
- For  $r$  times
  - Prepare a mini-batch of noise vectors  $\{(z)_{i=1}^m\}^{rn}$ .
  - Update  $G$  using  $\{(z)_{i=1}^m\}^{rn}$ .

We have used 1,200 images from the public database *Messidor* [26]. In our experiments, we resized all images to the same size (i.e.,  $256 \times 256$ ) by *bicubic interpolation* [51]. We have followed the deep convolutional neural network-based architecture suggested in [33] with minor modifications. Figure 4.22 shows the model architecture for  $256 \times 256$ -sized images. The mini-batch size was set to 32 (i.e.,  $m = 32$ ). Noise vectors were drawn from the uniform distribution. As a loss function, binary cross-entropy was used. As an optimizer, *RMSProp* with a learning rate of 0:0001 and a decay of  $3 \cdot 10^{-8}$  was used. The dropout value was set to 0:5. For batch normalization, momentum was set to 0:5 instead of default value 0:99. For *LeakyReLU*, it was set to 0.2 instead of the default value of 0:3. For all convolutional and transposed convolutional layers, stride = 2, kernel size = 5, and padding = same was used. L2 regularization was applied only for weights and biases of the transposed convolutional layers. For all other settings, the default values of *Tensor Flow's Keras API* were used.

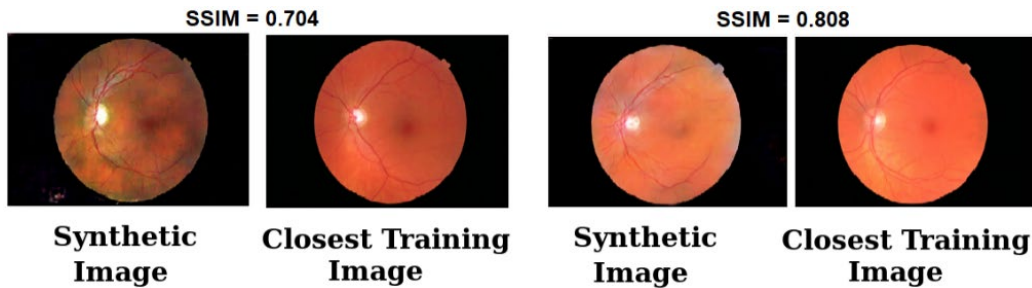


Figure 4.21: Comparison of synthetic image and the closest training image from the database.

After training, the generator is used to generate synthetic retinal images from noise vectors. The *Structural SIMilarity* (SSIM) measure shows how similar the synthesized images are to the training data.  $SSIM=0$  means there is no similarity and  $SSIM=1$  means that two images are the same. You can see some achieved results from this GAN generator of synthetic retinal images in Figure 4.21 and Figure 4.22.

On our STRaDe research group at Faculty of Information Technology, Brno University of Technology we generated sample database which is separated into two parts: healthy images and disease-affected images, which is especially diabetes and ARMD.

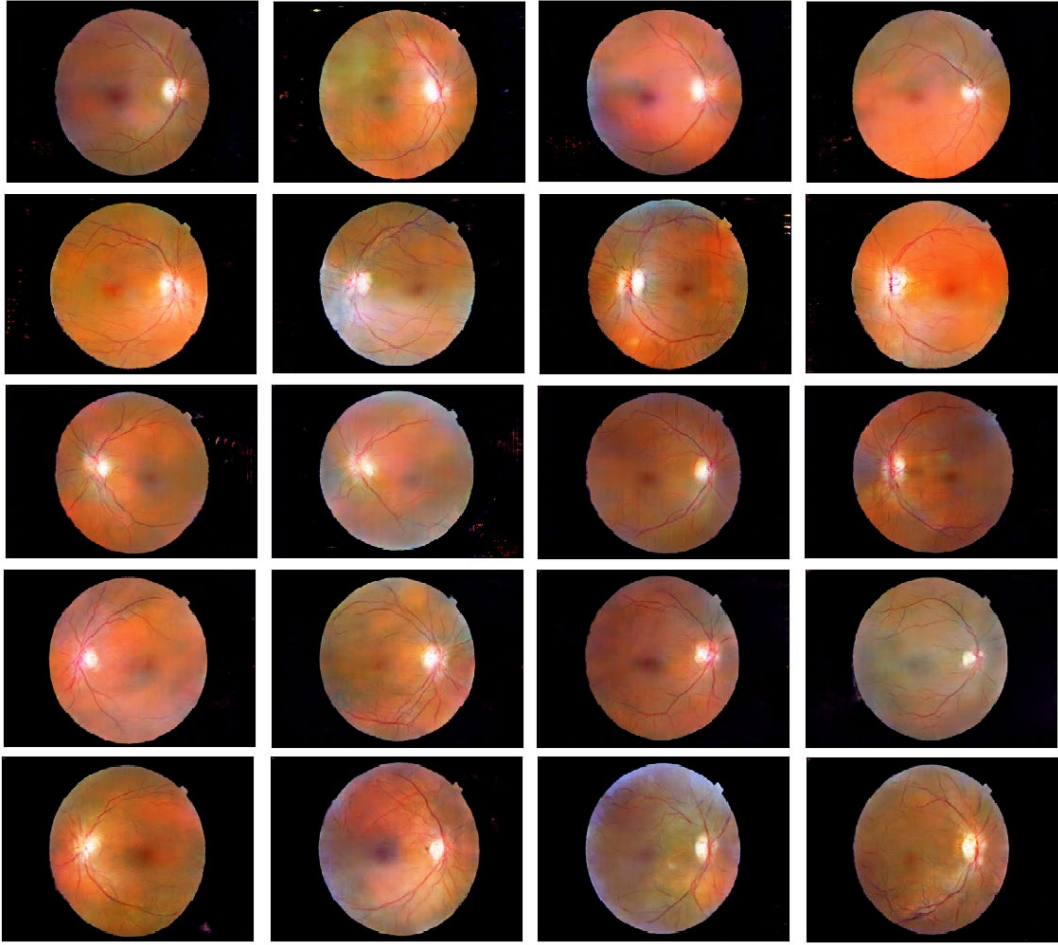


Figure 4.22: Examples of generated synthetic retinal images.

## 5 Statistical evaluation

The distribution of vascular lines in the retina of the human eye is unique (as shown in Chapter 2.4), which is similar to the ridges (papillary line) on the human fingers. Currently, there is no single approach to retinal recognition. Our procedure follows dactyloscopy, where bifurcations, terminations, positions and directions of a detected point are stored. We look for "anomalies" on the vessels in the retina – the places of visual crossings and bifurcations – and also record their position within the retina. For images, it is not easy to recognize whether it is a crossing or bifurcation of a vessel as the two phenomena often overlap. Therefore, we are only interested in the feature and not on its specific type. The termination of the vessel takes place "until lost" so a specific place cannot and will not be detected. We locate the points according to the position relative to the optical disc and the fovea. Therefore, we also store their position within the image as will be further described in Chapter 5.1 – (the coordinate system). The result is a set of vectors such that the system is not affected from the changes in retinal scanning (different rotations, zooms, or bevel).

Recognition becomes problematic in the presence of diseases that are manifested by a change in the retina such as bleeding. As with other biometric features, a relatively large amount of human health information can be read from retinal manifestations. Therefore, it is appropriate that the biometric facility manager guarantees the non-misuse or non-storage of this sensitive data, for example under the GDPR Directive [22][30].

If we take a brief look at some images of the human eye retina, we discover that crosses and bifurcations are not equally frequented in various areas. The probability of their occurrence is in some areas higher, in others almost zero. In the beginning, it should be noted that the ability to mark intersections and bifurcations strongly depends on the quality and contrast of the image. In the statistically empty parts there are the very small capillaries that are undetectable in the image using automatic or manual search. When we create the frequency map, the points can be regarded with different weights to recognize the pattern. Finding matching points in two retinas being compared in rare occurring sites may score higher than matching points in other areas. Therefore, we tried to statistically evaluate several hundred retinal images and create our own frequency scheme, which we will later use to adjust the evaluation when comparing two retinas.

Our main goal is to determine how diverse the objects on the retina are. We want to find out how suitable the retina is for biometric purposes for human recognition. Our goal is to calculate the degree of randomness of crossing and bifurcation of blood vessels. In this work, we shorten the term to *biometric entropy* (see 2.6.1) [59].

## 5.1 Coordinate system

In order to be able to work uniformly with all retinas without major complications, we have introduced a polar coordinate system, where two values can be used to align the retinal image to same coordinate system with the others. Our coordinate system assumes distances between the optical disc and the fovea in the different retinas approximately similarly. We also assume, if the physical structure of the retina differs significantly, that its development proceeded by similar rules. For example, if the distance between the optical disc and the fovea is smaller than average, the entire retinal structure will be smaller, and this will not affect our system.

The main point of the entire coordinate system is the center of the optical disc. In the records of individual retinas, its position in a particular image is stored as the distance from the left and top of the image edges. In addition, the width and height of the optical disc area (1<sup>st</sup> line of the output text file) are stored here as well. The second record is the center of the fovea (2<sup>nd</sup> line). The width and height of fovea are no longer stored here because its boundaries are difficult to ascertain by a simple look. The distance  $r$  between these two points is the basic unit of length for our coordinate system in each retina. This value may differ for every single image but is always valid for one retina. The second value is given point angle  $\psi$  of the direction from the optical disc. An angle of  $0^\circ$  lies in the line to the fovea and the value increases as it goes clockwise. This means that the fovea will have coordinates  $(1, 0^\circ)$  in all retinas according to our coordinate system. Bifurcations or crossings are expressed by  $r$  and  $\psi$ , respectively, and are stored on the next lines of the output file.

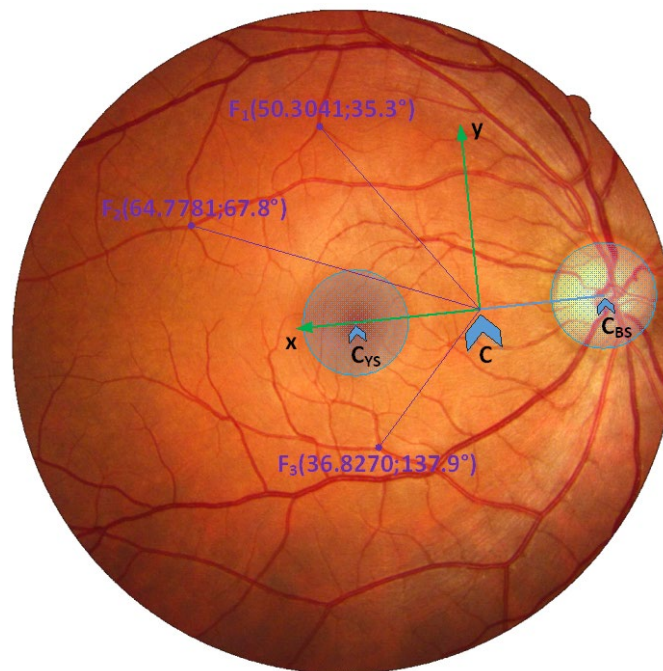


Figure 5.1: Coordinate system and three examples of points.

We convert the found bifurcations and crossings from the *polar* [52] to the *Cartesian coordinate system* [53] when we need to display or evaluate the entered points globally. To do this, we need the distance

between the center of the optic disc ( $C_{BS}$ ) and the yellow spot ( $C_{YS}$ ). Then, we calculate their *Euclidean distance* ( $d$ ) [54] and the angle between the centers of both points ( $\alpha$ ) according to the equation (5.1).

$$\alpha = \arctg2((y \cdot C_{YS} - y \cdot C_{BS}), (x \cdot C_{YS} - x \cdot C_{BS})) \quad (5.1)$$

Calculate the bifurcation/crossing distance from the optic disc using Eq. (5.2):

Using Eq. (5.2), we calculated the bifurcation/crossing distance from the optic disc:

$$v = r \cdot d \quad (5.2)$$

Then, calculate the coordinates  $dx$  and  $dy$  using Eq. (5.3) and (5.4).

Then, using Eq. (5.3) and (5.4), we calculated the coordinates  $dx$  and  $dy$ :

$$dx = d \cdot \cos(\psi + \alpha) \quad (5.3)$$

$$dy = d \cdot \sin(\psi + \alpha) \quad (5.4)$$

Lastly, calculate the point that resulted from the bifurcation/crossing in the Cartesian system [ $dx + x \cdot C_{BS}$ ;  $dy + y \cdot C_{BS}$ ].

## 5.2 Recognition scheme

The algorithm for determining the grade of conformity of the two retinas works by converting all points from the polar coordinate system (described earlier) to Cartesian coordinate system. It is not necessary to align or rotate both images. Due to the chosen system, which is based on the position of the optical disc and the fovea, these points on two retinas will always exactly overlap.

For the first point of intersection and bifurcation in the first retina, it is determined which set of points in the second retina is the closest one. Then, the same procedure is repeated for the point found from second retina – finding the closest point back in first retina. This will determine if the two points are really the closest. If we did not find points on both directions, as in the case of a marked point in only one retina, another point could be found, which has its pair from the first retina.

Figure 5.2 shows the scenario without two-way control. Green points from the first retina and blue points from the second retina are combined into one image. For a point in a red circle, we look for the nearest point that belongs to a pair with another point.

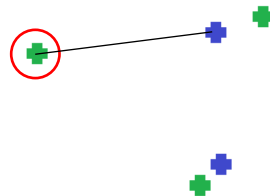


Figure 5.2: Illustration of finding the nearest point.

If the distance between the two found points is less than the specified limit, then they are not considered as close. If they are "close", they will be removed from the lists of both retinas and their distance is saved. Before saving, the distance value is converted to a percentage where 0% means zero distance

between points and 99% is the maximum allowed distance between two points to be considered as close. In addition, this value is then squared for better difference between near and far points.

The percentage value of the distance is then adjusted according to the statistical model described above. The value is multiplied by a number from 1 to 4 where a lower number means lower frequency in the statistical model. The reason is, if no nearby point is found in the high frequency region, then it is much worse for retinal conformity than if no point is found between two far points that are at distances from the optical disc. In addition, places with higher frequencies are usually closer to the center of the coordinate system where it is more accurate.

## 5.3 Used databases

For the testing purposes, we used several public or our internal databases. Messidor [26], e-optha [25], Drions-DB [69], High-Resolution Fundus (HRF) [27] and Retina EBD STRaDe (EBD).

First of them is publicly available database *Messidor* from team ADCIS was created for scientific work dealing with computer diagnostics of diabetic retinopathy. This database has 1,200 eye fundus color numerical images of the posterior pole. Three ophthalmologic departments captured the images: Hôpital Lariboisière Paris, Faculté de Médecine St Étienne and Centre Hospitalier Régional et Universitaire de Brest by using a color video 3CCD camera on a Topcon TRC NW6 non-mydratiac retinograph with a field of view of 45°. The captured images use 8 bits per color plane at 440×960, 240×488, or 304×536 pixels. There are 800 images that were captured with the pupil dilated (one drop of Tropicamide at 0.5%) and 400 without it.

Second one is database *e-optha* also from team ADCIS. This database has 47 images that are with exudates and 35 images without lesions. For our purposes, we use only images of healthy retinas.

The *Drions* database consists of 110 colorized digital retinal images from the Ophthalmology Service at Miguel Servet Hospital, Saragossa (Spain). Images are in RGB JPG format, and the resolution is 600×400 with 8 bits/pixel [69].

Next is *High-Resolution Fundus* (HRF) image database from German Fiedrich-Alexander University. The HRF database has 15 images of healthy patients, 15 images of patients with diabetic retinopathy, and 15 images of glaucomatous patients. Each image has a binary gold standard vessel segmentation image. Moreover, particular datasets are provided with masks to determine the field of view (FOV). A group of experts from the retinal image analysis field and the medical staff from the cooperating ophthalmology clinics generated the gold standard data.

The *European biometric database* (EBD) is internal set of iris and retina images our research group STRaDe (Security Technology Research and Development at the Faculty of Information Technology, Brno University of Technology (CZ), focused on security in IT and biometric systems). The database contains 684 images of both retinas from 110 distinct people, totaling 220 distinct samples.

Unfortunately, a significant part of this set consists of very low-quality pictures. Nevertheless, in this database all persons have several images of each eye.

For additional checking of our algorithms, we use our retinal fundus camera at our laboratory, which we use for several past years. We use 30 images from students, which were captured during Biometric systems course. Some images have bad quality, which is useful for testing applications in a worse condition. Several images are from same person eye (further as “school database”).

## **5.4 Developed applications**

We developed several applications to determine some properties of the retina, which will then be used to find out the degree of similarity of the two entered retina patterns. And ultimately for calculating the amount of biometric entropy.

### **5.4.1 Manual marking program**

The first application ( $SW_1$ ) is developed for manual retina marking by our students at the Faculty of Information Technology, Brno University of Technology. For the application purposes, we resize the images from the databases down to 1 megapixel. First, the edges of optical disc are marked. The application stores the top left position and the width and height of the ellipse around the optical disc. Then, the fovea is marked. Both positions are stored in Cartesian coordinates, which are based on the image properties and resolutions. Then are marked bifurcation or crossing points by simple click. These points are stored in polar coordinates. Data from the images are stored as a plain text file. By this application, we marked all retinal images using Messidor’s e-optha and HRF databases.

About 20 our students marked 888 retinal images. The diversity of people and the settings of their monitors cause different levels of visibility of individual capillaries. When we are marking the points, we ignored crossings inside optic disc, because the probability within this area would be very high, it is not considered in the biometric evaluation and sometimes these vessels can change during human life.

### **5.4.2 Automatic marking application**

The second application ( $SW_2$ ) stores the same information about the image as  $SW_1$ , except that it performs the steps automatically. Details of the overall work of the application, its steps, and further development are summarized in work [126]. The application is developed in Python and was used on the same images as  $SW_1$ . An average of 48 features have been found in these retinal images.

### **5.4.3 Application for comparison**

$SW_3$  compares the detection accuracy between the manually marked-up results by  $SW_1$  and the automatically marked-up results by  $SW_2$ . The algorithm is designed to compare the bifurcations/crossings that were selected manually, with the automatically detected set after they

have been detected. The paired bifurcations/crossings are automatically found through a method like that in Chapter 5.2.

The converted points are stored in the list with their position in it being used as ID for compiling disjunctive sets. A placeholder ID is assigned with -1 value. The problem is converted to an integer-programming problem [28] to calculate the minimum pairing. The edges are then determined between the graphs' individual vertices. The number of bifurcations/crossings that were manually found and paired can then be calculated. The resulting image for the comparison is shown in Figure 5.3.

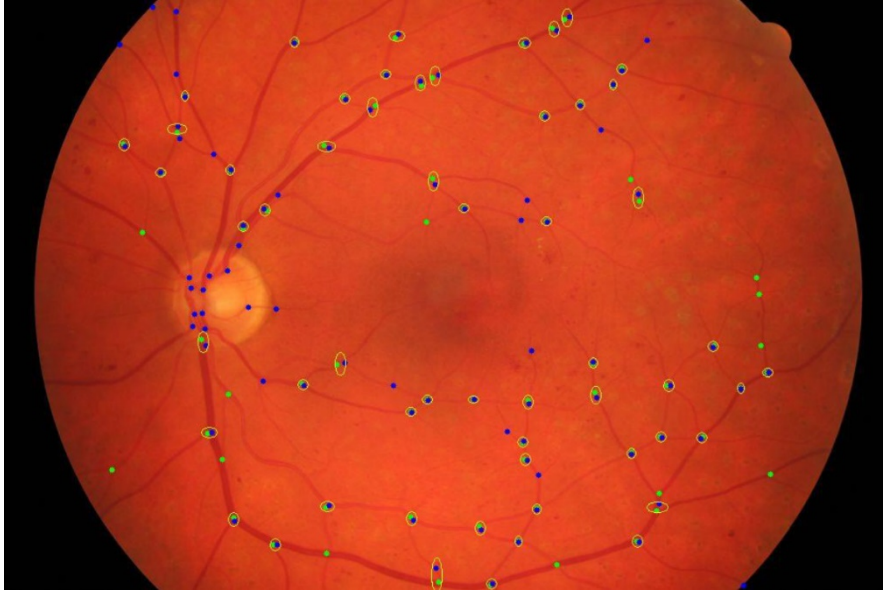


Figure 5.3: The resulting image for the comparison of manually and automatically found bifurcations/crossings.

For checking we used images from databases *Drions*, *Messidor* and *HRF* to compare our manually selected and automatically marked bifurcations and crossings in them. The results are summarized in Table 5.1.

Table 5.1: The summarized results for manual and automatic bifurcation/crossing detection.

Database	Average success rate [%]	Average marking error [%]	Average point spacing [px]
Drions images	62	47	5.25
HRF	66	31	4.55
Messidor (Base12)	74	65	4.25
Messidor (Base13)	79	63	5.01
Messidor (Base22)	61	45	4.65
Messidor (Base3)	82	72	4.95
Average	70.67	53.83	4.78

At the same time, we have modified and improved our algorithm that we tested on the *VARIA* database [29], which contains 233 images from 139 individuals. We conducted a classic comparison of found bifurcations/crossings that correspond to the fingerprint method. The DET curve is shown in Figure 5.4.

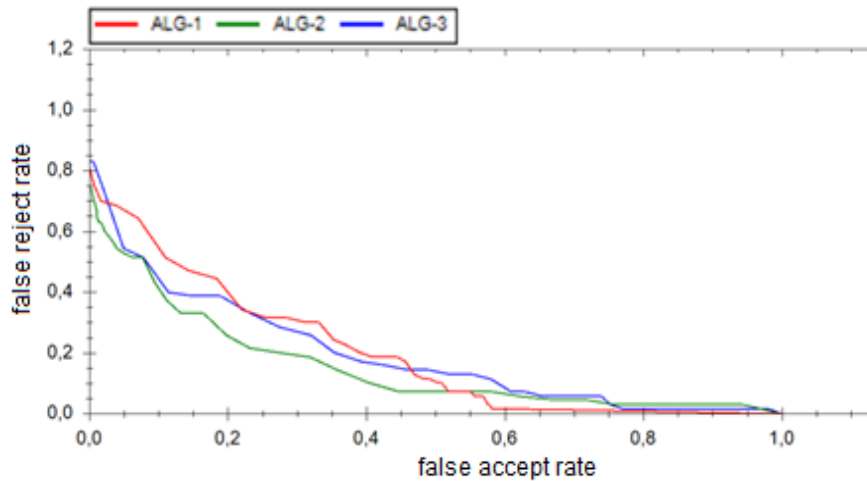


Figure 5.4: The DET curve for our three versions of the algorithm *RetinaFeatureExtractor*.

ALG-1 is an elementary algorithm that only shrinks' images to one-fifth, smoothes them, and equalizes the histogram. ALG-3 processes images as follows: after processing ALG-1, it detects an optical disc and fovea and then aligns the images to a uniform plane. Next, it highlights the vessels in the image and crops the compared area around the optic disc. ALG-2 compared to ALG-3 does not cut the image, otherwise on the optical disc area. Moreover, the resulting image is applied to edge detection. Source code of algorithms are available on [35].

#### 5.4.4 Visualization application

SW<sub>4</sub> collects the marked data by SW<sub>1</sub> and SW<sub>2</sub> in the previously described text file format into one picture. It collects individual pixels into a grid of adjustable size.

The program recursively scans all subfolders from the specified path and searches for all text files in which data about points in individual retinas are stored. SW<sub>4</sub> works with an array of 2,000×2,000 pixels. The program converts the polar coordinates in our coordinate system, described in Chapter 5.1, to the Cartesian one. It connects the individual bifurcation points together into the specified field. In the images, the fields with a higher frequency of occurrences are colored darker.

The program searches for and marks the effective area of the retina at 90% of the distance from the center to the edge of the retina. It also marks areas with significantly lower concentrations of bifurcation points around the blind and yellow spots, and also calculates what percentage of the effective area of the entire retina these empty elliptical areas occupy. It also allows the entire retina to be divided into regular areas and calculate percentage amount of bifurcation points in these parts.

For further purposes of the description, as a *pixel* will be defined one point in the base field 2,000×2,000 in image of all 888 merged retinas. One pixel can contain more *bifurcation* points. In the image, the higher number of bifurcations in one pixel is shown in a darker color. In the following text, a *new pixel* will appear, which is the sum of bifurcations from the original area at regular intervals (e.g. one new pixel forms 5×5 of the original pixels).

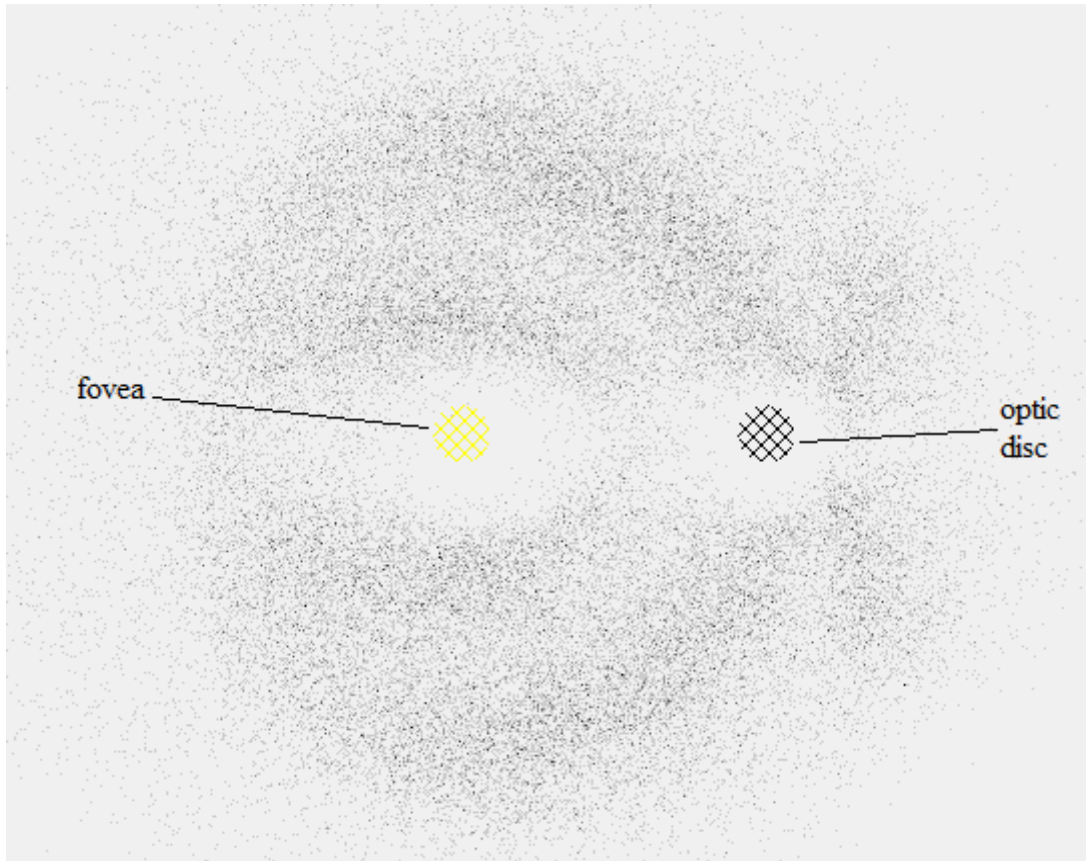


Figure 5.5: Combined image of all bifurcation positions in retinas. Darker dots are areas with more frequent bif. occurrence.

It combines the points according to a regular grid in steps of  $2 \times 2$  to  $10 \times 10$ . This grid then appears as the main image output program. It also allows to find out how many pixels far is the nearest point to another in the same retina. Finally, the algorithm determines the total center of gravity of all intersections, it can draw a circle from it, find out how many intersections (absolutely and in percent) are outside it and calculate how many points in the field are inside this circle.

We did not want to mark points inside the optic disc. Even so, some students marked these points at 215 retinas. We have therefore modified the program SW<sub>4</sub> to ignore these points. After that, SW<sub>4</sub> removed 988 points from these 215 retinas, but also 77 points from the remaining 673 retinas, which we thought were correctly marked. A total of 43,590 points were marked.

### 5.4.5 Recognition application

SW<sub>5</sub> works according to the recognition principle described in Chapter 5.2. For this purpose, we used database EBD, which has more images from one retina. We randomly selected images from EBD for 10 persons. Each have three images for the left and right eye, which are marked, e.g. 1002-2-R for person 1002's second image of the right eye. We mark all retinas by SW<sub>1</sub> very carefully. A specialist marked the first and third images of the eye such that at least 24 hours must have passed in between the marking of the retinas for the same person. The second images were marked by an ordinary computer user who is not involved in the project. Table 5.2 and Table 5.3 show the average results of evaluation after SW<sub>5</sub>.

Table 5.2: Recognition comparing results.

	Avg. value [%]	Min value [%]	Max value [%]
Comparison with second eye of same person	65.52	39.69	80.38
Comparison with different person eye	67.66	45.32	74.21
Comparison with our university database (different persons)	57.62	43.36	74.58

Table 5.3: Verification results.

	Avg. value [%]	Min value [%]	Max value [%]
Same eye, marked by different person	86.51	78.90	93.16
Same eye, marked by same person	93.54	88.54	95.78

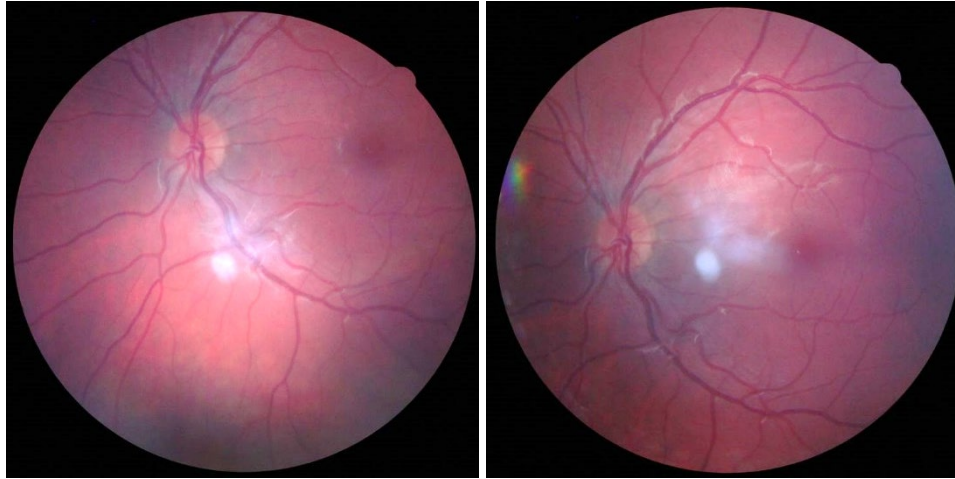


Figure 5.6: Sample of two images of the same retina in the EBD database.

Figure 5.6 shows two images of the same retina that are taken at significantly different angles. After the marking by  $SW_1$  and determining the similarity of the retinas by  $SW_5$ , the result was 91.09 %.

## 5.5 Basic field resolution

Furthermore, in  $SW_4$ , the distances of every two points in one retina were checked. As might be expected, during the recalculation, as expected, two different bifurcations in the same retina were not inserted at the same point after recalculation. In only one case, two bifurcations appeared right next to another. In Figure 5.7, it can be seen that checking the surroundings with a certain distance from one bifurcations does not mean that after merging the two bifurcations really fit into the same pixel. The number of indistinguishable bifurcations can be even smaller.

Two bifurcation points at a distance of two pixels from each other were found in only 4 cases out of all 888 retinas. Only 19 pairs of bifurcations lie at a distance of three pixels, which makes up 0.04% of the

total number of bifurcation points, i.e. a completely negligible amount. Other situations are described in Table 5.4. In addition, it also shows how many points would put into one new combined pixel at a given resolution over all 888 retinas in maximum (in image is the darkest color).

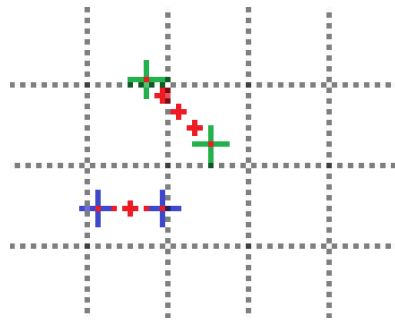


Figure 5.7: Two pairs of points (bifurcations) at a distance of 4 pixels. After merging with a 5×5 pixel filter, the two blue dots will be in the same new pixel, but the green dots in different ones.

According to the Table 5.4, we therefore find out that it is possible to merge points according to a grid of 5×5 pixels without a significant reduction in the resolution of the points, and thus without reducing the amount of biometric entropy found. To this result, however, it should be added that the degree of resolution was certainly influenced by the resolution of the retinal images and the way in which the vessels were crossed and bifurcated. On the other hand, better resolution would not help to find new points, only to focus them more precisely. The number of points would only increase the situation where thicker vessels cross at a very small angle. Then this situation could be referred to as two bifurcations instead of one crossing.

Table 5.4: The number of bifurcations with the specified distance in pixels and the maximum number of bifurcations in the new pixel after merging the specified areas.

Distance	Points	Ratio	Join	Max
0	0	0.00 %	1×1	5
1	1	0.00 %	2×2	9
2	3	0.01 %	3×3	13
3	19	0.04 %	4×4	20
4	86	0.20 %	5×5	27
5	213	0.49 %	6×6	38
6	560	1.28 %	7×7	44

## 5.6 Number of bifurcations in one image

The usual number of bifurcations in one image is a very important value, which then fundamentally affects other output results. To determine it, the numbers of marked points in all images were simply evaluated. It should be noted, however, that each student marked the images with different quality, detail and consistency. Globally it can be said that the resulting values should be real. Figure 5.8 shows a histogram with merged values in petitions. Thus, values 1-5 are combined into a value of 5, and for example 16-20 to 20.

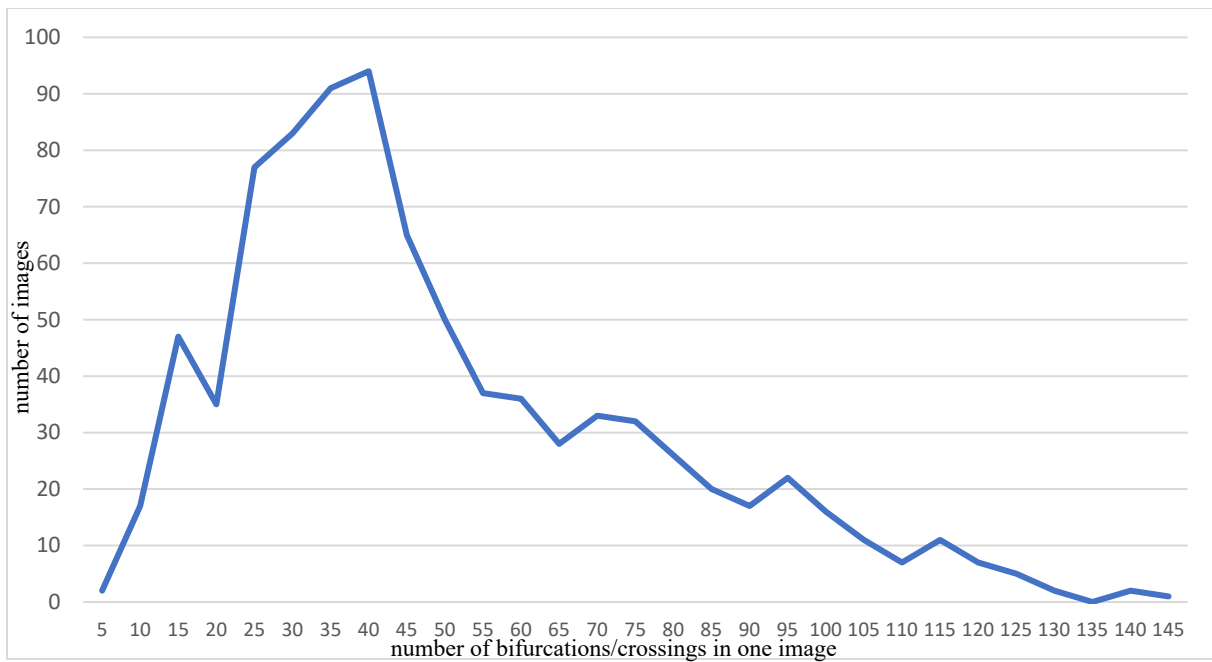


Figure 5.8: Number of images with a given number of bifurcations in one image (number  $n$ ) merged by petitions.

As can be seen in the Figure 5.8, the highest frequency value is at 40, and the calculation confirms this. The average value of the number  $n$  was calculated at 47.74, the median of the values is 40. In general, it can be assumed that students do not mark a point, overlook it or forget it, rather than mistakenly mark one. Therefore, we could calculate the value of the number  $n$  higher, but since we want to be rather stricter, we will choose the value 40 for further calculations.

## 5.7 Cropping of edges

SW<sub>4</sub> application was some kind of "drawing canvas" into which the individual retinas are inserted, with dimensions of 2,000×2,000 pixels. Since it was deliberately significantly larger to fit even very distant bifurcation from the center of the optic disc when converting from polar coordinates, a large part of it is empty as a result.

Figure 5.9 shows how many points are in total in the individual rows and columns of the field showed in Figure 5.5. The sums of bifurcation in the rows are marked in orange, the sums of bifurcation in the columns in blue. It can be seen that the vast majority of points is in the range of approximately 0-650, respectively 0-550. However, some points were recalculated to the value about 1,250. The orange histogram shows a decrease in the number of bifurcations and crossings in the area of the blind and yellow spot, i.e. in the graph in the middle of the more important area. This, although less noticeable decrease, is also seen in the blue values at the end of the main line. This is an optic disc and subsequent regrowth for the temporal major vessels in the retina. It can also be seen that the points are more distributed between the columns than rows. This is due to the aspect ratio in the images. Most of them are landscape oriented.

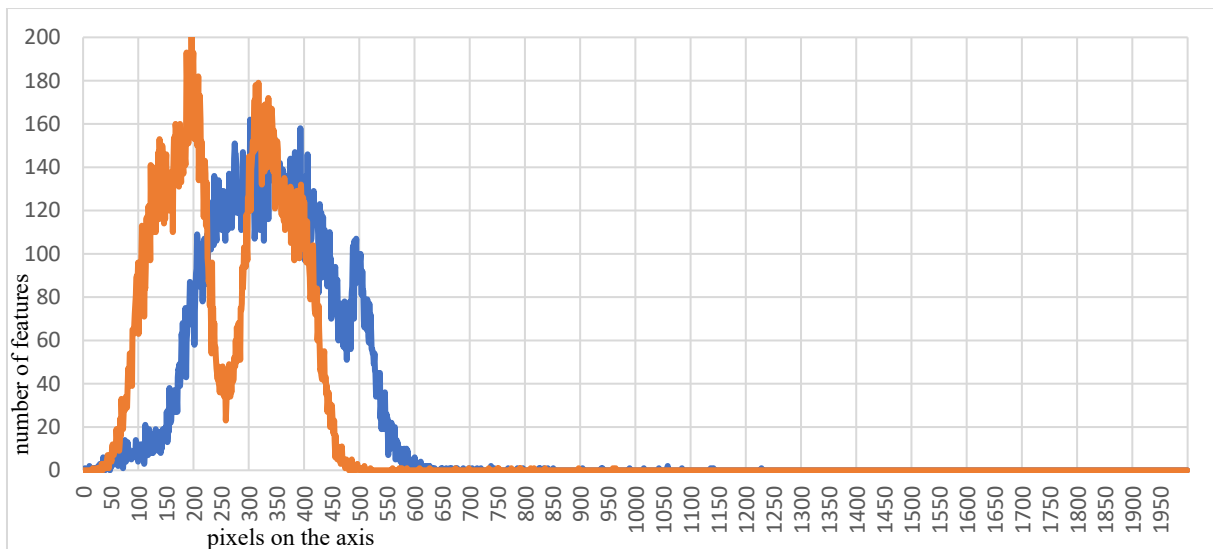


Figure 5.9: Sum of the number of bifurcations in columns (blue) and rows (orange) in Figure 5.5.

### 5.7.1 Rectangular cropping of edges

The first way to find effective margins in a Figure 5.9 is only a basic one-dimensional way. The histogram values are scanned sequentially in the direction from both ends and checking the moment when the set value is exceeded. If we then continued to work with an array of such truncated rectangles, we would use the specified number of pixels.

Table 5.5: Location of the first limit excess from left and right of the histogram. The x axis of the original image is blue in the Figure 5.9, the y axis is orange.

Limit	X left	Y left	X right	Y right	X area	Y area	Pixels
1	4	18	1,230	966	1,227	949	1,164,423
2	12	34	1,060	511	1,049	478	501,422
3	31	34	613	498	583	465	271,095
4	37	43	613	488	577	446	257,342
5	37	44	602	488	566	445	251,870
6	37	45	602	471	566	427	241,682
7	61	45	589	470	529	426	225,354
8	67	53	589	470	523	418	218,614
9	67	53	589	470	523	418	218,614
10	67	53	587	470	521	418	217,778

If we calculated the percentage of bifurcations from the total number instead of the absolute number of bifurcations, the result would be according to the Table 5.5. However, it should be emphasized that the limit values are for a single search and are therefore cut off four times their amount, reduced by the points that make up the intersection of multiple areas.

The ideal value seems to be a standard deviation of around 5%. If we take into account the cut from each of the four sides and the overlaps of the values with each other, at the limit of 1%, the cut will be almost 4%.

Table 5.6: Same as Table 5.5 with a limit in percent of the total number of bifurcations.

Limit	X left	Y left	X right	Y right	X area	Y area	Points
0.10 %	43	45	629	486	587	442	259,454
0.25 %	62	54	595	467	534	414	221,076
0.50 %	79	62	576	455	498	394	196,212
1 %	103	73	558	446	456	374	170,544
2 %	138	84	539	435	402	352	141,504
5 %	180	102	515	416	336	315	105,840
10 %	207	122	491	396	285	275	78,375

## 5.7.2 Circular cropping of edges

The second way to select the effective area is to cut with a circle. For these purposes, it was first necessary to determine the center of gravity of the bifurcations in the summary image of all retinal points. This was done with the usual weighted average number of bifurcations in pixels on both axes shown in the Figure 5.9. The center of gravity was calculated in the internal coordinate system to the position [341; 257]. If the center of gravity of some other sets of images was determined, it was always very similar, up to a maximum distance of 10 pixels. The center of gravity is marked in the Figure 5.10.

A circle was drawn from the determined center of gravity, and according to the standard formula for the distance of two points in two-dimensional space, it was determined how many bifurcations are inside and how many bifurcation points would be removed beyond the circle. The resulting values for some circle radius in pixels are shown in the following Table 5.7. There is the number of removed bifurcations, the percentage to the total number of marked bifurcations, how many pixels remained in the original matrix inside the circle and how many pixels would be according to the ideal join of the field according to the previous chapter.

Table 5.7: The number of dropped bifurcations after cropping with the specified circle radius and the number of resulting pixels within the circle.

Radius	Remove bif.	Ratio	Pixels	Join 5x5
150	19,085	43.78 %	70,677	2,827
160	15,447	35.44 %	80,377	3,215
170	12,023	27.58 %	90,781	3,631
180	8,994	20.63 %	101,761	4,070
190	6,560	15.05 %	113,365	4,535
200	4,748	10.89 %	125,625	5,025
210	3,499	8.03 %	138,501	5,540
215	2,937	6.74 %	145,185	5,807
220	2,505	5.75 %	152,009	6,080
225	2,156	4.95 %	159,029	6,361
230	1,838	4.22 %	166,205	6,648
235	1,585	3.64 %	173,481	6,939

The ideal crop of points is 5% of the total, which is according to the Table 5.7, when drawing a circle with a radius of 225 pixels. This is shown in the Figure 5.10.

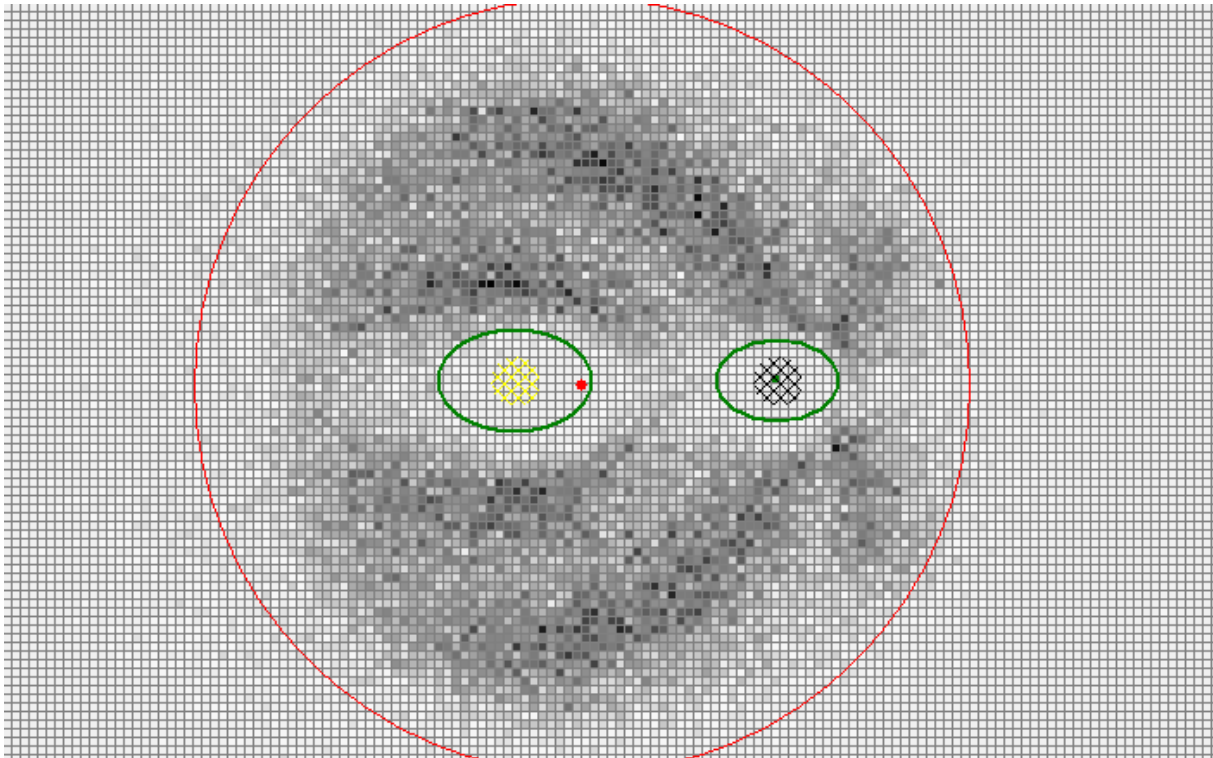


Figure 5.10: An image with merged  $5 \times 5$  pixels, marked center of gravity (red dot), a (red) circle with a radius of 225 (original) pixels, green ellipses marks areas with minimal amount of bifurcations and crossings around fovea (yellow) and optic disc (black).

## 5.8 Results from synthetic retinas

In the same way as in the previous chapter, we evaluated the images created from the synthetic retina generator described in Chapter 4.1. First, we processed the images using the SW<sub>2</sub> program (Chapter 5.4.2) and saved the found points according to our coordinate system. Using another program (SW<sub>4</sub>, Chapter 5.4.4), we then displayed the locations of bifurcations from all images into one image.

### 5.8.1 Testing

We are now comparing the created synthetic retinal images with our ground truth. We use manually marked real retinal images to create a density map, where there are the most bifurcation and crossing points. Using the same procedure, we want to automatically create a density map for synthetic retinal images and compare both results.

Using the application, 1,000 images were generated in which the crossings and bifurcation were found. The occurrence frequencies were graphically represented, and the result could be seen in Figure 5.11. It was then possible to visually compare the results of synthetic and real retinal images.

Figure 5.10 and Figure 5.11 shows the summarized occurrences of crossings and bifurcations for real and synthetic retinal images. First picture is marked manually, and second picture is marked

automatically. Both pictures are made up of about a thousand retinas. Although the application generates blood vessels in the synthetic retina symmetrically, some similarities with the summation from the real retina can be traced.

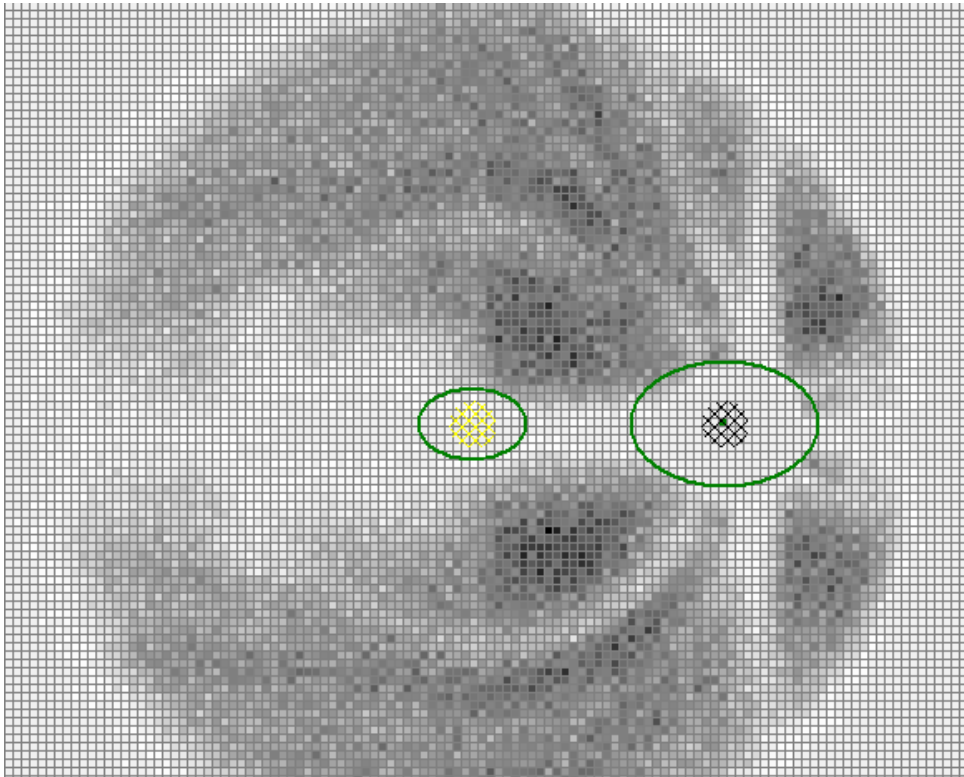


Figure 5.11: Density occurrence of summarized synthetically generated retinas, green ellipses is areas with minimal amounts of features.

The application of synthetic retinas is composed only from basic algorithms. As a result, there could be regular shapes seen on Figure 5.11. We assume that, based on real retinas research, we can better specify the distribution of crossings and bifurcations in the model.

### 5.8.2 Statistical treatment

In total, we obtained 1,000 images of synthetic retinas with the program. The auto-tagging program created 999 usable lists of bifurcation points. The program removed 2,793 points because they were inside a optic disc. 204,218 points were obtained.

The next same step as for manually marked retinas was to determine the smallest distance two points among each other and their resolution (see Chapter 5.5). After conversion from polar to Cartesian coordinates, there was no situation where two bifurcations in one retina belong to the same pixel, even with automatically marked points. In two adjacent pixels, it was only in one case. With the difference of two pixels then in five cases. All situations are displayed in the Table 5.8 again.

In Table 5.4 compared with Table 5.8 shows that although it has slightly higher numbers in absolute values. Algorithm of synthetic retinas vascular bed formation have too high branching, and therefore there are several times more points in the Table 5.8.

Table 5.8: The number of bifurcations with the specified distance in pixels and the maximum number of bifurcations in the new pixel after merging the specified areas.

Distance	Points	Ratio	Join	Max
0	0	0.0000 %	1×1	9
1	1	0.0000 %	2×2	19
2	5	0.0000 %	3×3	36
3	40	0.0002 %	4×4	54
4	205	0.0010 %	5×5	80
5	837	0.0041 %	6×6	101
6	2,962	0.0145 %	7×7	136

This chapter was presented the results of statistical analysis of bifurcation and crossing points in retinal images. The resulting density map shows different probabilities in the image areas according to the shades of grey. This information will be further used in calculating the amount of biometric entropy. The tool created in Chapter 0 has been tested for how diverse images it produces. However, after analyzing 1,000 images, it was found that the positions of the points are symmetrical and repeat in similar areas. Several procedures have been mentioned to suggest improvements to the entire synthetic retina formation system. Their mathematical values and regularities were also mentioned. In the following sections, the correctness of manual and automatic point detection was verified. Their deviation was 4.93 pixels on average. Independently, it has been found that mentioned detectors are not able to distinguish two crossings or bifurcations at a distance of less than 5 pixels. Therefore, it is fine if the raster for the point array is limited to 5×5 pixels in further calculations. Finally, the ideal field size for crossing and bifurcation points was quantified and the number of these points in all images was statistically analyzed. The effective area of the retinal image has a radius of 225 pixels and the median number of points is 40.

# 6 Theoretic enumeration of biometric entropy in retina

Another major task is to express the properties of the retina in a mathematical formula. Into a formula that can quantify how many various retinas can be distinguished in a set scheme. First, we will express only the basic limits of the retina, gradually we will incorporate the statistical properties and values into them, and finally we will try to quantify the entropy value in the retina.

## 6.1 General principle of theoretical quantification

In our first computation, principle of the retina on biometric entropy is performed in several ways, similar to fingerprints. We studied every pixel of the retinal image and checked whether there can be a split point of the vessels (bifurcation), visual crossing of two vessels or their termination (end point). Theoretically, we could say that it can occur anywhere in each pixel. As we know from images and physics of the retinal blood vessels, it is not possible practically. Therefore, if we assume that in one pixel a bifurcation or crossing occurs, the next bifurcation/crossing cannot be located in its close surroundings. Using this assumption, we can predict total number of biometric features in one particular retinal image. For each occurrence, we remember its properties (position in the image, the angle of the blood vessels, the biometric features type and the thickness of the blood vessels).

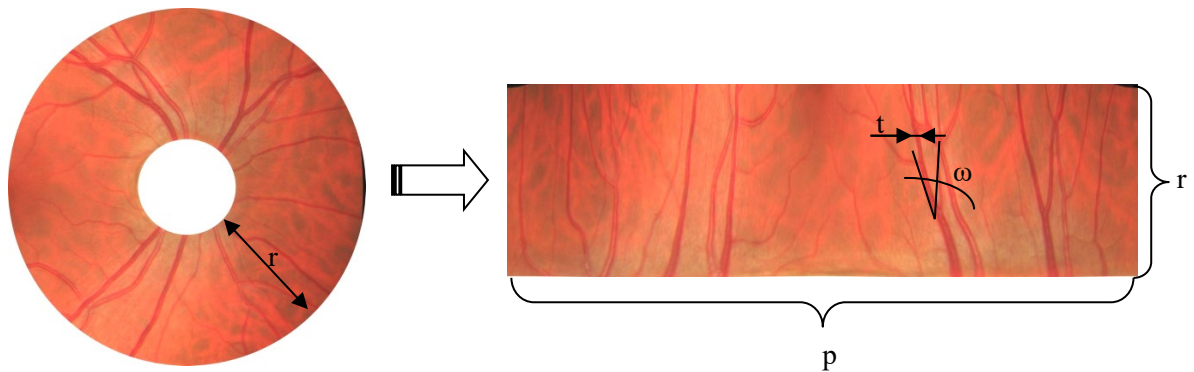


Figure 6.1: Retina feature description and illustration of transformation to polar coordinates.

Practical calculation of the entropy from properties of the eye is similar to the theoretical way. It is needed to find out the average occurrence of features in the retina. That means bifurcations, vessels crossing and terminations. It will also depend on the image resolution and the quality of imaging systems. For demonstration, see Figure 6.1 – the symbols here are used in Equation (6.1) below.

The variable  $n$  is an average count of biometric features locations, which is given by coordinates in the polar coordinate system  $(r, \theta)$ . Next step is to determine the angle  $\omega$  of each vessel. Very often, there are two angles very similar and in the same direction from the optic disc. In Equation (6.1) below,

it is symbolized by a variable indicating a number of different angles representing all the vessels. We are also interested in the total annulus area, which depends on the resolution. Finally, we used the thickness of the major and branching blood vessels. The width  $t$  of maximal thickness of the vessels could be approximately one tenth of the width of the ring segments. Approximate theoretical amount  $\Psi$  in all combinations of crossing vessels will be:

$$\Psi = \binom{p \cdot r}{n} \cdot \binom{\omega}{3} \cdot \binom{t+1}{2} \quad (6.1)$$

where  $p$  is resolution (width) of pixels,  $r$  is radius original retina in pixels before expand or height of expanded image. It can be assumed that in certain parts of the image there will not appear any biometric feature. Then, the equation can be improved by including interesting parts of the image only.

### 6.1.1 Experimental calculation of the formula

In the first naive localization of biometric features we analyzed 10 images from High-Resolution Fundus (HRF) Image Database [106]. The resolution of the pictures is 3,504×2,336 pixels. Total number of all the biometric features was 440. Average number of biometric features in one image was approximately 15. Then we have calculated percentage representation of each particular feature.

For biometric features finding, we have used expanded area around the optic disc bounded by circle with the center in the optic disc and with radius of distance between the optic disc and the fovea. We have been looking for these features:

- Type of branching of the vessels – we consider  $Y$ ,  $X$  and  $T$  like shapes of branching.
- Width of the branching vessels – when branching, both of the vessels widths are approximately the same (typically bifurcation at the end of the vessel) or different (typically when branching of the main vessel running from the optic disc).
- Number of biometric features in the sectors of a circle placed in the center of optic disc – the bounding circle was divided into six sectors (see Figure 6.2).



Figure 6.2: Iris and retina biometric features finding.

Based on the hypothesis it was found the approximate amount of some variables from equation. For basic finding on the sample approximately 20 images of retinas, there was manually determined amount crossings and bifurcation vessels. The results are in the following Table 6.1.

As can be seen in Table 6.1, at least two of branching vessels have the same width in 66 % occurrences. Instead of branching, the crossing vessel was in every fourth biometric feature. Surprising is a number

of perpendicular vessels in 39 % cases. It occurs especially when very thin capillary vessel split from a main vessel. Another validated though is biometric features occurrence in the directions from the optic disc. In the sector 1, there was 10 % of occurrences and in opposite sector only 7 %. Thus, the number of 83 % biometric features was in the rest of upper and lower sectors. It follows that in our entropy equation we could exclude biometric features, which are in some directions from the center of optic disc and calculate with two values of vessel width only. The branching type is invariable; it was not proven that, e.g. T branching, is less frequent than any other.

Table 6.1: Percentage representation of the biometric features.

Branching type			Width		In sector					
Y	X	T	same	diff.	1	2	3	4	5	6
36 %	25 %	39 %	66 %	34 %	10 %	22 %	18 %	7 %	21 %	22 %

Experimental calculation of entropy according to Eq. (6.1) was done afterwards. The resolution of our region of interest is approximately 720×120 pixels. Average number of biometric features is 15, maximal width of vessel is approx. 40 pixels. Number of possible angles of the vessels is 60.

$$\psi = \binom{p \cdot r}{n} \cdot \binom{\omega}{3} \cdot \binom{t+1}{2} = \binom{720 \cdot 120}{15} \cdot \binom{60}{3} \cdot \binom{40+1}{2} = 2.3 \cdot 10^{69} \quad (6.2)$$

According to Eq. (6.2) the number of possible combinations is  $2.3 \cdot 10^{69}$ . The parameters can vary depending on various conditions. For example, in the ROI of one-quarter size is the number of combinations  $2.1 \cdot 10^{60}$ . Of course, our calculation can be applied to any type of biometric feature.

### 6.1.2 Automatic finding

In the second solution, we focused on automatic finding of biometric feature purposes using two small databases. Gold Standard Database [27] for evaluation of fundus image segmentation algorithms with 45 images and Database Drive [43] with 40 images.

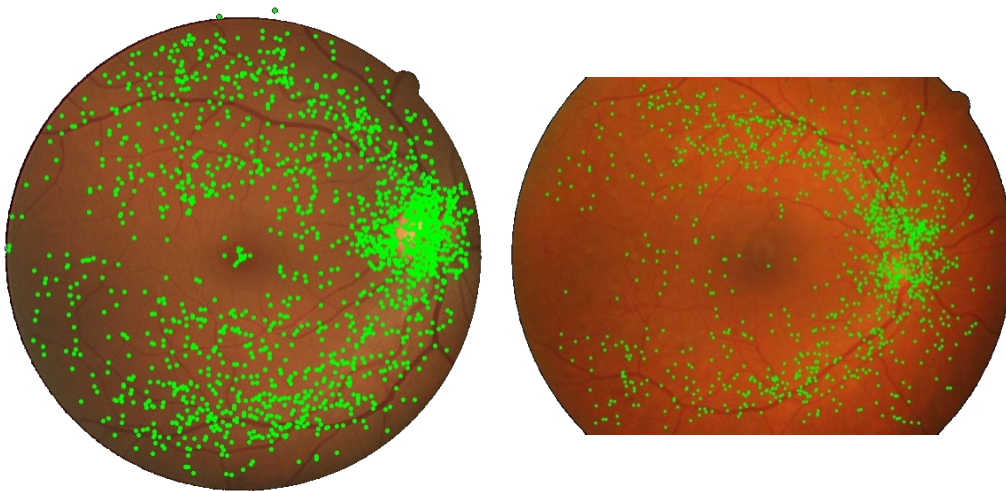


Figure 6.3: Results of biometric features localization in database drive (left) and gold (right).

Firstly, the application finds optic disc and fovea. Then, it tries to detect biometric features locations on image. Position of biometric features is written as an angle from the direction of the optic discs to the fovea and distance in multiples of lengths between optic disc and fovea. Half of the image was horizontally inverted so that the optic disc occurred always on the same side. Points from all retinas were combined into a single picture.

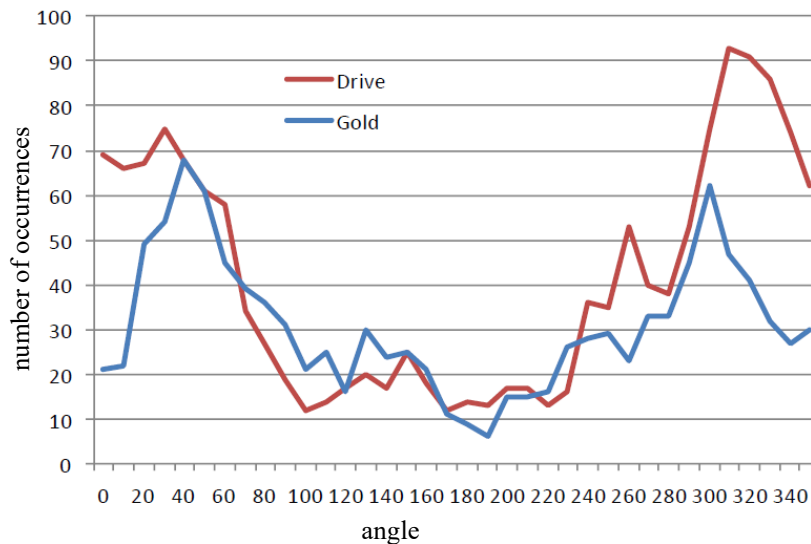


Figure 6.4: Number of occurrences by position around optic disc.

## 6.2 Theoretical formula

In further research, we deal with the frequency of occurrences in the usual area of the entire retinal image. The procedure for obtaining statistical information was presented in the previous chapters, now we are trying to write a formula that would clearly describe the procedure and its parameters. The presented theoretical formula has the disadvantage that it takes into account even very unlikely combinations of occurrences of bifurcations or crossings, which practically cannot occur in real retinas. Therefore, we quantified the probabilities of occurrence so that we can now approximate the calculation to the real retinas.

The first source of data is the probabilistic distribution of areas in which bifurcations occur relative to the position in the retina. We will work with Figure 5.10, in which, according to the bifurcation analysis, they are always connected from  $5 \times 5$  areas to one pixel. The pixels in the width correspond to the horizontal series of probabilities of the matrix  $R$  and has  $x$  values/pixels, and the vertical amount of pixels in the image corresponds to the vertical series of probabilities of the matrix  $R$  and has  $y$  values/pixels. Values into individual pixels are from 0 to  $n$ , where  $n$  is the maximal value on this resolution, according to the Table 5.4. Zero (on image white pixel) means no bifurcation in this place in all examined retinas, maximum value (on image black pixel) means that this point has the most points in the retinas. However, it is still a fraction of all the retinas examined. The other values are graduated

and displayed in the appropriate shade in the image. In the formula, we calculate the probability of individual points, therefore we convert these frequencies into probabilities according to the formula

$$p_{i,j} = \frac{b_{i,j}}{b_a} \quad (6.3)$$

where  $b_{i,j}$  is the number of bifurcations in a pixel at coordinates  $[i, j]$  in the summary image;  $b_a$  is the total number of bifurcations (the probabilities are not completely independent, but we will assume this for simplicity);  $p_{i,j} \in \langle 0,1 \rangle$  is the probability at position  $[i, j]$ , where  $i \in \{1, \dots, x\}$  and  $j \in \{1, \dots, y\}$ . Since the grayscale image is two-dimensional, we convert the probabilities to a probability matrix  $R$ , which is defined as follows:

$$R = \begin{bmatrix} p_{1,1} & \cdots & p_{x,1} \\ \vdots & \ddots & \vdots \\ p_{y,1} & \cdots & p_{x,y} \end{bmatrix} \quad (6.4)$$

According to statistical research, specific values of  $x$  and  $y$  are determined in several variants in the following Table 6.2. The minimum value is the dimension of the matrix at which the overall calculation still gives usable values in biometrics. We consider the combined  $5 \times 5$  field to be the optimal solution with respect to the previous statistical finding. The dimension without merging is for the original field. Our current calculations work with 1-megapixel images, but if we used retinal images at the highest possible resolution and did not use pixel joins, the result would be previously mentioned. However, it should be noted that the results are unlikely to increase in direct proportion to the increasing image resolution of the same retinal area.

Table 6.2: Possible resolution limits for relevant results.

	x	y
<b>Minimum</b>	~50	~40
<b>Join <math>5 \times 5</math> (optimal)</b>	92	75
<b>Original array</b>	456	374
<b>Maximal resolution</b>	by camera	

Since the positions of the probabilities have no meaning in the two-dimensional matrix, we can therefore convert it to a set. We convert the matrix  $R$  to the matrix  $D$  according to the function:

$$D = f(R) \quad (6.5)$$

wherein the function  $f()$  inserts individual rows from the matrix  $R$  one behind the other into a concatenated list according to the following scheme:

$$D = \{p_{1,1}, \dots, p_{x,1}, p_{2,1}, \dots, p_{2,x}, \dots, p_{y,1}, \dots, p_{x,y}\} = \{p_1, p_2, \dots, p_{(l-1)}, p_l\} \quad (6.6)$$

where  $l = (x \cdot y)$ , thus, the value  $l$  goes through all values of the matrix  $R$  and they generate a concatenated list  $D$ . Now we need to create sets of  $k$ -tuples that represent individual bifurcations in one retina. If we generate all the sets, we find out how many possible retinas can be created. Value  $k$  should be chosen according to the Gaussian distribution, as shown on Figure 5.8. We again use the mean

value for simplicity. Total number of combinations of arbitrary values  $k$  in this concatenated list  $D$  applies formula:

$$K = \binom{x \cdot y}{k} = \binom{|D|}{k} \quad (6.7)$$

Multiplication  $x \cdot y$  indicates the number of pixels/values in the list  $D$ , so we can write  $x \cdot y = |D|$ , where  $|D|$  indicates the length of list  $D$ . The number  $k$  indicates the number of intersections that occur in list in list  $D$  or matrix  $R$ . We count this value in Chapter 5.6 at 40 bifurcations. A large number of zero values will be truncated using the effective area of the circle. However, the field is still very sparse. In our statistically evaluated images, zero values contain 124,299 points, i.e. 78%. A large number of zero values can be caused by rounding and small sample of values. This is despite the fact that all position values of points in polar coordinates are stored with an accuracy of at least four decimal places. Reduce zero probabilities in the list  $D$ , i.e. the values  $p_i = 0$  is done as follows:

$$D' = \{p'_l | p'_l \in D \wedge p'_l > 0, l \in \{1, \dots, (x \cdot y)\}\} \quad (6.8)$$

Therefore, there remained in our calculated model 34,730 points at all. If the points are joined, there will not be so many reduced pixels.

Hereby we create a new set  $D'$ , which contains only non-zero probabilities of crossings. By a simple calculation, we then calculate the number of combinations of arbitrary  $k$  values of all crossings with a non-zero probability of occurrence in the set  $D'$  as follows:

$$K' = \binom{|D'|}{k} \quad (6.9)$$

where  $|D'|$  corresponds to the length of the list  $D'$ .

The last step is to reduce the sums of the probabilities of  $k$ -tuple (i.e. selected crossing positions with a non-zero probability of occurrence for all conceivable combinations), where the average value of all probabilities of crossing in this  $k$ -tuple corresponds to the average probability  $p_{avg}$  with tolerance  $\varepsilon$ .

The following applies:

$$p_{avg} = \frac{\sum_{l=1}^{|D'|} p'_l}{|D'|}, p'_l \in D' \quad (6.10)$$

wherein  $p_{avg}$  is the average value of all crossings occurrence probabilities in the set  $D'$ , i.e. non-zero crossings occurrences probabilities from  $D$ , or  $R$ . Finally, we need to find out whether the set of generated points in the retina is really possible. That is, the total probability of all points is approximately equal to the average probability with a given number  $k$ . We further define:

$$z_s = \{z_1, \dots, z_k\}_s \in V \quad (6.11)$$

$$V = \left[ \binom{|D'|}{k} \right] \quad (6.12)$$

$$s \in \{1, \dots, K'\} \quad (6.13)$$

where  $z_s$  contains all possible  $k$ -tuples of all possible combinations, which corresponds to  $V$  (special operator  $]x[$  defines the operation of creating all these possible  $k$ -tuple into the set  $z_s$ ).  $s$  then denotes a selection from the number of all combinations of  $D'$  with non-zero crossing probabilities. Then we calculate the average probability of a given  $k$ -tuple from the total number with as follows:

$$p_{avg-z_s} = \frac{\sum_{z_i \in z_s} p'_{z_i}}{k}, p'_{z_i} \in D' \quad (6.14)$$

Then we can write:

$$D'' = \{p_{avg-z_s} \mid p_{avg-z_s} \geq (p_{avg} - \varepsilon), z_s \in V\} \quad (6.15)$$

The value  $\varepsilon$  is a tolerance that we choose experimentally to tolerate a reasonably lower number of the average probability  $k$ -tuple.

In conclusion, it can be written that the number of elements in the set  $D''$  is the number we are looking for, which is

$$K'' = |D''| \quad (6.16)$$

We only generate a formula for one (median) value of  $k$ . We should correctly create combinations with a lower and higher value of  $k$ . This would increase the resulting biometric entropy. For now, we only need a calculation with an average value of  $k$ .



# 7 Practical enumeration of the formula

In order to be able to calculate the value of entropy according to the created formula, we need an unimaginably powerful computer that cannot even exist. Therefore, it is necessary to simplify and optimize the entire calculation. The first and simplest step is to reduce the resolution of the field, i.e. to merge the pixels into squares. In Table 5.7, we found that 159,029 points remain after the circular crop. If we connect them in  $5 \times 5$  areas, the result will be 6,362 pixels. For the mean value of  $n = 40$  bifurcations in the retina, the combination of 6,362 over 40 is  $1.5 \cdot 10^{104}$  combinations. If we join  $10 \times 10$  areas, the result will be 1,591 points, which is still a large  $8.5 \cdot 10^{79}$  combinations. It is therefore necessary to find another way to simplify the calculation.

## 7.1 Computing algorithms

We have created several applications to quantify the amount of biometric entropy. Because a specific value is impossible to determine, we at least wanted to estimate required time.

### 7.1.1 Program in Matlab

The first of the introduced programs is written in Matlab. We chose it because of its speed and the possibility of dividing the calculation into multiple threads. Unfortunately, we found that the generated array of combinations is too large for memory space. A variant in which this procedure could be applied is the sequential evaluation of the combinations array. This is not an insurmountable obstacle, but our settings did not allow it. The calculation procedure is as follows:

$$D'' = \text{sum}(\text{combntns}(D', k), 2) \quad (7.1)$$

Function *combntns* generates individual combinations of  $k$ -tuples over a set  $D'$ . This creates a list of sets with individual probabilities. We sum the probabilities in one set via the sum function with the value of the second parameter 2. This creates only a list of probabilities in the individual retinas. Finally, we find out whether the given element of the set is within the range of the average probability  $s \pm \varepsilon$ :

$$\text{sum}(\text{and}(D'' > p_{avg} \cdot k - \varepsilon, D'' < p_{avg} \cdot k + \varepsilon)) \quad (7.2)$$

The *and* function only returns the values 1 or 0, so it is enough to use the sum to find out the number of real combinations.

### 7.1.2 Program in C language

Another program was created in C language due to the speed of this language. The SW<sub>4</sub> program (Chapter 5.4.4) converts the points of all marked retinas from polar to Cartesian coordinates and joins all positions together. This resulting field is then converted to a file. The new program then processes

this file. The C program allows connecting points in squares of a specified size, as described earlier. The program works only in the console, but to check the correct connection, it allows viewing a graph of the merged field.

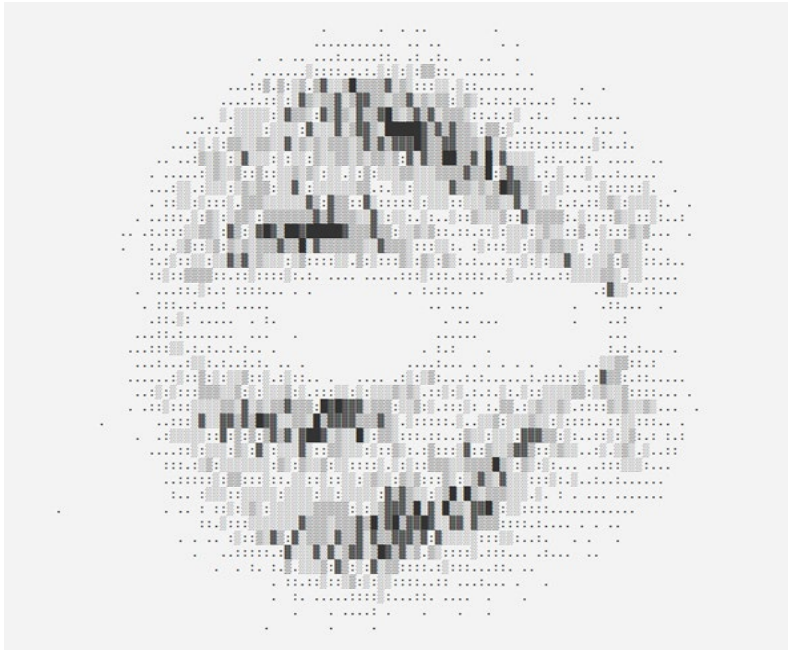


Figure 7.1: Showing of bifurcation frequencies of merged fields in C program.

The program works with either the original or a reduced field. It allows setting how many elements will be combined, and also sets an average probability limit. Finally, it displays a summary approximate graph (shown on Figure 7.2) with the result.

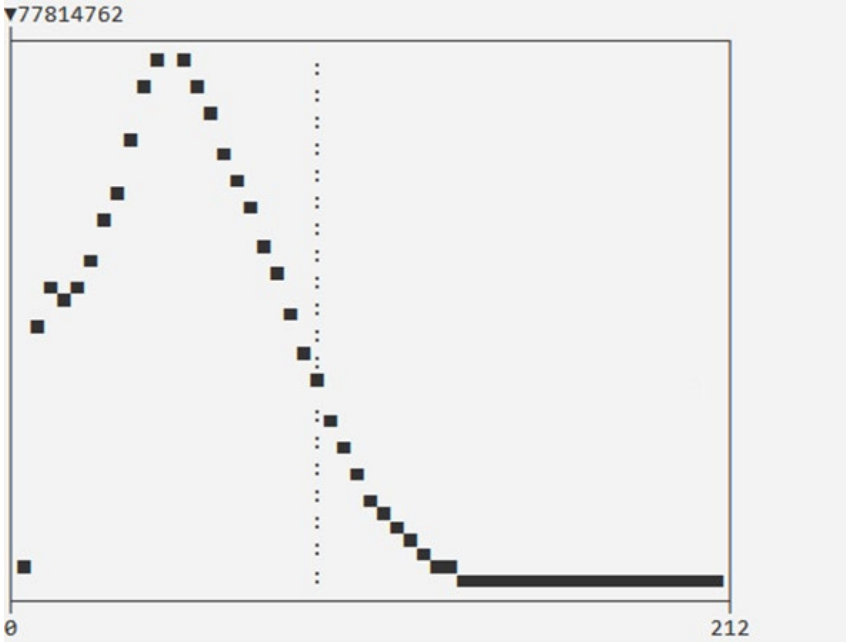


Figure 7.2: The resulting histogram of the sum of probabilities in  $k$ -tuples. The  $x$ -axis is the sum of the probabilities (in adjusted units), the  $y$ -axis is the number of  $k$ -tuples regards to the given group of sums.

The speed of the program on a computer with a processor with an average frequency of 3.9 GHz was first tested to calculate the sums of fours ( $k = 4$ ). In 255 minutes, the program processed 105.6 bil.

combinations (422.4 bil. steps). That's about 25 billion results per hour, or 6.9 million per second. In the 40-tuples calculation test, the calculation times were as follows. In 90 minutes, the program processed 5.9 bil. combinations (237 bil. steps). So about 4 billion per hour, or 1.1 million per second, respectively. It follows that in a non-optimized point generation proposal, it would in no way be possible to evaluate all these combinations, as Table 7.1 shows.

## 7.2 Simplification of the calculation

Since the quantification is really very difficult, we returned to the idea of simplifying the calculation. Unfortunately, we have found out that most of the following procedures are not mathematically possible. To understand these principles, we present these procedures.

### 7.2.1 Field raster reduction

The first method is to reduce the number of points from which the combinations will be calculated. As already written, we found that the optimal connection of points is on a grid of 5×5 pixels. At that point, we can work with each new pixel as one option where the bifurcation/crossing point can be used. If we merge areas in larger squares, we must already take into account that some new pixels may fit more than one point. However, this procedure does not lead to full results. Table 7.1 shows the number of combinations and approximate calculation times on a standard computer. These, we suppose, need no comment.

*Table 7.1: Time-consuming of calculation for the specified join on a classical computer.*

Join	Pixels	Combinations	Computing time
1×1	159,029	$1,3973 \cdot 10^{160}$	$4.00 \cdot 10^{146}$ years
5×5	6,361	$1,4997 \cdot 10^{104}$	$4.28 \cdot 10^{90}$ years
10×10	1,590	$8,4997 \cdot 10^{79}$	$2.42 \cdot 10^{66}$ years
20×20	397	$1,4352 \cdot 10^{55}$	$4.09 \cdot 10^{41}$ years

### 7.2.2 Retinal symmetry

A partial simplification could be to consider the fact that the retina is seemingly symmetrical along the  $x$ -axis. Therefore, we can generate combinations of half points on half the number of pixels. Subsequently, there must be a reverse phase, when all combinations from both fields are combined so that the number of bifurcation points is full again.

### 7.2.3 Division into regular clusters

The possibility of connecting areas in clusters seems to be based on a similar principle. First, we divide the retina into individual parts. We have tried several possibilities, which will be described in the following text. In these areas, we calculate the average value of probabilities per combined number of

bifurcations. In other words, it will be the probability that during combinations we will select a pixel that belongs to a specific cluster. Then we work similarly, as mentioned earlier, with the difference of repeated possibility of intervention of the same cluster, i.e. in combination with repetition. However, it is a significantly reduced set of points (units, maximum low tens number of clusters), so the calculation is not very demanding. Then we will evaluate individual clusters, i.e. if an area has been selected, which point or which points are likely to be selected. The resulting combination number will then be determined by a combination over all processed areas, i.e. again in the principle of recombining all detected combinations, as described previously.

The first way to select clusters is to divide them into regular radial areas. The advantage of this division is the same size of all parts, the disadvantage is that the individual clusters pass through areas with very different probability frequencies. In some evaluation principles, however, this may not be a disadvantage. The division into individual regular sections and the frequency of occurrence of bifurcations in them is shown in Figure 7.3. There are also areas of various regular shapes in which there is only a minimum of bifurcations. It is therefore obvious that only a small percentage of the detected points occur in the sections closest to the x-axis.

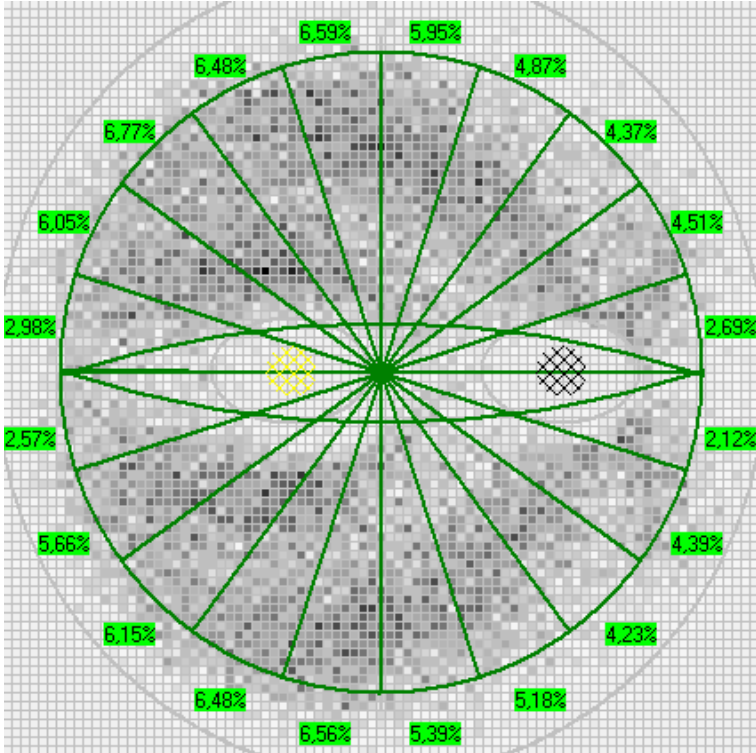


Figure 7.3: Division into radial clusters and percentage of all features in it..

### 7.2.4 Division into clusters according to probability

Another way is to create clusters over areas with a similarly high probability. The easiest way to describe it is to have regular areas, but since the areas will be converted to one-dimensional sets, we can choose any shape. These areas would replace individual probabilities to the aggregate probability of the entire cluster.

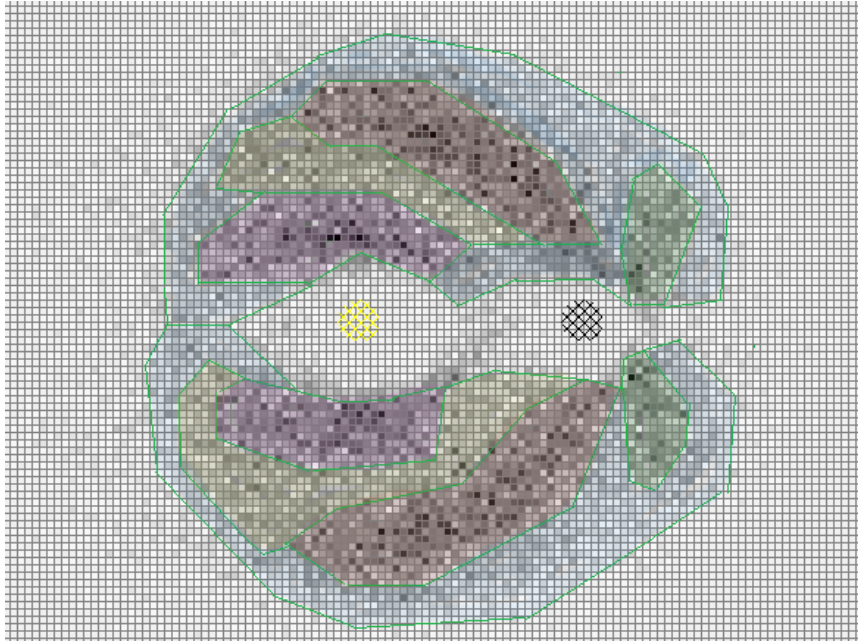


Figure 7.4: Division into clusters according to bifurcations/crossings probability.

In Figure 7.4, we roughly divided the probabilities into clusters according to their frequency. Clusters could be further reduced to a similar size. In each half of the retina, we selected two areas with the highest probability (red and purple), one area in the temporal part (green), one area between the main sections (yellow), and then the remaining areas with the least probability, but with the largest area – not yet marked areas (blue) and the rest of the retina (white). The next procedure would then be similar to the principle already described, individual aggregate probabilities of areas would be determined, combinations would be created, and after determining the points, the division in individual clusters would be considered.

### 7.2.5 Division into discontinuous areas with the same overall probability

As already written, the individual clusters are converted into a one-dimensional array, so it does not matter what the shape of the area will be. It shouldn't even matter if one cluster is divided into multiple partitions. Theoretically, we can divide it into individual pixels.

The procedure is as follows.

- We create individual almost identical clusters. We write all nonzero probabilities into the set. Their location is not necessary information, so we do not have to save it. We choose the number of clusters  $n$  on which we will divide the retina. We arrange the set and gradually assign points to clusters, which should contain almost the same points at the end of the division. For this reason, we do not have to write all clusters, but one universal one will suffice, in which we always write the median of the individual divided values.
- We compute the combinations over the individual clusters. Divide the average  $k$  occurrences of bifurcations/crossings in one retina (Chapter 5.6) by the number of clusters (ideally, they were chosen so that the division is without remainder). The resulting number is the number of combinations over

one cluster of  $c$  occurrences. Next, we enumerate all  $c$ -tuples over the universal cluster. According to the procedure in the theoretical formula (Chapter 6.2) we calculate the total probability of individual  $c$ -tuples. If the probability is higher or lower than the specified  $\varepsilon$ , we discard it. The value of  $\varepsilon$  should be  $n$  times higher as the tolerance decreased with the number of clusters. We now have an entropy value for one cluster.

- We need to obtain the total amount of entropy over all clusters. After the second step, we have a list of  $c$ -tuples with an average probability of occurrence ( $\pm \varepsilon$ ). Many combinations of probabilities will be repeated in the list, we will shrink the list and simplify the calculation by counting the combinations with repetition. We replace all  $c$ -tuples with the same probabilities by only one item in the list. The reduced list already shortens the length of the total entropy calculation. So now we combine the universal cluster  $n$  times, that is, if there were  $n$  clusters, we combine the partial results with each other.

## 7.3 Random choose

Random (or better manifold) selection became the final procedure, which took into account previous successful and unsuccessful ways. We thought that not all combinations that can be created can actually appear in the real retina. But with practical quantification we are not able to determine how many combinations do not pass the probability limit. Therefore, we will try to create combinations randomly and then we will find out on a sufficiently large sample which part meets the set limit. Due to the speed and the possibility of programming of anything code, we used a modified program in the C language (Chapter 7.1.2). Instead of sequential enumeration, the program now directly selected random 40-tuples, each quantifying the aggregate probability and determining if it is above the limit.

Application parameters: the loaded original field of merged bifurcations and crossings contains 490,000 pixels. The merged  $5 \times 5$  field, excluding zero points, contains 6,249 new pixels with a total of 41,419 bifurcations/crossings. The maximum value of the bifurcations/crossings number in one new pixel (i.e. how many times the bifurcation from the examined 888 retinas fit into this pixel) is 25. The amount of performed steps is 28.2 billion.

The application summed up the occurrence of bifurcations in randomly selected sets of 40 points (the inverse of the occurrences number divided by all points number is a probability). The maximum value of the sum is 388, the most common value of the sum is 219 (in 422 million cases). The results from the application are in the form of a Gaussian curve and are shown on Figure 7.5.

One bifurcation probability is  $\frac{1}{41,419} \cong 0.0024\%$ . According to the equation (6.9) in Chapter 6.2, it is an average value of one selected bifurcation or crossing for the most common resultant sum of the probabilities following  $p_{avg} = \frac{219}{41,419 \cdot 40} = 0.0132\%$ .

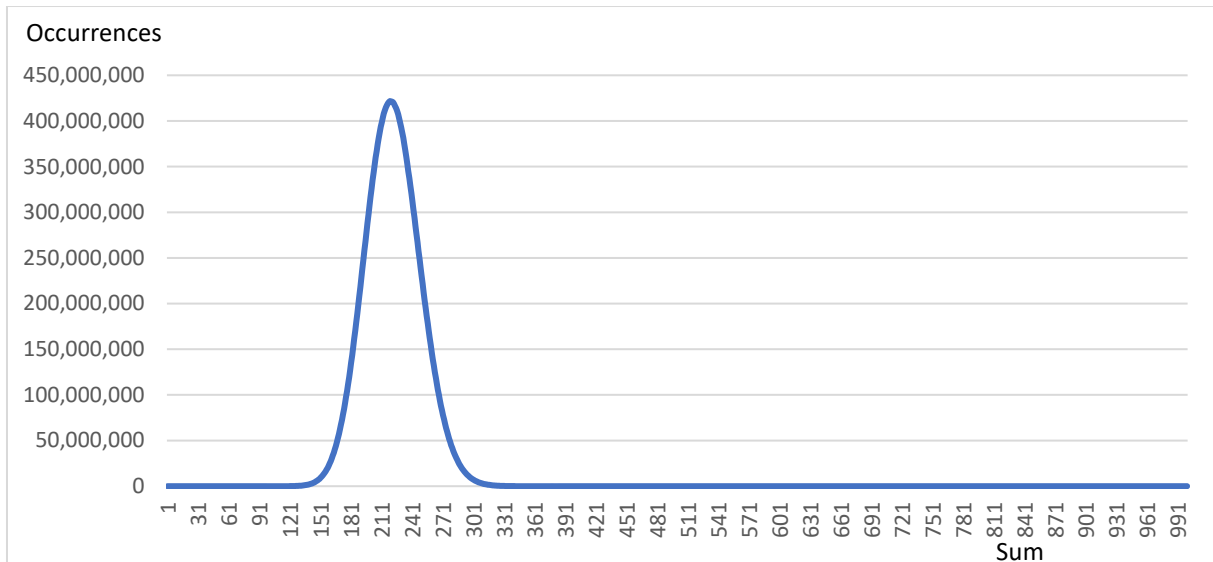


Figure 7.5: Histogram of 40-tuples of frequencies.

We therefore assume that we have taken a sufficient sample, and now apply a tolerance to all potentially generated combinations. Table 7.2 shows the resulting numbers for the different limit tolerance values. In the middle, there is the percentage of discarded 40-tuples.

Table 7.2: Biometric entropy value for different limit values.

Limit	Not discarded	Final
90	100,000%	$1,4997 \cdot 10^{104}$
120	99,999%	$1,4997 \cdot 10^{104}$
150	99,809%	$1,4968 \cdot 10^{104}$
180	94,750%	$1,4210 \cdot 10^{104}$
185	92,199%	$1,3827 \cdot 10^{104}$
190	88,846%	$1,3324 \cdot 10^{104}$
195	84,622%	$1,2691 \cdot 10^{104}$
200	79,518%	$1,1925 \cdot 10^{104}$
205	73,587%	$1,1036 \cdot 10^{104}$
210	66,956%	$1,0041 \cdot 10^{104}$
215	59,812%	$8,9700 \cdot 10^{103}$
220	52,390%	$7,8570 \cdot 10^{103}$
225	44,952%	$6,7415 \cdot 10^{103}$
230	37,742%	$5,6602 \cdot 10^{103}$
235	30,989%	$4,6474 \cdot 10^{103}$
240	24,874%	$3,7304 \cdot 10^{103}$
270	4,038%	$6,0559 \cdot 10^{102}$
300	0,275%	$4,1285 \cdot 10^{101}$
330	0,008%	$1,1959 \cdot 10^{100}$
360	0,000%	$1,5588 \cdot 10^{98}$

Thus, the resulting Table 7.2 states that in the described setting, it is possible to distinguish approximately  $1.4 \cdot 10^{104}$  by a combination of the distribution of the positions of the intersections by bifurcations or crossings.



## 8 Conclusion

In this work were introduced several topics. After a theoretical introduction, were described diseases that somehow visually affect the human eye retina. These diseases can significantly affect biometric identification, for example in access systems. Our research team works with ophthalmologists to help us identify diseases in images so that we can develop algorithms and applications like automatic retinal detection and recognition. This can often be crucial to the health of the person, which was photographed, especially if they do not yet know about their illness. In this work, we present several detection applications that achieve relatively good results. Doctors have already shown interest in some of them.

For the main goal of this work, it is important to identify individual points and areas in retinal images. In almost 900 pictures it was marked manually by our students, other applications were developed for further marking of points. The accuracy of this automated tag was checked against manually evaluated images.

A large database of images with a known location of detected points is needed to test the developed applications mentioned in the previous paragraph. However, such databases are not shared publicly, so the next chapter is devoted to the creation of a special graphics application for creating credible retinal images, in which we can simulate, for example, the manifestation of a disease. This application was created completely, from the background color to a credible vascular branching system. Another upgrade of this tool is a mathematical analysis of the method of bottling and branching of vessels in real images. This analysis tries to find out the laws that most often apply to the formation of blood vessels. The following chapters then present the main calculations concerning biometric entropy. The first is a statistical analysis of the points of branching and bifurcation of vessels, according to which our system recognizes the identity of people. The analysis determines in which parts of the retina these points occur more often and where less often. From these findings, a probability map was created, on which the second main chapter is based. In this chapter, a formula is mathematically determined that takes into account the probabilities of individual parts of the retina, and on this basis determines the biometric entropy of the retina. In the last chapter, previously determined values are inserted into the formula. However, the calculation of the exact biometric entropy would be very demanding, so practices to simplify the calculation were also introduced.

In the currently examined setting, i.e. image size  $450 \times 375$ , with the finding that the points of bifurcation and crossing do not repeat closer than 5 pixels, the biometric entropy can be set to 340 bits, which is sufficient to identify all people in the world.

The work provided a basic overview of the statistics of crossing points and bifurcations. These statistics were then converted into formula determinations and then approximate values were calculated for the

currently used images. There are, of course, more regularity and dependence on the physiological production of the bloodstream, we tried to introduce at least the basic ones.

The assignment of the dissertation work included a detailed research of the human eye retina biometric feature. Based on the experimental investigation were to be identified areas with a higher and lower probability of crossing and bifurcation of the vessels in the image. There should also be a discussion of how this probability and the possibility of biometric recognition can affect individual diseases manifesting on the retina. Based on probabilistic surveys were to be determined formulas for calculating biometric entropy, and then specific values were to be evaluated. All these dissertable points were analyzed and fulfilled in the work.

## 9 References

- [1] Barajas H.: *Atlas of the Human Eye: Anatomy & Biometrics*. Palibrio, 2015, ISBN 978-1506510330.
- [2] Snell R. S., Lemp M. A.: *Clinical Anatomy of the Eye*. Wiley-Blackwell, 2<sup>nd</sup> Edition, 2013, ISBN 978-0632043446.
- [3] Kazilek Ch., Cooper K.: *Rods and Cones*. Arizona State University School of Life Sciences, 2010, link: <https://askabiologist.asu.edu/rods-and-cones>, accessed on 2018-01-02.
- [4] Albert D. M., Miller J. W. et al.: *Principles and Practice of Ophthalmology*. Saunders Elsevier, 3<sup>rd</sup> Edition, 2008, ISBN 978-1416000167.
- [5] Ryan S. J. et al: *Retina*. Elsevier Mosby, 4<sup>th</sup> Edition, 2006, ISBN 978-0323043236.
- [6] American Diabetes Association: *Diagnosis and Classification of Diabetes Mellitus*. Diabetes Care, Issue 33, 2010: pp. 62–69, DOI 10.237/dc10-S062.
- [7] Albert D. M., Miller J. W., et al.: *Principles and Practice of Ophthalmology*. Saunders Elsevier, 3<sup>rd</sup> Edition, 2008, ISBN 978-1-4160-0016-7.
- [8] Scanlon P. H., Wilkinson C. P., Aldington S. J., Matthews D. R.: *A Practical Manual of Diabetic Retinopathy Management*. Wiley-Blackwell, 2009, ISBN 978-1405170352.
- [9] Sosna T.: *Diabetická retinopatie (Diabetic Retinopathy)*. Axonite CZ, 2<sup>nd</sup> Edition, 2016, ISBN 9788088046059.
- [10] Farzin H., Abrishami-Moghaddam H., Moin M. S.: *A Novel Retinal Identification System*. EURASIP, Journal of Advances in Signal Processing, Hindawi, Vol. 2008, p. 10, DOI 10.1155/2008/280635.
- [11] Cavallotti C. A. P., Cerulli L.: *Age-Related Changes of the Human Eye*. Humana Press, 2008, ISBN 978-1934115558.
- [12] Kolář P.: *Věkem podmíněná makulární degenerace (Aged-related macular degeneration)*. Grada, 1<sup>st</sup> Edition, 2008, ISBN 978-8024726052.
- [13] Kanski J. J.: *Clinical Ophthalmology – A Systematic Approach*. Elsevier, 6<sup>th</sup> Edition, 2007, ISBN 978-0080449692.
- [14] Ernest J.: *Makulární degenerace (Macular degeneration)*. Mladá fronta, 1<sup>st</sup> Edition, 2010, ISBN 978-8020423634.
- [15] *Vlhká forma s edémem (Wet form with edema)*. Mladá fronta, accessed on 2018-06-25, image from <https://img.mf.cz/062/617/c.jpg>.
- [16] Pašta J.: *Základy očního lékařství (Basics of ophthalmology)*. Charles University - Karolinum, 2017, ISBN 978-8024624600.
- [17] Tower P.: *The Fundus Oculi in Monozygotic Twins: Report of Six Pairs of Identical Twins*. AMA Arch Ophthalmology, No. 54, pp. 225-239, 1955.

- [18] Daugman J.: *How iris recognition works*. IEEE Transaction on Circuits and Systems for Video Technology, vol. 14, no. 1, pp. 21–30, 2004.
- [19] Jain A., Hong L., Pankanti S., Bolle R.: *An identity authentication system using fingerprints*. Proceedings of the IEEE, vol. 85, no. 9, pp. 2127–2134, 1997.
- [20] Tan X., Bhanu B.: *A robust two step approach for fingerprint identification*. Pattern Recognition Letters, vol. 24, pp. 2127–2134, 2003.
- [21] Ortega M., Mariño C., Penedo M., Blanco M., Gonzalez F.: *Personal authentication based on feature extraction and optica nerve location in digital retinal images*. WSEAS Transactions on Computers, vol. 5, no. 6, pp. 1169–1176, 2006.
- [22] Ortega M., Penedo M. G., Mariño C., Carreira M. J.: *Similarity Metrics Analysis for Feature Point Based Retinal Authentication*. Springer Berlin Heidelberg, 2008, pp. 1023–1032.
- [23] Mariño C., Penedo M. G., Carreira M. J., González F.: *Retinal Angiography Based Authentication*. Springer Berlin Heidelberg, 2003, pp. 306–313.
- [24] Jakobiec M. D., Frederic A.: *Ocular Anatomy, Embryology and Teratology*. Harpercollins, 1982, ISBN 978-0061413360.
- [25] Decencière E., Cazuguel G., Zhang X., Thibault G., Klein J. C., Meyer F., Marcotegui B., Quelled G., Lamard M., Danno R., Elie D., Massin P., Viktor Z., Erginay A., La B., Chabouis A.: *Teleophtha: Machine learning and image processing methods for teleophthalmology*. IRBM, Elsevier Masson, Vol. 34, No. 2, pp. 196–203, 2013.
- [26] Decencière E., Zhang X., Cazuguel G., Lay B., Cochener B., Trone C., Gain P., Ordonez R., Massin P., Erginay A., Charton B., Klein J. C.: *Feedback on a publicly distributed database: the messidor database*. Image Analysis & Stereology, Vol. 33, No. 3, pp. 231–234, 2014.
- [27] Kohler T., Budai A., Kraus M., Odstřilík J., Michelson G., Hornegger J.: *Automatic noreference quality assessment for retinal fundus images using vessel segmentation*. 26<sup>th</sup> IEEE International Symposium on Computer-Based Medical Systems, pp. 95–100, 2013.
- [28] Shih H. P.: *Two Algorithms for Maximum and Minimum Weighted Bipartite Matching*. Department of Computer Science and Information Engineering National Taiwan University, 2008.
- [29] Ortega M., Penedo M. G., Rouco J., Barreira N., Carreira M. J.: *Retinal ration using a feature points based biometric pattern*. EURASIP Journal on Advances in Signal Processing, vol. 2009, Article ID 235746, 13 pp., 2009.
- [30] Hájek J., Draňanský M.: *Biometric-Based Physical and Cybersecurity Systems: Recognition-Based on Eye Biometrics: Iris and Retina*. Springer International Publishing, 2019, p. 37-102.
- [31] Goh K. G., Hsu W., Lee M. L.: *An automatic diabetic retinal image screening system*. Medical Data Mining and Knowledge Discovery, Springer, Berlin, Germany, 2000.
- [32] Goodfellow I. J., Pouget-Abadie J., Mirza M., Xu B., Warde-Farley D., Ozair S., Courville A. C., Bengio Y.: *Generative Adversarial Networks*. CoRR, abs/1406.2661, 2014.

- [33] Radford A., Metz L., Chintala S.: *Unsupervised Representation Learning with Deep Convolutional Generative Adversarial Networks*. CoRR, abs/1511.06434, 2015.
- [34] Zamir M., Medeiros J. A., Cunningham T. K.: *Arterial bifurcations in the human retina*. The Journal of general physiology, Vol. 74, No. 4, 1979, pp. 537–548.
- [35] Source code: <https://github.com/Lukass2/RetinaFeatureVectorExtractor.git>
- [36] Purves E. D., Augustine G. J., Fitzpatrick D., Katz L. C., LaMantia A.-S., McNamara J. O., Williams S. M.: *Anatomical Distribution of Rods and Cones*. Neuroscience, 2<sup>nd</sup> edition, 2001.
- [37] Usher D., Tosa Y., Friedman M.: *Ocular Biometrics: Simultaneous Capture and Analysis of the Retina and Iris*. Advances in Biometrics Sensors, Algorithms and Systems, Springer Publishers, pp. 133-155, 2008.
- [38] Li S. Z., Jain A.: *Encyclopedia of Biometrics*. Springer Publishers, pp 273-274, 2009.
- [39] Drahanický M., Orság F., Doležel M. et al.: *Biometrie*. Computer Press, 2011.
- [40] Arakala A., Culpepper J. S., Jeffers J., Turpin A., Boztas S., Horadami K. J., McKendrick A. M.: *Entropy of the Retina Template*. ICB '09 Proceedings of the Third International Conference on Advances in Biometrics, pp. 1250–1259, 2009.
- [41] Timberlake G. T., Kennedy M.: *The Direct Ophthalmoscope – How it Works and How to Use it*. University of Kansas, 2005.
- [42] Goldstein I., Simon C.: *A New Scientific Method of Identification*. New York State Journal of Medicine, Vol. 35, 1935.
- [43] Staal J., Abramoff M., Niemeijer M.: *Ridge based vessel segmentation in color images of the retina*. IEEE Transactions on Medical Imaging, Vol. 23, No. 4, 2004, pp. 501–509.
- [44] *Vertical sagittal section of the adult human eye*. Webvision, accessed on 2017-02-14, image from: <http://webvision.med.utah.edu/imageswv/sagitta2.jpeg>
- [45] International Organization for Standardization: *International standard ISO/IEC 2382-37:2017 Information technology – Vocabulary – Part 37: Biometrics*, ISO/IEC JTC 1/SC 37 Biometrics, 2017, p. 27.
- [46] Sehu K. W., Weng W. R.: *Ophthalmic pathology: an illustrated guide for clinicians*. Oxford, Blackwell Publishing, 2005, s. 289, ISBN: 978-0-727917-79-9.
- [47] Wang J., Jiao L., Jing X., Chen H., Hu X., Yang Z.: *Retinal thermal damage threshold dependence on exposure duration for the transitional near-infrared laser radiation at 1319 nm*. Biomed, Opt. Express 7, 2016-2021 (2016).
- [48] Tyler M. E., Saine P. J., Bennett T. J.: *Practical Retinal Photography and Digital Imaging Techniques*. Butterworth-Heinemann, 2003
- [49] Drahanický M.: *Recognition of Eye Characteristics*. Machine Learning and Biometrics, IntechOpen, DOI: 10.5772/intechopen.76026, 2018.
- [50] Sandberg M. A., Tolentino M. J., Miller S. et al.: *Hyperopia and neovascularization in age-related macular degeneration*. Ophthalmology, 1993.

- [51] Keys R.: *Cubic convolution interpolation for digital image processing*. IEEE Transactions on Acoustics, Speech, and Signal Processing. Vol. ASSP-29, No. 6, pp. 1153-1160, 1981.
- [52] Korn G. A., Korn T. M.: *Mathematical handbook for scientists and engineers*. McGraw-Hill, 1961.
- [53] Sauer R., Szabó I.: *Mathematische Hilfsmittel des Ingenieurs*. New York: Springer Verlag, LCCN 67-25285, 1967.
- [54] Ballantine J. P., Jerbert, A. R.: *Distance from a line, or plane, to a point*. Classroom notes, American Mathematical Monthly, Vol. 59, No. 4, pp. 242-243, 1952.
- [55] Hill R. B.: *Retina Identification*. Biometrics: Personal Identification in Networked Society, Springer New York, pp. 123-141, 1996.
- [56] Optimis Fusion, System Vision accessed on 2018-06-06, image from: <http://www.systemvision.eu/uploads/4/9/5/4/49542663/1439895333.png>
- [57] Kowa VX-20. Kowa Optimed Deutschland GmbH accessed on 2018-06-06, image from: <https://www.kowamedical.com/vx20.html>
- [58] Raj V., Devi V.: *Retinal Image Analysis Using Fovea Detection using Unsymmetrical Trimmed Median Filter*. International Journal of Engineering and Innovative Technology (IJEIT), Vol. 3, ISSN 2277-3754, 2013.
- [59] Dražanský M., Smolík L.: *Entropic Numbers from the Fingerprint*. The Royal Statistical Society, pp. 1-20, 2004.
- [60] Villalobos-Castaldi M., Felipe-Riverón E. M.: *Fast automatic retinal vessel segmentation and vascular landmarks extraction method for biometric applications*, IEEE, pp. 1–10, 2009.
- [61] *Diabetic Macular Edema and Hypertensive Retinopathy*. Retina gallery, image from: [http://retinagallery.com/displayimage.php?album=228&pid=2596#top\\_display\\_media](http://retinagallery.com/displayimage.php?album=228&pid=2596#top_display_media), accessed on 2019-02-07.
- [62] Nugroho, H. A. et al.: *Automated microaneurysms (MAs) detection in digital colour fundus images using matched filter*. International Conference on Computer, Control, Informatics and its Applications (IC3INA), pp. 104-108, 2015.
- [63] Dalton M.: *Evaluating the risks of retinal detachment in cataract patients*. Eyeworld, 2012, online at: <https://www.eyeworld.org/article-evaluating-the-risks-of-retinal>.
- [64] *Lacquer Cracks*. Retina Image Bank, American Society of Retina Specialists, image from: <https://imagebank.asrs.org/file/1428/lacquer-cracks>.
- [65] Bergmüller T., Christopoulos E., Schnöll M., Uhl A.: *Recompression effects in iris segmentation*. Proceedings of the 8<sup>th</sup> IAPR/IEEE International Conference on Biometrics (ICB'15), Phuket, Thailand, pp. 1-8, 2015.
- [66] Nguyen K. et al.: *Iris recognition with off-the-shelf CNN features: A deep learning perspective*. IEEE Access, Vol. 6, pp. 18848-18855, 2018.
- [67] Trokielewicz M., Czajka A., Maciejewicz P.: *Iris Recognition After Death*. IEEE Transactions on Information Forensics and Security, pp. 1501-1514, 2019.

- [68] Fuhrmann T., Hämmerle-Uhl J., Uhl A.: *Usefulness of Retina Codes in Biometrics*. Advances in Image and Video Technology, 3<sup>rd</sup> Pacific Rim Symposium, Japan, Springer LNCS 5414, 2009, ISSN 0302-9743.
- [69] Carmona E., Rincón M., García-Feijoo J., Martínez-de-la Casa J.: *Identification of the optic nerve head with genetic algorithms*. Artificial Intelligence in Medicine, Vol. 43, pp. 243-259, 2008.
- [70] Hough P. V. C.: *Method and means for recognizing complex patterns*. U. S. Patent 3, 069 654, 1962.
- [71] Lee J., Kim S. W., Lee S. C., Kwon O. W., Kim Y. D., Byeon S. H.: *Co-occurrence of Acute Retinal Artery Occlusion and Acute Ischemic Stroke: Diffusion-Weighted Magnetic Resonance Imaging Study*. American Journal of Ophthalmology, Vol. 157, No. 6, pp. 1231-1238, 2014.
- [72] Hayreh S. S.: *Classification of central retinal vein occlusion*. Ophthalmology, Vol. 90, No. 5, pp. 458–474, 1983.
- [73] Li D.: *HSV Color Space*. Encyclopedia of Microfluidics and Nanofluidics. Springer, Boston, 2008, [https://doi.org/10.1007/978-0-387-48998-8\\_656](https://doi.org/10.1007/978-0-387-48998-8_656).
- [74] Lee C. K., Li C. H.: *Adaptive thresholding via Gaussian pyramid*. International Conference on Circuits and Systems, pp. 313-316 Vol. 1, 1991, doi: 10.1109/CICCAS.1991.184348.
- [75] Arefi H., Hahn M.: *A morphological reconstruction algorithm for separating off-terrain points from terrain points in laser scanning data*. International Archives of Photogrammetry, Remote Sensing and Spatial Information Sciences. Vol. 36, 2012.
- [76] Pizer S. M., Amburn E. P., Austin J. D. Cromartie R., Geselowitz A., Greer T., Haar Romenij, B. M., Zimmerman J. B., Zuiderveld K. J.: *Adaptive histogram equalization and its variations*. Computer Vision, Graphics, and Image Processing, Vol. 39, No. 3, pp. 355-368, 1987.
- [77] Otsu N.: *A Threshold Selection Method from Gray-Level Histograms*. IEEE Transactions on Systems, Man, and Cybernetics, Vol. 9, No. 1, pp. 62-66, 1979, doi: 10.1109/TSMC.1979.4310076.
- [78] Mehnert A., Jackway P.: *An improved seeded region growing algorithm*. Pattern Recognition Letters, Vol. 18, Issue 10, pp. 1065-1071, 1997, ISSN 0167-8655.
- [79] Zhu Y., Dass S. C., Jain A. K.: *Statistical models for assessing the individuality of fingerprints*. IEEE Transactions on Information Forensics and Security, Vol. 2, No. 3, pp. 391–401, 2007.
- [80] Gonzales R. C., Woods R. E.: *Digital Image Processing*. Tennessee, Pearson International Edition, 2008.
- [81] Serra J.: *Image Analysis and Mathematical Morphology*. 1982, ISBN 0-12-637240-3.
- [82] Gonzalez R. C., Woods R. E.: *Digital Image Processing*. 3<sup>rd</sup> Edition, Pearson India Education, ISBN 978-93-325-7032-0, 2008.
- [83] Berry T., Patterson R.: *The uniqueness of Bézier control points*. Computer Aided Geometric Design, Vol. 14, pp. 877-879, 1997, 10.1016/S0167-8396(97)00016-2.
- [84] Fawad S.: *Adapting Bresenham Algorithm*. Journal of Theoretical and Applied Information Technology, 2006.

- [85] Ebert D., Musgrave F. K., Peachey D., Perlin K., Worley S.: *Texturing and Modeling: A Procedural Approach*. Academic Press, 1994.
- [86] *Desmos Graphing Calculator*. Desmos Graphing Calculator: 2016, accessed on: 2019-01-10, available at: <https://www.desmos.com/calculator>
- [87] *CurveExpert Basic*. Hyams Development, 2016, accessed on: 2019-01-10, available at: <https://www.curveexpert.net/>
- [88] *RegressionTools: The Program*. Xuru, 2016, accessed on: 2019-01-10, available at: <http://www.xuru.org/rt/RegressionTools.asp>
- [89] Schwiegerling J.: *Field Guide to Visual and Ophthalmic Optics*. Society of Photo Optical, 2010, ISBN10: 0819456284.
- [90] Rabbetts R.: *Bennett and Rabbett's Clinical Visual Optics*. 4<sup>th</sup> Ed. Hodder & Stoughton General Div. 2007.
- [91] Risovic D., Misailovic K., Eric-Marinkovic J., Kosanovic-Jakovic N., Milenkovic, S., Petrovic L.: *Refractive errors and binocular dysfunctions in a population of university students*. European Journal of Ophthalmology, Vol. 18, pp. 1-6, 2008.
- [92] Navarro R., Santamaria J., Bescos J.: *Accommodation-Dependent Model of the Human Eye with Aspherics*, JOSA A Vol. 2, No. 8, pp. 1273–1281, 1985.
- [93] Hájek J., Dražanský M., Kolář R.: *Experimental ophthalmic multimodal imaging system for iris and retina*. Proceedings of IIAI 3<sup>rd</sup> International Conference on Advanced Applied Informatics, Kitakyushu: IEEE Computer Society, 2014, pp. 676-679, ISBN 978-1-4799-4174-2.
- [94] Abdolrahimzadeh S., Ciancimino C., Grassi F., Sordi E., Fragiotta S. et al.: *Near-Infrared Reflectance Imaging in Retinal Diseases Affecting Young Patients*. Journal of Ophthalmology, 2021, DOI: 10.1155/2021/5581851. ISSN 2090-004X.
- [95] *Prosilica GT6400*. Allied Vision Technologies GmbH, online at: <https://www.alliedvision.com/en/camera-selector/detail>
- [96] Banda H. K., Shah A., Shah G. K.: *Application of Wide-Field Infrared Reflectance Imaging in Retinoschisis, Retinal Detachments, and Schisis Detachments*. International Journal of Retina and Vitreous, Vol. 5, No. 1, pp. 42, 2019, DOI: 10.1186/s40942-019-0188-5, ISSN 2056-9920.
- [97] Timm F., Barth E.: *Accurate Eye Centre Localisation by Means of Gradients*. VISAPP, 2011, DOI: 10.5220/0003326101250130.
- [98] Groen F. C., Young I. T., Ligthart G.: *A Comparison of Different Focus Functions for Use in Autofocus Algorithms*. Cytometry, Vol. 6, No. 2, p. 81–91, 1985, DOI: 10.1002/cyto.990060202. ISSN 0196-4763.
- [99] Brouns T.: *Robust Video-Based Eye Tracking Using Recursive Estimation of Pupil Characteristics*. ArXiv, 2017.

- [100] Lyu W., Zhou Z., Chen L., Zhou Y.: *A Survey on Image and Video Stitching*. Virtual Reality & Intelligent Hardware, Vol. 1, No. 1, p. 55–83, 2019, DOI: 10.3724/SP.J.2096-5796.2018.0008, ISSN 2096-5796.
- [101] Feng X., Cai G., Gou X., Yun Z., Wang W. et al.: *Retinal Mosaicking with Vascular Bifurcations Detected on Vessel Mask by a Convolutional Network*. Journal of Healthcare Engineering, Hindawi, Vol. 2020, p. e7156408, 2020, DOI: 10.1155/2020/7156408, ISSN 2040-2295.
- [102] Berggren L.: *Iridology: A critical review*. Acta Ophthalmologica, Vol. 63, No. 1, pp. 1–8, 1985.
- [103] Bekerman I., Gottlieb P., Vaiman M.: *Variations in eyeball diameters of the healthy adults*. Ophthalmology, 2014.
- [104] Cunningham P. R., Emmett T.: *Vaughan & Asbury's General Ophthalmology*. 18<sup>th</sup> edition, New York: McGraw-Hill Medical, 2011, ISBN 978-0-07-163420-5.
- [105] Daugman J.: *How iris recognition works*. Proceedings of 2002 International Conference on Image Processing, Vol. 1, 2002.
- [106] *High-Resolution Fundus (HRF) Image Database*. Pattern Recognition Lab, 2009, Available at: <http://www5.cs.fau.de/research/data/fundus-images>.
- [107] Fischbarg J.: *The Biology of the Eye*. Elsevier Science, 2006.
- [108] Franklin K., Muir P., Scott T., Wilcocks L., Yates P.: *Introduction to Biological Physics for the Health and Life Sciences*, Wiley, 2010.
- [109] Gao X., Bharath A.: *Measurement of Vessel Diameters on Retinal Images for Cardiovascular Studies*. Medical Image Understanding and Analysis conference, 2001.
- [110] Hart W. E., Goldbaum M., Cote B., Kube P., Nelson M. R.: *Automated measurement of retinal vascular tortuosity*. International Journal of Medical Informatics, Vol. 53, pp. 239–252, 1999.
- [111] Judd D. B., Wyszecki G.: *Color in Business*. Science and Industry, Wiley Series in Pure and Applied Optics, 3<sup>rd</sup> edition, New York: Wiley-Interscience, p. 388, ISBN 0-471-45212-2, 1975.
- [112] Lahn H. E.: *Iridology: The Diagnosis from the Eye*. Kessinger Publishing, 2010.
- [113] Medeiros F. A., Zangwill L. M., Bowd C., Vessani R. M., Susanna R. Jr., Weinreb R. N.: *Evaluation of retinal nerve fiber layer, optic nerve head, and macular thickness measurements for glaucoma detection using optical coherence tomography*. Ophthalmology, Vol. 139, pp. 44–55, 2005.
- [114] Rapatzikos K., Zervakis M., Balas K.: *Detection and segmentation of drusen deposits on human retina: Potential in the diagnosis of age-related macular degeneration*. Medical Image Analysis, Vol. 7, No. 1, pp. 95-108, 2003.
- [115] Simon A., Worthen D. M., Mitas J. A.: *An evaluation of iridology*. J. Amer. Med. Assoc., Vol. 242, pp. 1385–1387, 1979.
- [116] Wang X., Cao H., Zhang J.: *Analysis of Retinal Images Associated with Hypertension and Diabetes*. Engineering in Medicine and Biology Society, 27<sup>th</sup> Annual International Conference of the IEEE Engineering in Medicine and Biology Society, Vol. 1, No. 4, pp. 6407-6410, 2005.

- [117] Košťálik G.: *Detection of diseases on the human eye retina*. Bc. thesis, supervised by: Martin Drahanský, Brno University of Technology, Faculty of Information Technology, Research group STRaDe, Czech Republic, 2020.
- [118] Košťálik D.: *Disease detection in eye retina image*. Bc. thesis, supervised by: Lukáš Maruniak, Brno University of Technology, Faculty of Information Technology, Research group STRaDe, Czech Republic, 2017.
- [119] Aubrecht T.: *Detection of diseases in the image of eye retina*. Bc. thesis, supervised by: Lukáš Semerád, Brno University of Technology, Faculty of Information Technology, Research group STRaDe, Czech Republic, 2018.
- [120] Sýkorová T.: *Detection of diseases of diabetes on the human eye retina*. Bc. thesis, supervised by: Martin Drahanský, Brno University of Technology, Faculty of Information Technology, Research group STRaDe, Czech Republic, 2019.
- [121] Palacková B.: *Comparision of retinal images with pathological finding*. Bc. thesis, supervised by: Martin Drahanský, Brno University of Technology, Faculty of Information Technology, Research group STRaDe, Czech Republic, 2019.
- [122] Dvořák, M.: *Algorithm for Realistic Vascular Circulation of Synthetic Retina*. Bc. thesis, supervised by: Lukáš Semerád, Brno University of Technology, Faculty of Information Technology, Research group STRaDe, Czech Republic, 2019.
- [123] Semerád L., Drahanský M.: Biometric entropy of retina. In *2015 International Conference on Information and Digital Technologies*, IEEE, 2015, ISBN 978-1-4673-7186-5, s. 302–304, doi:10.1109/DT.2015.7222988.
- [124] Magdolen, P. *Řízení polohovatelné platformy pro vystředění oka v obrazu*. Brno, CZ, 2018. Master's thesis. Brno University of Technology, Faculty of Information Technology.
- [125] Tretter Z. *Generování syntetických obrazů sítnice oka*. MSc. thesis, supervised by: Martin Drahanský, Brno University of Technology, Faculty of Information Technology, Czech Republic, 2017.
- [126] Pres M. Bifurcation localization in retina images. MSc. thesis, supervised by: Lukas Semerád, Brno University of Technology, Faculty of Information Technology, Czech Republic, 2016.
- [127] *Poloautomatické zařízení na snímání sítnice oka (Semi-automatic device for capturing image of the eye retina)*. Functional specimen, Faculty of Information Technology, Brno University of Technology, 2018, online at: <https://www.fit.vut.cz/research/product/587/>
- [128] Vajda I.: *Teorie informace (information theory)*. ČVUT publishing, 2004, ISBN 80-01-02986-7.